THE UNIVERSITY OF CHICAGO

DECODING EPITHELIAL FORCES: HOW CELLULAR FORCES PROPAGATE AND ARE REGULATED FROM SUBCELLULAR TO TISSUE SCALES

A DISSERTATION SUBMITTED TO

THE FACULTY OF THE DIVISION OF THE PHYSICAL SCIENCES

IN CANDIDACY FOR THE DEGREE OF

DOCTOR OF PHILOSOPHY

DEPARTMENT OF PHYSICS

BY

THERESA ANN CHMIEL

CHICAGO, ILLINOIS

MARCH 2023

Table of Contents

List of Figures:

Acknowledgements:

None of the work in this thesis was done in isolation and my success as a scientist as well as the quality of this work was made possible by numerous wonderful and inspirational people who have been a part of my life for many years. To everyone who has known me, encouraged me when work was difficult, and supported me through these long years, thank you from the depths of my heart.

My thesis advisor Margaret Gardel has been my model of a scientist and a mentor these past five years. She gave tremendous amounts of advice and guidance as I grew from a young graduate student who had so much biology to learn. At every step she advocated for me, supported me, and helped to shape this work and my view of what it means to be a biophysicist. This work would not have been possible without her, and she has my upmost respect.

I would also like to thank every member of the Gardel lab and all of the fantastic mentors and friends that I have had along the way. I need to give a set of special thanks to Bob, and Yvonne who have taught me everything I know about cell biology, the ups and down of lab work, and who have been the most supportive and helpful presences these past few years. Erik, you were the first person I knew as a new lab member and a wonderful friend. Steven, it has been such a pleasure sharing the connecting desk to yours, I always smile when I enter lab and see that you're around. Ayanna, it has been so wonderful to get to work and laugh with you. To all of the scientists that I have collaborated with through the years, your work is clearly felt in this thesis. To Kate and Shailaja, thank you for sharing you goals and your data with me, I could not have imagined working with more diligent scientists and better friends. To Yang, what an exciting experiment we built together, thank you for the time and the work that got it up and running.

I have been beyond fortunate to have a family who has supported my education and love of learning since the beginning. To my parents, who have supported me in every decision and at every step along the way, thank you for everything. Thank you for feeding my love of reading and learning as a child, thank you for helping me through my hectically busy high school years, thank you for all of the support and encouragement in college and beyond. To my siblings Becca and Matt, you guys are amazing, I love you so much and even though we've never lived near each other as adults, it's been so fun getting to see each other regularly again over zoom these past two years. Thank you also to Brisket, who has been the best cat and companion over periods of quarantine and working from home.

Thank you as well to all of my friends throughout the years. To my Kenyon friends Jenna, Morgan, Emily, and Richard thank you for the long college workdays together and the years of support and community. To my Chicago friends, Kaeli, Lucas, Louis, Liza, and Michael, you all got me through that first year of graduate school and every year since, thank you for the board games, the Pub Trivia, and the Dungeons and Dragons. You make Chicago my home. To Claire and Emily, you are both wonderful roommates and you were always able to put a smile on my face living together those first few years.

And finally, to my lovely fiancé Dan. We have walked hand in hand together throughout our PhD journey. Through the highs and lows of graduate school we have had each other, and I cannot imagine it any other way. Thank you for your patience, your humor, and your love.

Abstract:

Our understanding of the mechanics of multi-scale cellular biology continues to improve as we study the complex balance of forces found in tissues from the subcellular to the tissue scale. Determining the links between how subcellular protein activity regulates cell shape and volume and how those changes to shape and volume affect tissue architecture as a whole is vital to our understanding of cellular processes from embryo development and organization to the uncontrolled growth of cancerous masses. Here, we add to this body of work by examining how perturbations to subcellular forces, both internal and external, affect individual cell shape, motility, and overall homeostasis as well as how these forces propagate and affect tissue-scale change. Using model epithelial (and in one case endothelial) tissue, we examine various internal and external perturbations to cell force. This includes internal modifications to junctional tension from local ROCK inhibition and activation as well as modifying the presence and localization of the force sensitive LIM domain protein FHL2. It also includes the application of external forces through processes such as the addition of hyperosmotic media to create osmotic pressure changes, applying a DC electric field to induce transient calcium spikes implicated in electrotaxis, and applying shear stress through disturbances to apical fluid flow. Ultimately, we find that cell shape, volume, and cell motility is controlled through various underlying biophysical mechanisms from active membrane tension to cell-cell adhesion to local ion concentration. We also show that cell shape, volume, and motility regulation in response to force perturbations affect cells differently in small colonies compared to mature epithelial tissue, underscoring the importance of collective behavior in the regulation of tissue-scale dynamic processes.

Chapter 1: Introduction

1.1 Cellular force production

1.1.1 The cytoskeleton

Understanding mechanical forces within living organisms begins with the cytoskeleton. Cellular force generation and transmission occurs through a complex network of self-assembled filaments in the cellular cytoplasm known as the cytoskeleton. The cytoskeleton is a dynamic viscoelastic system made up of biopolymer networks (Pullarkat *et al.*, 2007). These networks act to resist cellular deformation and transmit internally generated stress through the cell at scales orders of magnitude longer than the individual proteins that make up the filaments (Fletcher and Mullins, 2010). Ultimately, they are responsible for a cell's ability to maintain shape, exert forces on their external environment, move proteins through the cytoplasm, and provide basic elements for cell motility and division (Hohmann and Dehghani, 2019).

There are three main filaments that make up the eukaryotic cytoskeleton: actin, microtubules, and intermediate filaments. These filaments are capable, along with a whole army of accessory proteins, of self-assembling, disassembling, and reassembling into complex network components (Blanchoin *et al.*, 2014). Each individual cytoskeletal protein has the ability to polymerize into a filament and transmit short range interactions into the long-range transmission of forces(Fletcher and Mullins, 2010). In this work, we largely focus on the structure and effects of the actin cytoskeleton, but that does not discount the importance of the other two components of the cytoskeleton.

1.1.2 Actin and myosin assemblies

Actin is one of the most abundant proteins in eukaryotic tissue (Dominguez and Holmes, 2011), making up approximately 20% of total protein in muscle cells and 5-10% of total protein in other cell types (Cooper, 2000). Polar actin monomers, known as globular actin or G-actin, assemble into right handed helical filaments known as f-actin (Blanchoin *et al.*, 2014). These filaments have a barbed end and a pointed end each with distinct properties. Both ends are capable of assembly, disassembly, and reassembly, but the barbed end goes through these processes 10 times faster than the pointed end and, assuming sufficient monomer concentration, can assemble to be 10μm in length in under 2 seconds (Blanchoin *et al.*, 2014). These actin filaments with the ability to polymerize and depolymerize are the basic components of the complex self-assembled networks that make up the actin cytoskeleton.

Myosin is a superfamily of molecular motor proteins which interacts cyclically with actin to create cellular contractility and generate motility (Sweeny and Houdusse, 2010). Myosin proteins each consist of heads which bind to actin subunits and tails which attach to the myosin

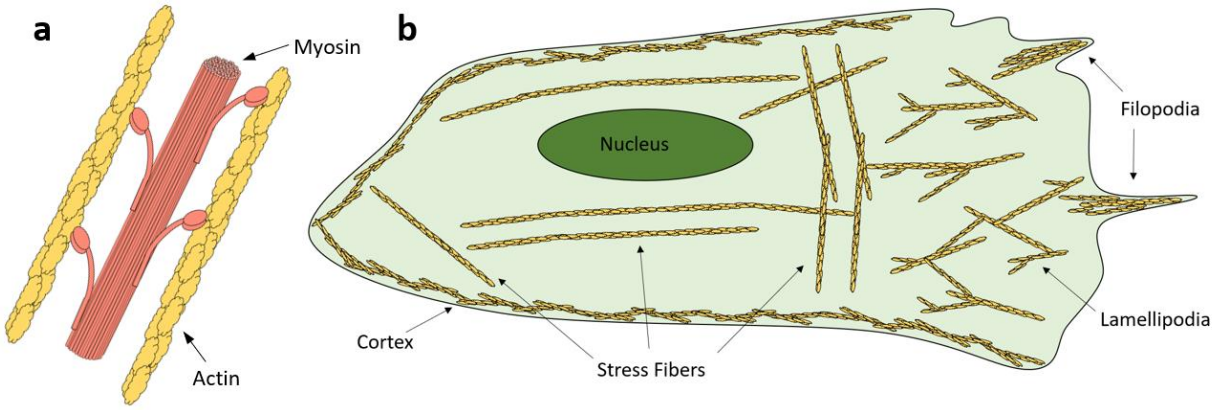

Figure 1.1: Diagrams of actin organization (a) Stacked myosin binding to actin filaments which make up a fundamental unit of contractility in the cell. (b) Actin filaments (shown in yellow) organized in a migrating cell. Including filopodia, lamellipodia, stress fibers, and the cortex surrounding the cell.

heads at a neck region and interact with loads or cargo (Craig and Woodhead, 2006). These individual molecular proteins commonly self-assemble into larger contractile bundles which undergo a power stroke cycle allowing them to pull on actin filament and generate contractile force in a cell (Hartman and Spudich, 2012). A power stroke consists of myosin moving through various mechanical conformations in which it first binds to actin, then changes conformation to create a pulling motion (the power stroke), and finally the myosin detaches and the shape of the myosin resets itself (Hartman and Spudich, 2012) (Figure 1.1a). This basic cycle allows members of the myosin family to perform tasks such as walking along actin filaments carrying cargo or sliding actin filaments across one another to generate tension in the contractile ring during cytokinesis (Warrick and Spudich, 1987).

When it comes to cell motility and force generation in cells, myosin II is a crucial component of cellular movement and reshaping. Myosin II is a double headed and non-processive member of the myosin motor family (Kovács *et al.*, 2004). In muscular cells it assembles into large bundles of hundreds of individual motors (Grewe and Schwarz, 2020), while in non-muscle myosin II forms smaller minifilaments of under 30 motors (Dasbiswas *et al.*, 2018). Non-muscle myosin II is critical for cell adhesion, migration, division, and polarity and its function is critical to our understanding of actin organization and function (Vicente-Manzanares *et al.*, 2009).

Together, along with an army of accessory assembly and regulatory proteins, actin and myosin manage to make up the actomyosin cytoskeleton. These structures include the cellular cortex, which provides tension just inside of the cellular membrane and regulates external cell shape (Salbreux *et al.*, 2012), stress fibers, filaments of actin crosslinked together to connect the cytoskeleton to focal adhesions and transmit stress to and from the external environment

(Tojkander *et al.*, 2012), the lamellipodia, a sheet of branched and crosslinked actin which pushes on the front of the cell membrane as it polymerizes resulting in cell movement (Blanchoin *et al.*, 2014), and filopodia, parallel actin bundles which protrude out of the front of migrating cells to probe the surrounding environment (Wood and Martin, 2002) (Figure 1.1b).

1.1.3 Length scales of cellular force

The actin cytoskeleton has the remarkable ability to generate and transmit forces at length scales many orders of magnitude larger than the size of individual actin or myosin monomers. As discussed in the above section, actin and myosin subunits polymerize and bind together to form crosslinked filaments which can span the length of a cell (Burlacu *et al.*, 1992; Blanchoin *et al.*, 2014). But the length scale of the forces generated by the actin cytoskeleton does not stop at the edge of the cell. Individual cells in a tissue generate forces that are transmitted collectively and affect tissue physiology on an even larger scale.

One example of this bridge between subcellular cytoskeletal dynamics and tissue scale effects is the process of convergent extension which occurs in many vertebrate and invertebrate embryo growth (Keller *et al.*, 2003). During convergent extension the embryo undergoes narrowing and a lengthening along an axis of convergence (Wolpert *et al.*, 2000). This complex process is dependent in part on the cortical actomyosin network within the cells in the tissue to polarize along the embryonic axis and coordinate cell-cell and cell-matrix adhesion as the tissue remodels (Bertet *et al.*, 2004; Skoglund *et al.*, 2008). This myosin polarization in the cortex allows for pairwise neighbor exchange of cells driving the lengthening and narrowing of the tissue.

Another example of tissue scale process controlled by the subcellular actomyosin cytoskeleton is contractility of smooth muscle tissue in vesicles. In smooth muscle tissue, integrin signals transmitted at and around focal adhesion complexes allows for the muscle cell to receive external mechanical stimuli (Gerthoffer and Gunst, 2001). In response, dynamic redistribution of the actin cytoskeleton occurs to provide the contractile forces necessary for cell scale contraction. This contraction then pulls on neighboring smooth muscle cells through the cell-cell junctions connecting the cells and further propagates the mechanical signal through the well-organized muscle tissue that makes up a vesicle, allowing for a pulse of contraction in the blood vessel as a whole (Ye *et al.*, 2014).

1.2 Epithelial tissue and cell-cell junctions

1.2.1 The epithelium

Epithelial tissue is a interface tissue which is found throughout an animal and lines body cavities, organs, and other surfaces (Marieb, 1995). It provides a diverse medley of functions including acting as a protective barrier, facilitating the absorption of nutrients, and aiding sensory reception (Tai *et al.*, 2019). There are multiple different classifications of epithelial tissue including simple epithelia, which form a single monolayer of cells attached to a basement membrane, stratified epithelia, which form from two or more cell layers such as the skin, and transitional epithelia, which start as several layers of cells that are capable of becoming just one layer when stretched as occurs in the bladder (Marieb, 1995). Another common way to classify epithelial tissue is by overall cell shape, with squamous cells growing in flat sheet-like layers, columnar cells growing tall and column-like in shape, and cuboidal cells in the middle with an almost equal height and width (Marieb, 1995; Lommel, 2003) (Figure 1.2).

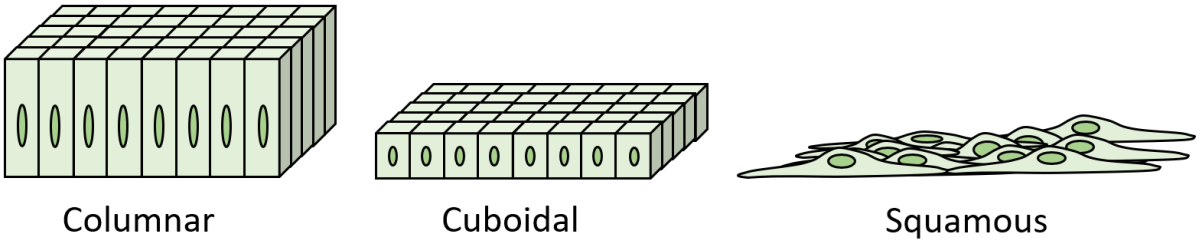

Figure 1.2: Epithelial cell shapes Epithelial cells in a simple epithelium range in shape from tall columnar cells found in the small intestine, to shorter cuboidal cells found in salivary glands and renal tubules, to very flat squamous cells found in the air sacs of lungs. This work is interested in the regulatory mechanisms which give and maintain these cellular shapes.

The function of epithelial tissue varies greatly depending on type of tissue. In the skin, the epithelium grows in many stratified squamous layers with a final layer of dead keratinized tissue on top. Here the epithelial tissue is responsible for establishing a protective barrier to prevent pathogens from entering the body, growing and healing when wounded, and protecting more internal tissue types from damage from the sun and other external objects (Bozzone and Light, 2021). In contrast, the epithelium of the small colon is an example of a simple columnar epithelial tissue. This tissue main function is to allow for maximal nutrient absorption from the gastrointestinal tract and across the tissue and into the lumen where nutrients are then absorbed into nearby blood vessels in a process known as trans-epithelial transport (Gilles-Baillien and Gilles, 2012; Palmer, 2017).

Despite its wide array of shapes and functions throughout the body, epithelial cells have certain common cellular structures. Cell-cell junctions are present in all of the various types of epithelial tissue, connecting the cells in the tissue tightly together into a densely organized barrier (Paxton *et al.*, 2003; Garcia *et al.*, 2018). In addition, apical-basal polarization complexes are found in all epithelial tissue to differentiate the apical or “top” side of the epithelial tissue from the basal or “bottom” side and allowing for sub-cellular regulation of protein localization

based on the presence or absence of these complexes(Gibson and Perrimon, 2003; Buckley and St Johnston, 2022). Epithelial cells also have a shared turnover process, with sections of the mature tissue replicating at a constant rate equal to the rate of cell death and allowing for regular tissue repair and maintenance of tension of in the cell layer (Anti *et al.*, 1998).

1.2.2 Cell-cell junctions

As mentioned in the above section, a common structure in epithelial tissue is the presence of cell-cell junctions. These junctions, including the adherens junction, tight junction, gap junction, and desmosome, mechanically tie the tissues together and propagate mechanical tension throughout the cell layer, provide semipermeable barriers, and facilitate the rapid cell-cell movement of small particles (Brückner and Janshoff, 2018) (Figure 1.3).

The adherens junction is a epithelial cell-cell junction closely associated with structurally linking cells in the epithelium and because of this plays a major role in the maintenance of mechanical tension across the tissue (Harris, 2012). This junction is known as the zonula adherens when it completely encircles cells in a mature tissue and connects to an actin belt (Meng and Takeichi, 2009). In adherens junctions, cadherin transmembrane proteins of one cell interact with calcium ions to bind with adjacent cadherin proteins of neighboring cells, binding those two cells together and to each respective actin cytoskeleton (Harris, 2012). In epithelial tissue E-cadherin (epithelial cadherin or CDH1) is the most commonly expressed member of the cadherin family (Oda and Takeichi, 2011).

Tight junctions primarily act as a physical barrier, tightly binding adjacent cells to each other just below the apical region of the cell. This junction acts as a semipermeable membrane, allowing water and some small molecules and ions through, but forcing most other molecules to

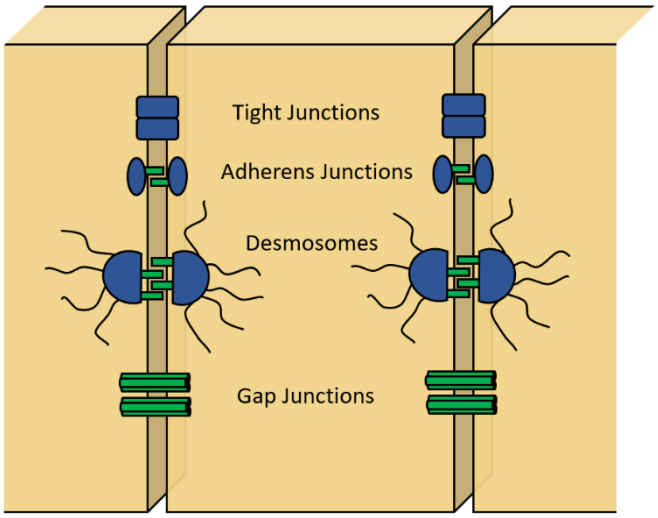

Figure 1.3: Cell-Cell Junctions Four main cell-cell junctions exist in epithelial tissue. The tight junction which is responsible for creating a semipermeable barrier between the apical and basal sides of the tissue, the adherens junction responsible for mechanically linking neighboring cells together and to the actin cytoskeleton, desmosomes which provide additional mechanical support and bind the junction to intermediate cytoskeletal filaments, and gap junctions which connect the cytoplasm of neighboring cells.

move through the cells themselves during transepithelial transport (Hirsch and Noske, 1993; Fischbarg, 2010). A complex of various proteins make up the tight junction including claudins, a transmembrane protein, occludin, an enzyme responsible for junction maintenance and remodeling, and ZO-1 (zonular occludins-1) responsible for anchoring the tight junction and connecting the complex to the actin cytoskeleton (González-Mariscal *et al.*, 2003; Odenwald *et al.*, 2018).

In contrast to the adherens junction and the tight junction which are responsible for mechanically binding epithelial tissue together, gap junctions function to facilitate communication between cells in a tissue through directly connecting the cytoplasm of neighboring cells (Kumar and Gilula, 1996). In gap junctions, connexin, a family of membrane proteins, bundles together to connect adjacent cells and form a channel allowing the cytoplasm of the cells to connect and carry signals primarily through passive diffusion (Kumar and Gilula,

1996; Söhl and Willecke, 2004). In particular, local spikes in transient intracellular calcium have been shown to propagate quickly through gap junctions and quickly transmit biochemical signals from cell to cell (Wall and Banes, 2005; Benninger *et al.*, 2008).

The final primary cell-cell junction type in epithelial tissue is a desmosome along with its basally located cousin the hemidesmosome. Like the adherens junction, desmosomes act to structurally bind cells together and resist mechanical forces, but unlike adherens junctions they do this primarily through interactions with intermediate filaments (Delva *et al.*, 2009). They are most common in skin, bladder, and cardiac tissue which are forced to withstand intense stretching and external pressure without rupturing or tearing (Holthöfer *et al.*, 2007). A desmosome is made up of three distinct regions: the extracellular core, the outer dense plaque, and the inner dense plaque. The extracellular core region is made up of the transmembrane cadherin adhesion proteins desmoglein and desmocollin and functions to connect adjacent cells (McMillan and Shimizu, 2001). The outer dense plaque connects the intracellular components of the desmoglein and desmocollin proteins and anchors them through binding to the protein plakoglobin. The inner dense plaque then binds the outer dense plaque to keratin intermediate filaments and thus to the mechanosensitive cellular cytoskeleton (McMillan and Shimizu, 2001; Delva *et al.*, 2009). Hemidesmosomes are similar in structure to desmosomes, but are found on the basal membrane of cells and anchor a tissue to the basement membrane instead of to other cells and so are not considered a type of cell-cell junction (Green and Jones, 1996). They have anchoring filaments instead of the extracellular core region found in desmosomes, but still contain an outer plaque and an inner plaque and bond to keratin intermediate filaments in the cell (Walko *et al.*, 2015).

1.2.3 Epithelial dynamics

It would be improper to discuss the nature of epithelial tissue without also touching on the dynamic balance of forces, tension, and active stresses which comprise this living material. A common inaccuracy when it comes to imagining epithelial tissue is that the tissue is static and the cells remain in one place, perhaps stretched and under tension, but not motile and under constant rearrangement. This may stem from how we observe our skin, only commonly seeing the dead keratinized tissue on top and not imagining the cells beneath which are constantly dividing, rearranging, and extruding from one layer to another. Regardless, even mature epithelial tissue not engaged in the process of embryogenesis or wound repair is a dynamic tissue with cells exchanging neighbors, growing, dividing, being apically extruded to layers above, and dying (Goodlad, 2017; Lloyd-Lewis *et al.*, 2022).

As an example, in the basal layer of the stratified epidermis cells grow and divide with proliferation of this tissue constrained to stem cells in the bottom layer of the tissue (Macara *et al.*, 2014). As this columnar basal layer becomes more and more crowded, cells are extruded upward to the surface layer where their morphology becomes flattened to squamous cells (Mackenzie and Fusenig, 1983). This dynamic motion of cells through the epithelial tissue is mediated through various mechanical forces both intracellular remodeling of the actin cytoskeleton and extracellular forces as well as through the relative strength of the adherens junction (Czirok *et al.*, 2016; Pinheiro and Bellaïche, 2018; Harmon *et al.*, 2022). The greater details of some of these processes are given below in section 1.4.

1.2.4 Immortalized epithelial monolayers

Throughout this dissertation, we make use of immortalized epithelial cells in order to capture these epithelial dynamics using a controlled medium. Immortalized epithelial cells are cells which have been modified to be able to exist *in vitro*, or outside of an organism. These cell lines have obtained the ability to grow through various mutations to their genome which allow for significantly reduced regulation of growth restriction proliferation (Irfan Maqsood *et al.*, 2013). Because these cells can be grown and manipulated outside of the constraints of a living organism, they make for ideal laboratory samples in the study of various cellular and basic tissue dynamics.

The MDCK-II (Madin Darby canine kidney) and the Caco-2 (human colorectal adenocarcinoma) cells lines are the immortalized cell lines most used in this dissertation. They both spontaneously grow to become monolayers when grown on glass or soft gel for 24-48 hours in growth media and because of these are an ideal model epithelium for the following studies in this thesis work. In particular, MDCK cells are cells taken from the collecting duct of a kidney, making up the final part of nephron that controls fluid and electrolyte reabsorption into the blood. This cell type operates in various changing osmotic conditions which affect its function of transepithelial transport (Gaush *et al.*, 1966), a detail which makes it an excellent choice of sample when studying cellular size and shape regulation in response to osmotic pressure changes as we do in chapter 3.

1.3 Cell shape regulation

1.3.1 Two-Dimensional Epithelial Cell Shape

When studying the dynamics of epithelial tissue, one common method used to simplify this complex physical system is to treat a monolayer of tissue as a two-dimensional sheet of cells. Using this model, we can simplify the relationship between cells in a tissue to polygons adhered to one another in a two-dimensional layer of packed cells. This allows us to talk about the "area" or "perimeter" of cells in a tissue as opposed to the volume and surface area that compose our three-dimensional understanding of cellular dynamics. A two-dimensional simplified model provides insight into the mechanical forces distributed throughout epithelial monolayers and affecting cell shape, motility, growth, and proliferation. It allows us to ask questions about packing and tissue density, uncover relationships between shape, motility, density, and proliferation, and ultimately explore fundamental relationships of cellular organization of epithelial tissue.

1.3.2 The Vertex Model

When studying two-dimensional epithelial sheets (and later three-dimensional sheets) one of the models which is most used to understand tissue mechanics and how the distribution of tension throughout a tissue affects cell shape and dynamics is the vertex model. The vertex model was originally developed to study the shape of packed bubbles in foam and to reduces the complex nature of cellular mechanisms to very simple forces and parameters. It imagines a two-dimensional packed epithelial tissue as various polygons with vertices at points where three or more cell junctions come together (Fletcher *et al.*, 2014; Alt *et al.*, 2017). Mechanical forces

acting on these vertices are then described and calculated to provide a model of vertex displacement as cells in the tissue evolve and change shape over time.

For a single cell in the monolayer, the mechanical energy as modeled by the most simplified version of the two-dimensional vertex model is:

$$E = K_A(A - A_0)^2 + \xi P^2 + \gamma P$$

In this equation, the first term describes the energy of the compressed cell area where K_A is the height elasticity, A is the cell area, and A_0 is the preferred cell area or the area the cell would have assuming no outside forces. The second term then represents the energy of the cell perimeter resulting from the stiffness of the actomyosin cortex where P is the perimeter of the cell, and ξ is the elastic constant of the cell cortex. The final term describes the energy from the adhesion molecules off cell-cell junctions where γ is the tension between adjacent cells (Farhadifar *et al.*, 2007; Bi *et al.*, 2015). Together, this vertex model can be used to predict cell motion and behavior.

One example of the vertex model predicting cell behavior is its ability to describe T1-transitions in which cells in a monolayer will exchange places with neighboring cells. During this transition, an edge between two neighboring cells shrinks and a new edge is created between cells which had not previously been neighbors. In order for this transition to occur in a confluent monolayer, there must be no energy barrier preventing the transition from being energetically favorable, and so in order for a T1-transition to occur, mechanical work must take place and mechanical energy from the arrangement of the cells in the tissue must be able to be converted into work (Staple *et al.*, 2010). Using the vertex model, it's possible to describe the geometries of

the epithelial sheet which allow this T1-transition and study which geometries allow the tissue to dynamically remodel and why.

1.3.3 Epithelial Glassy Dynamics

One particular example of how two-dimensional cell shape affects the tissue-scale properties of the epithelia in a way that can be captured and studied by the vertex model is through examination of glassy dynamics in the epithelium. Glassy dynamics describes a material's ability to transition from a jammed solid crystalline state to that of a more disordered and motile supercooled fluid (Lunkenheimer *et al.*, 2000). This model of epithelial tissue as a material that can undergo solid-to-liquid transitions allows us to describe the collective behavior of cells during processes such as embryonic development, wound healing, and cancer metastasis.

This rigidity transformation has been observed in confluent model epithelial tissues. Tissue with more circular "regular" shaped cells behave in a more solid-like manner, meaning T1-transitions are rare, individual cells in the tissue have limited motility, and the material as a whole can be described as in a jammed state. In contrast, tissue with more jagged "irregular" shaped cells are shown to behave as a more liquid material with energetic states that favor t1-transitions, and individual cells being highly motile as can be seen in developing embryos and during tissue wound healing (Bi *et al.*, 2015, 2016; Park *et al.*, 2015; Lawson-Keister and Manning, 2021).

The parameter most closely associated with understanding this glassy transition is known as the shape index (ρ), which is a dimensionless measurement of cell irregularity using the area and perimeter of the cell's polygon described by the vertex model. The shape index is defined as:

$$\rho = \frac{P}{\sqrt{A}}$$

And so, the smallest shape index possible is that of a circle at 3.54 (Park *et al.*, 2015) and a regular pentagon has a shape parameter of 3.72 and we observe shape parameters of typical epithelial cells from 3.6 to 5.0 with no theoretical upper limit for how large the shape parameter could get (Bi *et al.*, 2015; Park *et al.*, 2015).

What has been observed, is that there is an energy barrier for local cellular rearrangements that can be described using the vertex model and that governs this solid-to-liquid behavior. This energy barrier is described by the shape index and allows to tissue to transition from solid-like properties to liquid-like properties as ρ becomes greater than 3.81 (Bi *et al.*, 2015; Park *et al.*, 2015). In this way, we can mechanically describe how individual cell shape regulation affects overall tissue-scale dynamics in a two-dimensional model system.

1.3.4 Three-Dimensional Epithelial Cell Shape

Despite the profound relationships uncovered using a simplified two-dimensional understanding of epithelial tissue dynamics, in living organs it is rare to find cells growing solely in two dimensions and there are a number of processes which require a three-dimensional model of tissue growth and shape in order to fully analyze. Understanding how the properties of tissue height and cell volume affect changes in three dimensions is often required for more complex epithelial properties.

As an example, the process of epithelial invagination during morphogenesis is a process which converts sheets of epithelial tissue into three-dimensional tube-like structures form the early stages of organ development (Pearl *et al.*, 2017). During this process, cytoskeletal and cell-

cell adhesion changes allow for changes to cell shape. First the cells lengthen as height increases, and then the apical surface of the cells along where the invagination pit or furrow will form apically constricts. This is followed by cell shortening and expansion of the basal surface. Together this coordination of cell shape allows a pit or a furrow to form in formerly flat epithelial sheet, folding the tissue into three dimensions (Lee and Harland, 2010; Kondo and Hayashi, 2015). This maneuver cannot be described using models which only consider cells as polygons on a two-dimensional sheet, it requires a much fuller understanding of the three-dimensional nature of cells in the tissue.

Over the years, there have been many versions of the vertex model applied to three-dimensional cell shape. These models either treat cells as two dimensional objects applied to a three-dimensional curved surface such as an ellipsoid (Trichas *et al.*, 2012) or as three-dimensional scutoids with each cell able to have a height and volume of its own (Gómez-Gálvez *et al.*, 2021). These models have been used to improve our understanding of tissue mechanics in processes from drosophila salivary gland formation (Durney and Feng, 2021) to tubular mechanics during mouse epididymal development (Hirashima and Adachi, 2019) to early growth if cancerous masses in the pancreas (Messal *et al.*, 2019) all using the same fundamental principles of the vertex model.

1.4 Epithelial Force Sensing and Force Production

1.4.1 The Role of Force Sensing in Tissue

It is critical for cells in a tissue to be able to create and respond to mechanical cues and external forces. Sensing external forces from other cells in a tissue or from sources external to the tissue is a vital component of tissue homeostasis, development, growth, and motility. This

process is known as mechanical signal transduction or “mechanotransduction” and is the mechanism of converting physical forces into biochemical signals which influence cellular behavior and often overall tissue dynamics (Sun and Alushin, 2022).

The actomyosin network is capable of modifying its shape and structure to generate different forces which can be transmitted between cells or transmitted to the extracellular matrix (Chanet and Martin, 2014). Because of this, the actin cytoskeleton is an integral part of the feedback necessary for mechanotransductive pathways and a wide variety of cytoskeletal accessory proteins have been shown to mediate these processes (Luo *et al.*, 2013). This response to mechanical force may look like actin bundles organized into thin finger-like protrusions known as filopodia which extend into the extracellular matrix and exert traction forces on its surroundings (Mattila and Lappalainen, 2008). Alternatively, this response may look like contractility in the cellular cortex generating a pulling force or focal adhesions coupled to the extracellular matrix, further transmitting a force to other cells in the tissue or to the basal substrate (Chanet and Martin, 2014). Here, we will go into further detail on how epithelial cells sense forces in a tissue, how they transmit the sensing into biochemical signals, and how this allows forces to propagate through a tissue. Specifically, we will focus on the details of the well-studied Rho/ROCK pathway, the role of LIM domain proteins, and how calcium and other ion cues facilitate these processes.

1.4.2 LIM Domain Proteins

One key driver of mechanosensitivity is the superfamily of LIM domain proteins, named for the three homeodomain proteins where it was discovered Lin1 1, Isl-1, and Mec-3, which contain one or more regions of double zinc finger motifs in the protein structure (Bach, 2000).

This superfamily of proteins are a critical component of mechanical signaling pathways and have been implicated in numerous strain-sensing regulatory roles including stress fiber remodeling and repair (Smith *et al.*, 2010), cell adhesion mechanisms (Brown *et al.*, 1998; Razzell *et al.*, 2018; Anderson *et al.*, 2021) , and substrate stiffness detection (Wang *et al.*, 2021; Swiatlowska *et al.*, 2022). These proteins are strongly implicated in rearranging the actin cytoskeleton in response to external forces on the cell (Smith *et al.*, 2010).

Zyxin, a LIM domain protein strongly associated with the repair of actin stress fibers and basal focal adhesions (Guo and Wang, 2007), is one example of how LIM domain proteins mediate mechanosensing in epithelial tissue. Zyxin has been shown to accumulate at sites of damaged stress fibers and facilitate the repair and thickening of these actin filaments (Smith *et al.*, 2010; Oakes *et al.*, 2017). This localization has been shown to be force sensitive, meaning that zyxin is able to sense force-bearing actin stress fibers, and preferentially bind to these filaments (Colombelli *et al.*, 2009; Smith *et al.*, 2010), and this force sensing ability is linked to the zinc finger motif present in the LIM domain (Uemura *et al.*, 2011).

1.4.3 The RhoA/ROCK Pathway

A family of crucial regulators of the actin cytoskeleton is the Rho family of GTPases which regulate a range of cellular functions from cell cycle processes, to overall cortical contractility, to cell-cell adhesive complexes (Villalonga *et al.*, 2006; Terry *et al.*, 2010). GTPases are GTP-binding proteins which act as a molecular switch as they cycle between being active and GTP bound and inactive and GDP bound. Activated Rho GTPases are able to interact with different cellular target proteins, often associated with the actin cytoskeleton (Mackay and Hall, 1998; Etienne-Manneville and Hall, 2002). One such target protein is Rho-associated

protein kinase (ROCK) which triggers local myosin contractility (Amano *et al.*, 1996). ROCK is activated by the Rho GTPase known as RhoA, and together these two proteins make up the RhoA/ROCK pathway.

This RhoA/ROCK pathway regulates myosin II activity and is responsible for a wide array of contractile forces present within cells. Active RhoA interacts with ROCK as an effector molecule which then promotes the phosphorylation of myosin light chain (MLC) in myosin II which in turn promotes myosin II mediated contractility in the cytoskeleton (Totsukawa *et al.*, 2000; Lessey *et al.*, 2012), ultimately turning biochemical signals into mechanical forces within the cell. ROCK also stabilizes actin filaments through the activation of the protein LIM kinase which works to inhibit of cofilin, an actin severing protein (Maekawa *et al.*, 1999).

In particular, RhoA has an active role mediating tension at cell-cell junctions in epithelial tissue. RhoA has been shown to be necessary for junctional assembly as myosin mediated tension is an important component of the dynamic remodeling of epithelial junctions (Yamada and Nelson, 2007; Liu *et al.*, 2010; Itoh *et al.*, 2012). Mutations to RhoA or inhibition of RhoA activity through the enzyme C3 transferase results in the thinning of the actin belt which surrounds epithelial tissue just below the adherens junction as well as reduces functionality of the tight junctions and the adherens junctions resulting in a more porous and less structurally sound tissue (Nusrat *et al.*, 1995; Bruewer *et al.*, 2004; Desai *et al.*, 2004). Proper cell-cell adhesive functions have been shown to be dependent on zones of junctional RhoA where RhoA as well as GTP loading and GTPase activating proteins cluster and dynamically mediate myosin II activity through the RhoA/ROCK pathway (Priya *et al.*, 2017), and so modulating and controlling not just whether RhoA is activated and present in a cell, but whether it is localized to these zones

adjacent to the adherens junction is a second level to the complex signaling network which mediates cellular force sensing and force response.

1.4.4 Mechanical Calcium Cues

Calcium is an essential ion in organisms and its signaling is involved in various physiological mechanism from muscle stimulation to neural pathways to the regulation of junction adhesion (Armstrong and Hille, 1998; Elmas, 2016; Varadarajan *et al.*, 2021). Calcium ions can flood into a cell's cytoplasm through voltage dependent ion channels, gap junctions connecting a cell's cytoplasm to its neighbors, or calcium permeable channels in the smooth endoplasmic reticulum (Hoenderop *et al.*, 2005; Greer and Greenberg, 2008). This complex array of transport methods work together to signal a variety of mechanical cues in the epithelium.

Within the cell-cell junction, calcium ions play a critical role in adhesion dynamics. The adherens junction is dependent on cadherin-cadherin dynamics, meaning that transmembrane cadherin proteins from one cell in a tissue needs to bind to the cadherin proteins embedded in the membrane of the adjacent cell in order to mechanically tie the cells together and form the adherens junction (Oda and Takeichi, 2011; Buckley *et al.*, 2014). This interaction requires the presence of extracellular calcium ions in order to make the ends of the cadherin molecules rigid enough to bind to one another (Nagar *et al.*, 1996).

Calcium ions have also been implicated in regulating integrin mediated adhesion. Integrins are a family of receptor proteins which link extracellular matrix molecules to the actin cytoskeleton at basal focal adhesions (Humphries, 2000). Calcium ions have been shown to inactivate integrin binding by reducing their affinity to extracellular ligands (Huttenlocher *et al.*,

1996), reducing cell-matrix adhesive properties. This allows the regulation of calcium ions, calcium related ion channels, and other methods of local calcium modulation to play a vital role in cell migration. In order to migrate, cells need to coordinate highly regulated and localized adhesive interactions through first promoting and then dispelling cell-matrix adhesions (Huttenlocher *et al.,* 1996). Local regions of calcium "flickers" have been found at the leading edge of migratory cells to assist in cell migration and have even been implicated in steering the migratory cell (Wei *et al.*, 2009, 2012), underpinning the ion's important role in establishing mechanical cues in dynamic cellular conditions.

Chapter 2: Measurements of Cellular Volume Variation in Epithelial Monolayers

2.1 Abstract

Epithelial tissue stability is highly dependent on cell shape and size regulation. While two-dimensional cell shape has been well characterized and heavily studied, three-dimensional cell shape regulation is less well understood despite its critical role in large scale epithelial processes such as invagination. By examining the relationship between cell height, volume, density, and biological components of the actin cytoskeleton, we explore the mechanisms by which epithelial cells regulate shape and volume. We see that there is high cell volume variability within epithelial tissue that is not dependent on mean monolayer density or cellular cytoskeletal activity. However, we do find that localized cell density in a tissue affects local volume variability of cells in the region.

2.2 Introduction

The shape and size of individual cells in a tissue has tremendous consequences for the function and physiology of that tissue. For example, we see that in a monolayer where cells change neighbors and migrate through the tissue, cell speed is highly correlated with cell shape. Rounder cells form a more solid tissue with less migration and neighbor changes, while more elongated cells form a more fluid-like tissue with increased cell migration through the tissue (Park *et al.*, 2015; Devany *et al.*, 2021). Additionally, during development, changing cell shape mediates the process known as invagination, which is a morphological process where there is a local infolding of an epithelial tissue to form a cavity (Ettensohn, 1985). In the beginning stages

of invagination, cells first increase in height, and then constrict their apical domain to form the beginning of a shallow pit, followed by cell shortening and extension of the apical domain which acts to more fully form a new invaginated furrow (Kondo and Hayashi, 2015). It's the changes in cell shape that drives these critical mechanical processes.

There has been significant research into how cell shape affects the balance of forces in an epithelial sheet. The most common modeling approach used to investigate these processes is know as the vertex model. This model is a framework used to combine tissue geometry with cell forces to describe the underlying physics of tissue dynamics. In it, cells are approximated in two dimensions as polygons where the polygon edges are cell-cell junction, and the vertices are tri-cellular junctions. Each vertex is capable of moving in response to forces including growth, membrane tension, and pressure withing the cell (Fletcher *et al.*, 2014). These models have been used to study a variety of important cellular processes, from collective cell motility (Koride *et al.*, 2018), to ventral furrow formation in Drosophila (Spahn and Reuter, 2013).

In addition to the two-dimensional vertex model, there has been a lot of research into adapting this model for three dimensions. These three-dimensional models reformat the equations necessary for the two-dimensional model, changing length into area and area into cell volume with vertices lying on a three-dimensional manifold as opposed to a flat sheet (Du *et al.*, 2014; Alt *et al.*, 2017). Three-dimensional models of tissues are ideal for studying the complex morphological changes that occur during development. Many, but not all of these three-dimensional models assume a constant or "preferred" cell volume, with cells maintaining their volume despite changes to cortical tension, cell height, and overall tissue geometry (Alt *et al.*, 2017; Gómez-Gálvez *et al.*, 2021).

Here, we answer some of these open questions on volume regulation in three dimensions. We show that volume in epithelial tissue is highly variable and independent of the mean monolayer density as well as many disruptions to cellular cytoskeletal activity. We find that, in fact, cellular volume in these mature tissues is regulated at a very local scale as the size and tissue density of immediate cell neighbors is the largest predictor of local volume and volume variability.

2.3 Results

2.3.1 Cell volume in monolayers is highly variable and globally independent of monolayer density

To explore changes in cell volume occurring in mature epithelium, we develop protocols to characterize the changes in cell volume. MDCK-II cells are plated densely on glass slides and grown for 48 hours with 100% confluency achieved after 24 hours. CellMask Orange membrane dye is added prior to imaging to clearly outline the apical and basal membranes in monolayers (Figure 2.1a). This allows us to calculate average monolayer height for a desired field of view (135x175 μm^2) in a sample through plotting the average intensity for each slice of our 3-dimensional image and fitting the two peaks in intensity, which represent the apical and basal membranes of the sample, to a gaussian (Figure 2.1b). The difference between these two peaks is the local average height of the monolayer. We then measure the average cross-sectional area and approximate average cell volume in a monolayer as the average cross-sectional area multiplied by the average monolayer height (Figure 2.1c).

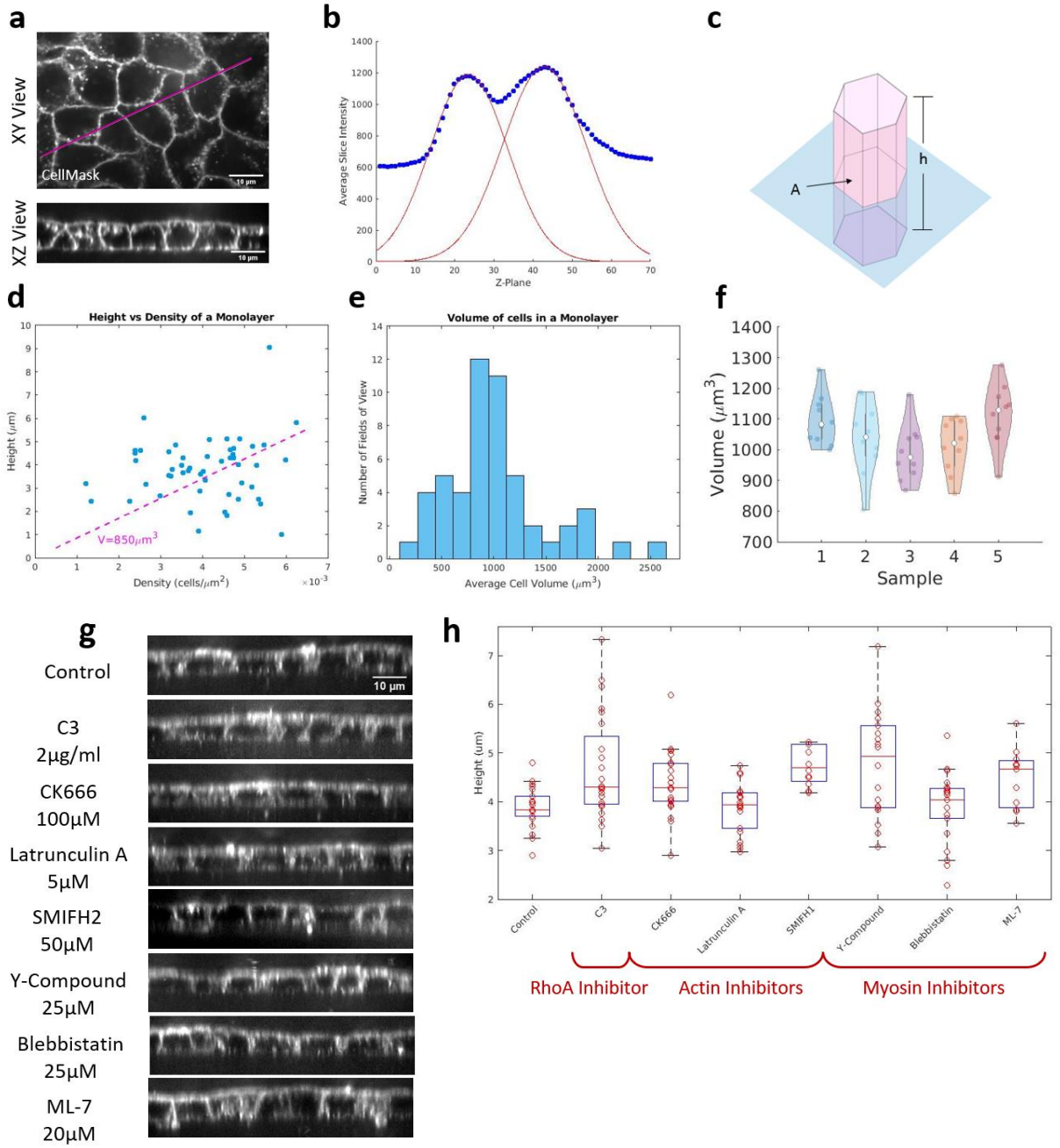

Figure 2.1: Cell volume in monolayers is highly variable and globally independent of monolayer density or cytoskeletal inhibition (a) Images of live MDCK monolayers. Cell membrane stained with CellMask Orange. Scalebars are 10μm. (b) Intensity of CellMask Orange membrane stain at different slices of the three-dimensional image, used to measure average monolayer cell height. (c) Average monolayer volume is approximated as average height, h, multiplied by average cross-sectional area, A. (d) Measured average density and height of 52 separate regions of MDCK monolayers. Each region is 135x175μm^2 field of view. Pink line is a line of constant volume at the mean volume of all cells measured (850μm^3). (e) Histogram of the average cell volume across the 52 fields of view. (f) Violin

Figure 2.1 Continued: plot representing the variation in volume across monolayers. Each sample represents a difference monolayer with each data point representing a different 135x175μm^2 field of view in that monolayer. (g) Images of live MDCK monolayers. Cell membrane stained with CellMask Orange. Various cytoskeletal inhibitors added to monolayer 2 hours prior to imaging. (h) Boxplot of cell heights with each data point representing a different 135x175μm^2 field of view in that monolayer.

This experiment was replicated by using five separate samples, each of which exhibited natural variation in both cell density and cell volume (Figure 2.1d). The scale of this variation can be seen within a single 135x175 μm^2 fields of view, indicating that on this scale, the natural variation in local volume is consistent with the average variation in volume between one monolayer and another, this both justifies treating each field of view in a sample as effectively independent and allows us to make conclusions about the global (as opposed to local) relationships between monolayer height, density, and cell volume.

We find that the mean height and volume of cells using this method between different 135x175 μm^2 fields of view fluctuated widely with mean cell heights varying from 0.8-9.0 μm and densities varying from 0.001-0.007 cells/ μm^3 (Figure 2.1e). In addition, we saw no significant correlation between height and density in the different samples. Figure 2.1e shows a line representing the mean volume of all cells measured. Assuming that height and density were highly correlated to achieve some "preferred" cell volume, we would expect the data to correlate with this line. This is clearly not the case. Instead, we see that there is no "preferred" volume with the average cell volumes of different fields of view fluctuating between 200-2600 μm^3 and varying by over 15x (Figure 2.1f).

2.3.2 Cytoskeletal inhibitors have limited effect on cell volume or monolayer height

Our first instinct was to examine the role of the cytoskeleton in the regulation of three-dimensional shape in epithelial monolayers. After all, cytoskeletal components play a major role

in two-dimensional shape regulation with myosin II activity mediated through the Rho/ROCK pathway or through Myosin Light Chain Kinase (MLCK) are found to be a critical mediator of cell shape (Niggli *et al.*, 2006; Mader *et al.*, 2007; Blanchoin *et al.*, 2014).

To explore this, we tested a variety of actin, myosin and RhoA inhibitors including C3 Transferase (a Rho inhibitor), CK666 (an Arp-2/3 complex inhibitor), Latrunculin A (an actin polymerization inhibitor), SMIFH2 (a formin inhibitor), Y-27632 (a ROCK inhibitor), Blebbistatin (a myosin-II inhibitor), and ML-7 (an MLCK inhibitor) (Figure 2.1g). We see that while each of these inhibitors do see variation in three-dimensional cell height, all this variation is well within the expected variation between samples that we see without any perturbations to the cytoskeleton (Figure 2.1h).

2.3.3 Local monolayer density affects cell volume variability in a tissue

Once we determined that mean monolayer density and cell height does not show significant correlation and results in highly variable cell volume, we next asked at what scale do these values fluctuate locally? We volumetrically imaged larger sections of a monolayer by stitching together individual fields of view (Figure 2.2a,d). Individual cell height was found using a similar method to that described in section 2.3.1, but for each cell as opposed to averaging over the entire field of view. Local density for each cell was determined by first finding the area of each cell and its immediate neighbors and dividing the number of cells in that region by the area (Figure 2.2a-f). We examined the local distribution of cell height and density for both a sparce and dense monolayer which we expect would be experiencing growth inhibition (Figure 2.2a-c), and a less mature monolayer with lower density which has recently grown to confluency (Figure 2.2d-f).

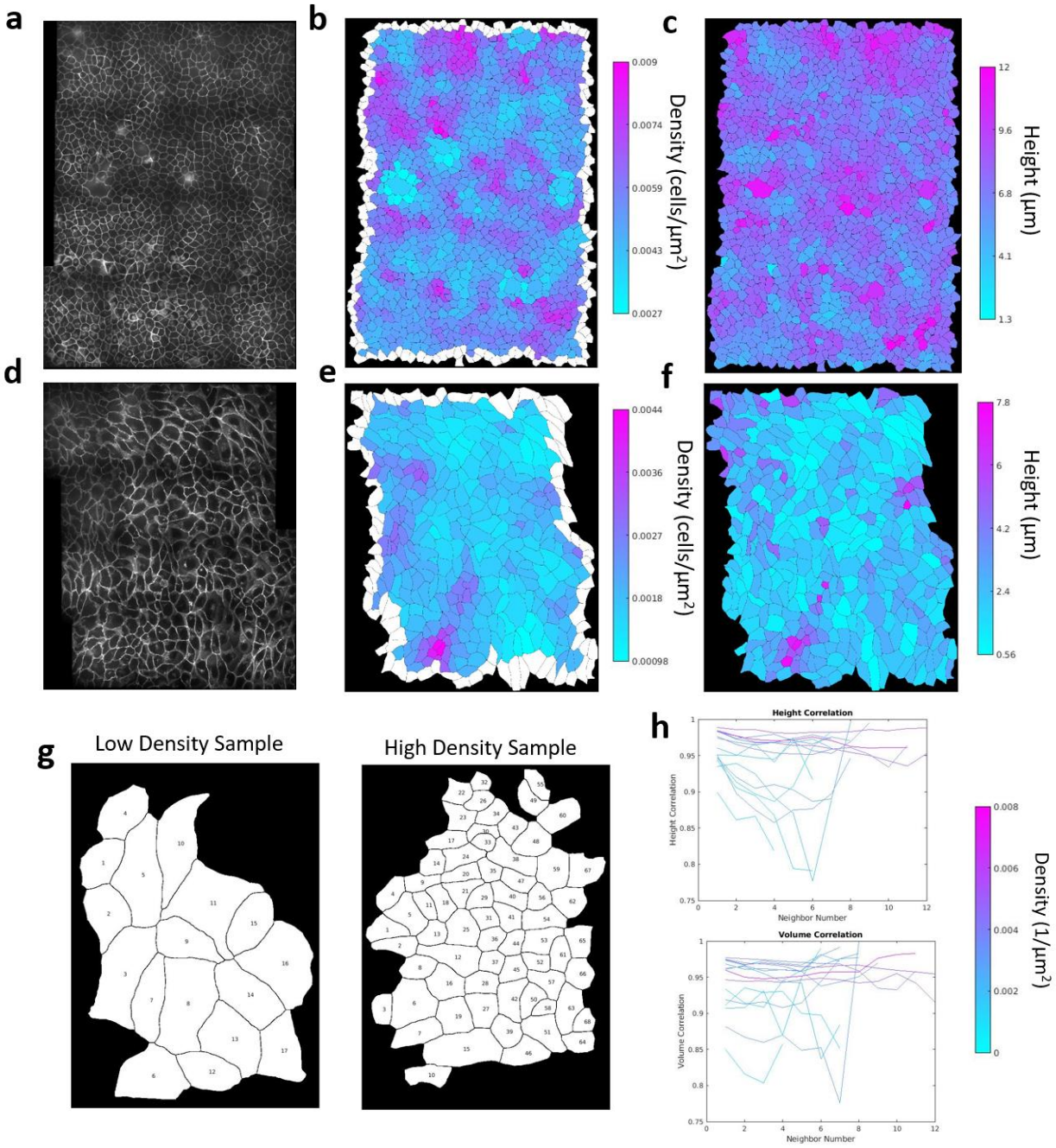

Figure 2.2: Local monolayer density affects cell volume variability in a tissue (a) A dense monolayer of MDCK cells. Cell membrane stained with CellMask Orange. 16 fields of view have been stitched together to create this one image while imaging at a high enough magnification to capture relevant volumetric information. (b) Dense monolayer cells segmented using Cellpose machine learning software. Map of local density in the tissue. Local density is measured by finding the density of each cell and its immediate neighbors. (c) Map of individual cell height in the dense tissue. (d) A sparse monolayer of MDCK cells. Cell membrane stained with CellMask Orange. 16 fields of view have been stitched together to create this one image while imaging at a high enough magnification to capture relevant

Figure 2.2 Continued: volumetric information. (e) Map of local density in the sparse tissue. (f) Map of individual cell height in the sparse tissue. (g) Cellpose machine learning segmentation of example low- and high-density sample tissues used for the volume and height correlation measurements. (h) Pairwise height (top) and volume (bottom) correlation of samples for regions of a MDCK monolayer at different densities. Neighbor number refers to the number of cells in between any pair of cells in the tissue. See Methods for additional details.

We see that for both of these monolayers, there are significant density fluctuations in the monolater and areas of both higher and lower density scattered throughout the sample (Figure 2.2b,e). We also find that there are regions of both higher and lower cell height throughout the monolayer (Figure 2.2c,f). However, the sample density affects the correlation that we observe between cell density and cell height. For the high-density sample, while there are regions of the sample in which cell density and cell height are highly correlated, there are also regions in which they are clearly anticorrelated (Figure 2.2b,c). This is not the case for the low-density sample. The cell height and cell volume are very well correlated in the low-density sample with cells in a denser region of the sample consistently taller than cells in more sparse regions (Figure 2.2c,f). This indicates that at the scale of cells and their immediate neighbors, there is a correlation between regions of high density and increased individual cell height only in mature, growth inhibited samples.

In order to better quantify this local correlation, we looked at individual fields of view at varying densities and segmented these images using Cellpose machine learning software (Figure 2.2g). We wanted to see how correlated height and volume of two cells in the monolayer were likely to be based on how many neighbors removed they were from each other in the tissue. To do this we found the pairwise correlation between each pair of cells in the monolayer (see

methods section 2.5 for details). We find that regions of high density are more likely to have high neighbor correlation in both height and volume than cells in regions of lower density (Figure 2.2h), meaning that local variations in height and volume are reduced in regions of high density.

2.4 Discussion

Through this careful study of epithelial cell volume distribution, variation, and overall three-dimensional cell shape, we have a greater understanding of what does and does not regulate cell size and shape. Here, we are able to conclude that the overall mean height and volume of cells in a tissue is independent of tissue density and highly variable sample to sample. We also show that this size regulation is not mediated through direct cytoskeletal regulation as has been shown in two-dimensional cell shape regulation (Niggli *et al.*, 2006; Mader *et al.*, 2007; Blanchoin *et al.*, 2014). Interestingly, it is the very local cell-cell neighbors that are the greatest predictor of cell size and volume with high density confined sample tissues showing higher correlation of cell height and density as well as greater height and volume correlation across greater distances in the samples.

These findings shed light on related work in the field of cell size regulation. Similarly, Zehnder et al. tracks the volume of MDCK cells over multiple hours and shows that epithelial tissue undergoes volume fluctuations of approximately 20% over the course of two hours, which is comparable to the variation that we see within each tissue sample (Figure 2.1f). They find that this variation is driven at a very local level with cell groups of 5-10 neighbors fluctuating together (Zehnder *et al.*, 2015). Our conclusions here directly corroborate and add to these findings. We see that this local volume correlation is specifically dependent on the tissue reaching a threshold of density at around 0.005 cells/μm^2. Above this threshold, cell volume is

highly correlated in the closest 5-10 neighboring cells, but below this threshold there is significantly reduced volume correlation.

Our understanding of volume correlation and its relationship to tissue density is also highly related to the effects of growth inhibition in a tissue. MDCK cells experience contact-based inhibition of cell growth (Saier, 1981) with cells in a confluent tissue experiencing limited growth while continuing to divide until a set density is reached in which both growth and division are inhibited (Di Meglio *et al.*, 2021; Devany *et al.*, 2022). We can see this contact inhibition taking place in our denser samples which have overall smaller cells and in which cell height is highly influenced by cell density with denser areas resulting in taller cells (Figure 2.2 a-c). We see that this correlation is not present in our confluent but still low-density tissue, where local density is not a predictor of individual cell height (Figure 2.2 d-f). Allowing us to map the onset of contact inhibition as the denser tissue and tighter confinement results in lower variations in local volume variability (Figure 2.2h). All together, these data tell a story of tissue confinement coupled with growth inhibition in a mature tissue which results in reduced local volume variability and increased tissue size correlation.

Overall, this work describes local volume distribution and variation across samples in unperturbed conditions. In the following chapter we will build on these conclusions to examine how cell volume in a tissue is regulated when subjected to an external force, namely an external osmotic force.

2.5 Methods

Cell culture: MDCK-II cells were cultured in Dulbecco's Modified Eagle's Medium (DMEM) and supplemented with 10% fetal bovine serum (FBS) (ThermoFisher Scientific), 2mM L-glutamine (Invitrogen), and penicillin-streptomycin (Invitrogen). Cells were incubated in a humidified environment at 37C and 5% $C0_2$.

Sample creation: To create a mature monolayer, MDCK cells were plated densely to coat the glass bottom of an 8-well chamber (Ibidi). The cells were then incubated for 48 hours with a change of media at 24 hours. Inhibitors were added 3 hours prior to imaging.

Microscopy and live cell imaging: 2µl/ml of CellMask Orange (Invitrogen) was added to samples 30 minutes prior to imaging to stain the cell membrane. Samples were imaged on an inverted T-E microscope (Nikon) with a confocal CSU-X spinning disk (Yokogawa Electric Corporation), a stage controller (Prior), and a CMOS camera (Zyla-Andor). Metamorph software was used to control the microscope and collect images. A stage incubator (Chamlide and Quorum Technologies) with CO-2, humidity, and temperature control was used for timelapse experiments while a stage heater (Nevtek, ASI 400) was used for non-timelapse experiments. A 561 nm laser (MPB Communications, VFL-P Series) was used to illuminate the CellMask Orange stain. Images were acquired using a 60x Plan Apo NA water immersion objective with a NA of 1.20 and a WD of 0.31-0.28 (Nikon). Three-dimensional images were collected using z-stacks of 0.25µm steps.

Height and volume analysis: Both ImageJ and Matlab were used for image analysis of monolayer height and volume. Average monolayer height was measured using Matlab by taking the average image intensity for each z-stack of the 3-dimensional image. The peaks in average image intensity at the apical and basal membrane from the CellMask Orange dye were fitted to a

gaussian and the distance between these peaks was measured to find the monolayer height. In ImageJ, the Cell Counter tool was used to determine the density of cells in each sample image. This density measurement was used to determine the average cross-sectional area of the cells in the image. The average volume of cells in the monolayer was found by multiplying the average cross-sectional area by the average monolayer height.

Image Stitching and Segmentation: Multiple images were stitched together to form Figures 2.2 a and d. To do this, the imageJ Grid/Collection Stitching plugin was used (Preibisch *et al.*, 2009). Once the images were stitched together, Cellpose segmentation software was used to segment the images to form the image outlines seen in Figures 2.2 b, c, d, and e (Stringer *et al.*, 2021).

Pairwise Correlation and Neighbor Numbers: Pairwise correlation between the heights of different cells was performed using the formula:

$$C_H = 1 - \left(\frac{H_2 - H_1}{H_2 + H_1}\right)^2$$

Where C_H is the pairwise height correlation between cells 1 and 2, $H_1$is the height of cell 1and H_2 is the height of cell 2. Similarly, the pairwise correlation between the volumes of different cells was performed using the formula:

$$C_V = 1 - \left(\frac{V_2 - V_1}{V_2 + V_1}\right)^2$$

Where $C_V$is the pairwise volume between cells 1 and 2 and V_1 and V_2 are the respective cell volumes. To find the total height and volume correlations, C_H and C_V were found for each combination of pairs of cells in each image and averaged over their neighbor number, how many

cells apart they were in the monolayer with adjacent cells having a neighbor number of 1, cells separated by one other cell having a neighbor number of 2 and so on.

Quantification and Statistical analysis: Image analysis and quantification was performed in Fiji, Excel, and Matlab.

Chapter 3: Confluence and tight junction dependence of volume regulation in epithelial tissue

3.1 Abstract

Epithelial cell volume regulation is a key component to tissue stability and dynamics. In particular, how cells respond to osmotic stresses is of significant physiological interest in kidney epithelial tissue. For individual mammalian cells, it is well established that Na-K-2Cl cotransporter (NKCC) channels mediate cell volume homeostasis in response to hyperosmotic stress. However, whether mature epithelium respond similarly is not well known. Here we show that while small colonies of MDCK epithelial cells behave similarly to single cells and exhibit volume homeostasis that is dependent on the NKCC channel function, mature epithelial tissue does not. Instead, the cell volume decreases by 33% when confluent monolayers or acini formed from Madin Darby Canine Kidney (MDCK) cells are subjected to hyperosmotic stress. We show that the tight junction protein, Zonula Occludins-1 (ZO-1), and Rho-associated kinase (ROCK) are essential for osmotic regulation of cell volume in mature epithelium. Since these both are known to be essential for tight junction assembly, this strongly suggest a role for tight junctions in changing volume response in mature epithelium. Thus, tight junctions act either directly or indirectly in osmotic pressure response of epithelial tissue to suppress volume homeostasis common to isolated epithelial cells.

3.2 Introduction

Epithelial cells actively regulate their volume in response to osmotic gradients through management of ion concentration and cytoskeletal tension (Delpire and Gagnon, 2018). Animal cells lack rigid structures that would help to maintain an osmotic gradient across the plasma membrane, meaning that when an osmotic pressure is applied to the membrane, a cell must respond with a sizable deformation to the membrane or risk rupture (Strange, 1993; Hoffmann *et al.*, 2009). It does so primarily by controlling the movement of solutes across the cell membrane through tightly regulated ion channels (Finan and Guilak, 2010). And so, while osmotic stress is a mechanical force on a tissue, how the cells in that tissue respond physically and the regulatory pathways involved in this response is a significantly more complicated relationship.

The pump-leakage model is the basic model that is used to understand regulation of cell volume through ion transport and in response to changes in external or internal osmotic pressure (Strange, 1993). When hypertonic media is introduced, highly membrane permeable water initially rushes out of the cell, causing the cell to shrink in volume. The cell then reacts by activating a variety of transport channels, and predominately the Na-K-2Cl cotransporter (NKCC) family (Haas, 1994), to increase ion concentration in the cytoplasm and restore the osmotic gradient (Haas, 1994; Delpire and Gagnon, 2018). This process to re-establish cell volume after a hyperosmotic shock is known as a regulatory volume increase (RVI).

The response to osmotic gradients in epithelial tissue is not as well understood as in single cells and, presumably, involves both cell and tissue-scale responses. In polarized epithelial tissue, tight junctions assemble at the apical surface and create a barrier to prevent the extracellular flow of osmolytes across the epithelial tissue (Günzel and Yu, 2013; Varadarajan *et al.*, 2021). Tight junctions prevent “leakiness” in epithelial tissue and are designed to act as a

barrier between the internal and external cellular environments (Fischbarg, 2010; Tokuda and Yu, 2019). The integrity of the tight junction is critical for proper organ function (Lee *et al.*, 2006, 2018; Liu *et al.*, 2012), and the depletion of the tight junction protein zonula occludins-1 (ZO-1) (Odenwald *et al.*, 2018) or the cytoskeletal regulator Rho-associated protein kinase (ROCK) (Walsh *et al.*, 2001) both result in increased tissue permeability. Renal epithelium in particular are consistently exposed to changing osmotic conditions as solute concentration passing through the kidney is constantly in flux (Beck *et al.*, 1998).

Because the tight junctions regulate osmotic flow across the epithelium, they control the spatial regulation of osmotic stress on the tissue. In addition, polarized renal epithelial tissue confine NKCC1, a member of the NKCC family of ion channels, to the basolateral membrane (Carmosino *et al.*, 2008). This functions to create an osmotic pressure gradient not just across a cell's plasma membrane as we observe in single cells, but a differential pressure gradient across the epithelial tissue, the regulation and cellular response to which is not well understood.

Here, we examine the mechanics of volume regulation in renal epithelial tissue formed from madin darby canine kidney (MDCK) cells and find both a confluence and a tight junction dependence on the tissue's ability to maintain volume homeostasis under hypertonic conditions. We find that small colonies of epithelial tissue exhibit volume homeostasis in response to hyperosmotic stress, in a mechanism reliant on NKCC channels. However, the volume of cells within mature monolayers and acini is acutely suppressed hours after hypertonic conditions were introduced, indicating an inhibition of the process of regulatory volume increase. Disruption of tight junctions in mature monolayers, either through the depletion of ZO-1 or the inhibition of ROCK recover volume homeostasis in response to hyperosmotic stress. Based on these findings,

we report a role of the tight junctions in qualitatively modifying cell volume regulation in epithelial tissue.

3.3 Results

3.3.1 Cell volume in epithelial colonies recovers from hyperosmotic shock via NKCC-mediated regulatory volume increase

To measure the volume response of renal epithelium to osmotic stress, we plated MDCK-II cells sparsely on glass and allowed them to grow for 24 hours, creating small colonies of 4-37 cells and imaged them fluorescently with the addition of CellMask Orange membrane stain. We exposed these colonies to either isotonic (normal DMEM media) or hypertonic (an added 200mM of the synthetic sugar sorbitol) conditions for 3 hours and examined whether the colony was able to recover its isotonic volume (Figure 3.1a), i.e. whether the colony was able to undergo regulatory volume increase (RVI) and maintain volume homeostasis. We observed that the average colony cell volume after a long-term hypertonic shock is slightly but not significantly reduced when compared to the average volume of colonies in isotonic conditions (Figure 3.1b). In addition, when we examine a colony immediately after the addition of hyperosmotic media, we see that there is an initial decrease in the average cell volume, followed by almost complete volume recovery consistent with RVI (Figure 3.1c). In this data, we see a slight increase in average cell volume of the isotonic/control cells immediately following the addition of new media. Initial changes in isotonic volume following the agitation of the wash-in can be seen in much of our time-lapse data and indicates that there is a transient effect of agitation which occurs at a much shorter time scale than the observed regulatory volume increase.

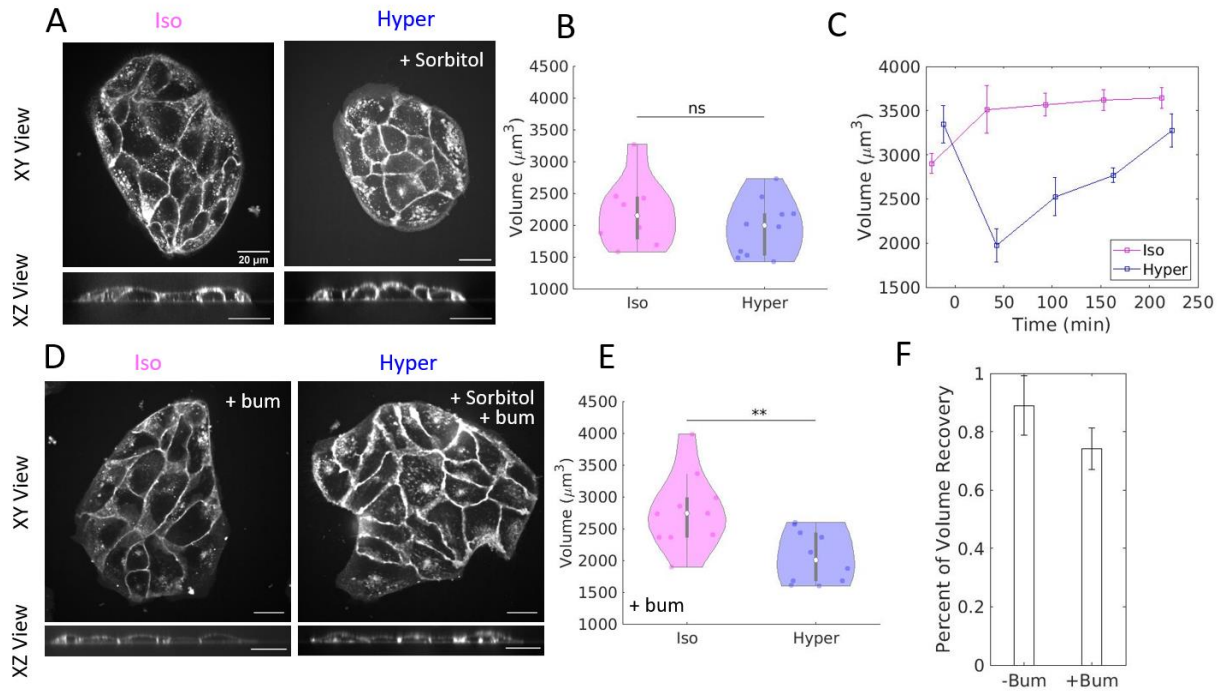

Figure 3.1 Cell volume in epithelial colonies recovers from osmotic shock via NKCC-mediated regulatory volume increase (A) Images of live MDCK-II colonies three hours after an osmotic shock in both a top down (XY) view and a side view (XZ). Cell membrane stained with CellMask Orange. Colonies in isotonic (Iso) conditions are in control media, while colonies in hypertonic (Hyper) conditions have 200µM sorbitol added. Scalebars are 20µm. (B) Violin plot of average colony cell volume in isotonic (n=8 colonies) and hypertonic (n=10 colonies) conditions measured three hours after media exchange. Colonies are 4-37 cells in size. ns=p>0.05 as calculated by the student's t-test. (C) Average colony cell volume in isotonic (Iso) and hypertonic (Hyper) conditions imaged every hour for four hours. Media exchange occurs at t=0min. Error bars represent standard error of the mean. (D) Images of live MDCK colonies three hours after an osmotic shock and the addition of 10µM bumetanide. Cell membrane stained with CellMask Orange. Colonies in isotonic (Iso) conditions are in control media, while colonies in hypertonic (Hyper) conditions have 200µM sorbitol added. Scalebars are 20µm. (E) Violin plot of average colony cell volume in isotonic (Iso) and hypertonic (Hyper) conditions measured three hours after media exchange and the addition of 10µM bumetanide. n=10 colonies each with 5-37 cells. **=p<0.01 as calculated by the student's t-test. (F) Percent of volume recovery for colonies with and without the addition of 10µM bumetanide. Volume recovery is measured by the ratio of mean hypertonic volume to mean isotonic volume three hours following media exchange. Error bars represent standard error of the mean.

We next wanted to confirm that the volume recovery observed is due to ion channel activity as expected for RVI. MDCK cells express exclusively the Na+-K+-Cl- cotransporter 1

(NKCC1), which has been found to localize basolaterally in epithelial tissue (Mykoniatis *et al.*, 2010; Koumangoye *et al.*, 2018). We treated colonies with 10μM of bumetanide, a Na+-K+-Cl-cotransporter (NKCC) inhibitor and saw that volume homeostasis in response to hypertonic conditions is abrogated (Figure 3.1d). Cell volume is significantly reduced after 3 hours of hypertonic conditions in the presence of NKCC inhibitor, compared to cells in isotonic conditions (Figure 3.1e). After 3 hours, NKCC inhibition under hyperosmotic conditions resulted in a reduction in average colony cell volume to 74% of isotonic cell volume, while control cells were able to recover to 89% of their initial volume (Figure 3.1f). This indicates that small colonies of MDCK cells exhibit volume homeostasis mediated by NKCC channels, consistent with well-established regulatory volume increase mechanism that maintains volume homeostasis in single cells in response to hyperosmotic stress

3.3.2 Characterization of monolayer volume and volume variation

To explore changes in cell volume occurring in mature epithelium, we developed protocols to characterize the changes in cell volume. MDCK-II cells are plated densely on glass slides and grown for 48 hours with 100% confluency achieved after 24 hours, creating a mature epithelial tissue (Figure 2.1a). We then use the methods described in section 2.3.1 to measure the average cross-sectional area and approximate average cell volume in a monolayer as the average cross-sectional area multiplied by the average monolayer height (Figure 2.1 b,c).

MDCK monolayers exhibit natural variation in both cell density and cell volume (Zehnder *et al.*, 2015) and the scale of this variation can be seen within a single 135x175μm^2 field of view (Figure 2.1 d,e). We chose this range to average over because the natural variation

in local volume is consistent with the average variation in volume between one monolayer and another (Figure 2.1f), allowing us to treat each field of view's local volume as independent.

3.3.3 Mature epithelial tissue does not recover from a long-term osmotic shock

We next perform iso and hyper-tonic experiments on mature epithelium formed by plating MDCK cells at high density onto glass and incubating for 48 hours. Under these conditions, tight junctions form in this polarized model epithelial tissue to facilitate well-characterized barrier function (Lee *et al.*, 2006; Fischbarg, 2010). In this condition, the hyperosmotic media presumably remains confined to the apical cell surface. Upon media exchange to hypertonic conditions, we discover that that average volume of the cells decreases by 20-35% and does not recover over time such that the epithelial height and volume remain permanently reduced even after three hours (Figure 3.2a-c).

To determine whether mature epithelial tissue reacts similarly independent of configuration, we performed these experiments in MDCK acini in collagen gel. MDCK acini are confluent cysts that are formed by seeding cells sparsely within collagen gel and incubating for eight days. Acini are polarized with the apical surface at the inner surface of the cyst known as the lumen and the basal surface facing the external media. Thus, for acini, the basal and basolateral cell surfaces are exposed to the exchanged media and the barrier prevents transport to the apical surface. Similar to confluent monolayers, the hyperosmotic shock permanently reduces volume of cells within acini by 34% (Figure 3.2 d and e).

Comparing these data, hyperosmotic shock leads to 20-35% cell volume reduction in both confluent monolayers plated on glass and MDCK acini grown in collagen gel. This volume

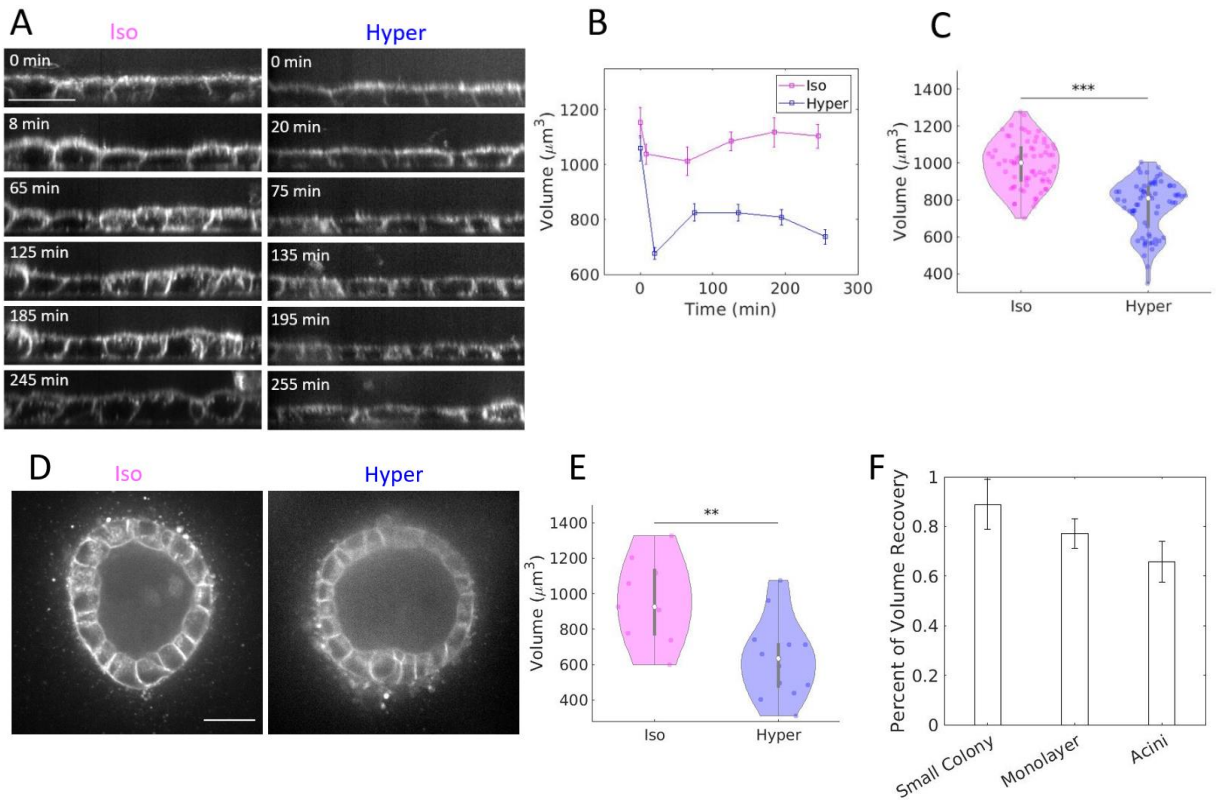

Figure 3.2: Mature epithelial tissue does not recover from a long-term osmotic shock (A) Images of live XZ views of MDCK monolayers taken over five hours. Cell membrane stained with CellMask Orange. Monolayers in isotonic (Iso) conditions are in control media, while those in hypertonic (Hyper) conditions have 200µM sorbitol added. Scalebars are 20µm. (B) Average cell volume in isotonic (Iso) and hypertonic (Hyper) conditions imaged every hour for four hours. Media exchange occurs at t=0 min. Error bars represent standard error of the mean. n=10 fields of view from one monolayer. (C) Violin plot of average monolayer cell volume in isotonic and hypertonic conditions measured three hours after media exchange. n=70 fields of view across 7 separate monolayers of varying density with 100-165 cells per field of view. ***=$p<0.0001$ as calculated by the student's t-test. (D) Cross sections of hollow MDCK acini grown in collagen gel. Cell membrane stained with CellMask Orange. Acini in isotonic (Iso) conditions are in control media, while those in hypertonic (Hyper) conditions have 200µM sorbitol added. Scalebars are 20µm. (E) Violin plot of average acini cell volume in isotonic (n=9 acini) and hypertonic (n=13 acini) conditions measured three hours after media exchange. **=$p<0.01$ as calculated by the student's t-test. (F) Volume recovery is measured by the ratio of mean hypertonic volume to mean isotonic volume three hours following media exchange. Error bars represent standard error of the mean.

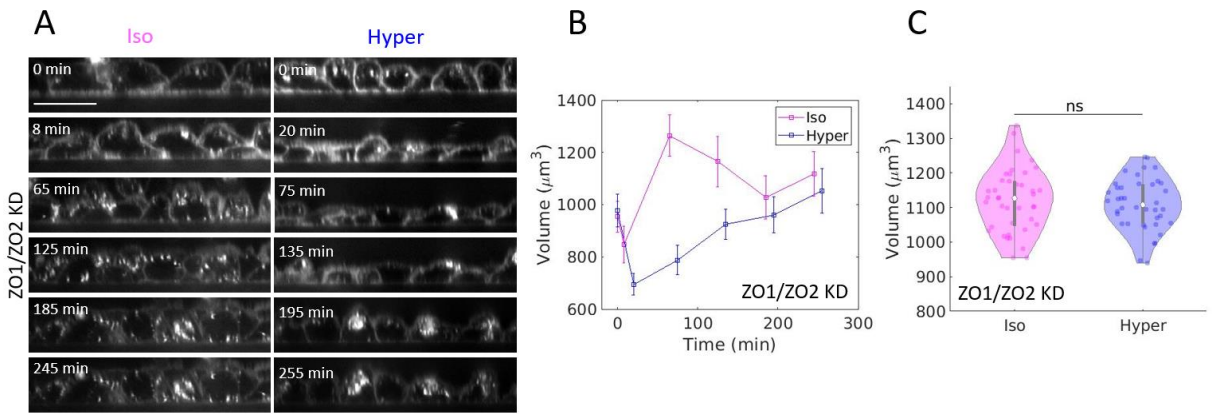

Figure 3.3: The tight junction protein ZO-1 is required to prevent volume recovery in mature epithelial tissue (A) Images of live XZ views of ZO-1/ZO-2 knock-down (KD) MDCK monolayers taken over five hours. Cell membrane stained with CellMask Orange. Monolayers in isotonic (Iso) conditions are in control media, while those in hypertonic (Hyper) conditions have 200μM sorbitol added. Scalebars are 20μm. (B) Average cell volume of ZO-1/ZO-2 KD monolayers in isotonic (Iso) and hypertonic (Hyper) conditions imaged every hour for five hours. Media exchange occurs at t=0 min. Error bars represent standard error of the mean. n=10 fields of view in one monolayer. (C) Violin plot of average ZO-1/ZO-2 KD monolayer cell volume in isotonic and hypertonic conditions measured three hours after media exchange. n=40 fields of view across 4 separate monolayers of varying density with 99-150 cells per field of view. ns=p>0.05 as calculated by the student's t-test.

reduction is not seen in MDCK colonies, which recover to 90% of their isotonic volume within three hours (Figure 3.2f). This allows us to conclude that the NKCC-mediated regulatory volume increase after hyperosmotic shock that preserves volume homeostasis in single cells and small colonies is hampered in confluent renal epithelial tissue.

3.3.4 Tight junctions are required to prevent volume recovery in mature epithelial tissue

We speculated that the differences in volume regulation between small colonies and mature epithelium might arise from tight junctions. Tight junctions, which are critical for barrier function, are not observed in small colonies and assemble in rho-kinase (ROCK) and ZO-1

mediated processes in confluent and polarized epithelium (Hirase *et al.*, 2001; Walsh *et al.*, 2001; Odenwald *et al.*, 2018). To assess this, we first formed monolayers and acini from MDCK-II cells with the tight junction proteins ZO-1 and ZO-2 knocked-down (Choi *et al.*, 2016). Interestingly, we found that that cell volume recovered after hyperosmotic shock in these cells. Similar to that observed for small colonies, the volume of ZO-1/ZO-2 deficient cells in mature epithelium acutely decreased but recovered over the subsequent several hours (Figure 3.3 a and b). After 3 hours, the average cell volume is not significantly different than those in isotonic media (Figure 3.3c). Thus, ZO-1 is critical to the differing volume regulation observed in confluent epithelial tissue.

Another means to alter tight junction assembly is through inhibition of ROCK activity (Hirase *et al.*, 2001; Walsh *et al.*, 2001) with the addition of 25μM of the ROCK inhibitor Y-27632 during monolayer formation. We find that ROCK inhibition also recovered the process of regulatory volume increase of cells within confluent monolayers or acini that are subjected to hyperosmotic shock (Figure 3.4 a-e) Taken together, these data show that ROCK inhibition facilitates an 88% volume recovery in monolayers, and 94% for acini (Figure 3.4f). And so, we are able to conclude that functional tight junctions are critical for the different response to hyperosmotic shock in mature epithelium than in isolated cells.

3.4 Discussion

The mechanics regulating cell volume homeostasis are vital to the proper functioning of epithelial tissue in animals. Here we find that small colonies of renal epithelial tissue maintain their volume homeostasis and undergo NKCC dependent regulatory volume increase in a manner consistent with the pump-leakage model found in many types of individual cells. Here we find

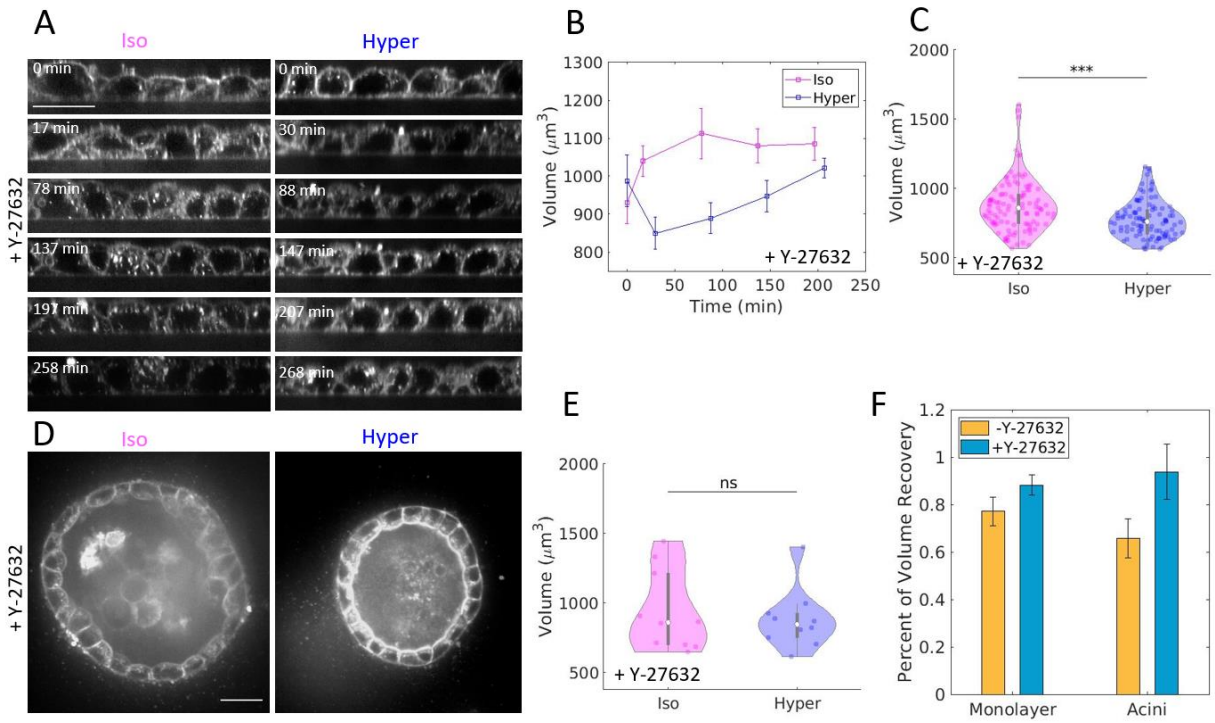

Figure 3.4: ROCK is required to prevent volume recovery in mature epithelial tissue (A) Images of live XZ views of MDCK monolayers with 25μM of the ROCK inhibitor Y-27632 taken over four hours. Cell membrane stained with CellMask Orange. Monolayers in isotonic (Iso) conditions are in control media, while those in hypertonic (Hyper) conditions have 200μM sorbitol added. Scalebar is 20μm. (B) Average cell volume of monolayers with 25μM Y-27632 in isotonic and hypertonic conditions imaged every hour for four hours. Media exchange occurs at t=0min. Error bars represent standard error of the mean. n=10 fields of view in one monolayer. (C) Violin plot of average monolayer cell volume with 25μM Y-27632 in isotonic and hypertonic conditions measured three hours after media exchange. n=110 fields of view across 11 separate monolayers of varying density with 40-160 cells per field of view. ***=$p<0.0001$ as calculated by the student's t-test. (D) Cross sections of hollow MDCK acini grown in collagen gel. with 25μM Y-27632 added three hours prior to imaging. Cell membrane stained with CellMask Orange. Acini in isotonic (Iso) conditions are in control media, while those in hypertonic (Hyper) conditions have 200μM sorbitol added. Scalebars are 20μm. (E) Violin plot of average acini cell volume in isotonic (n=10 acini) and hypertonic (n=10 acini) conditions measured three hours after media exchange. ns=$p>0.05$ as calculated by the student's t-test. (F) Volume recovery is measured by the ratio of mean hypertonic volume to mean isotonic volume three hours following media exchange. Error bars represent standard error of the mean.

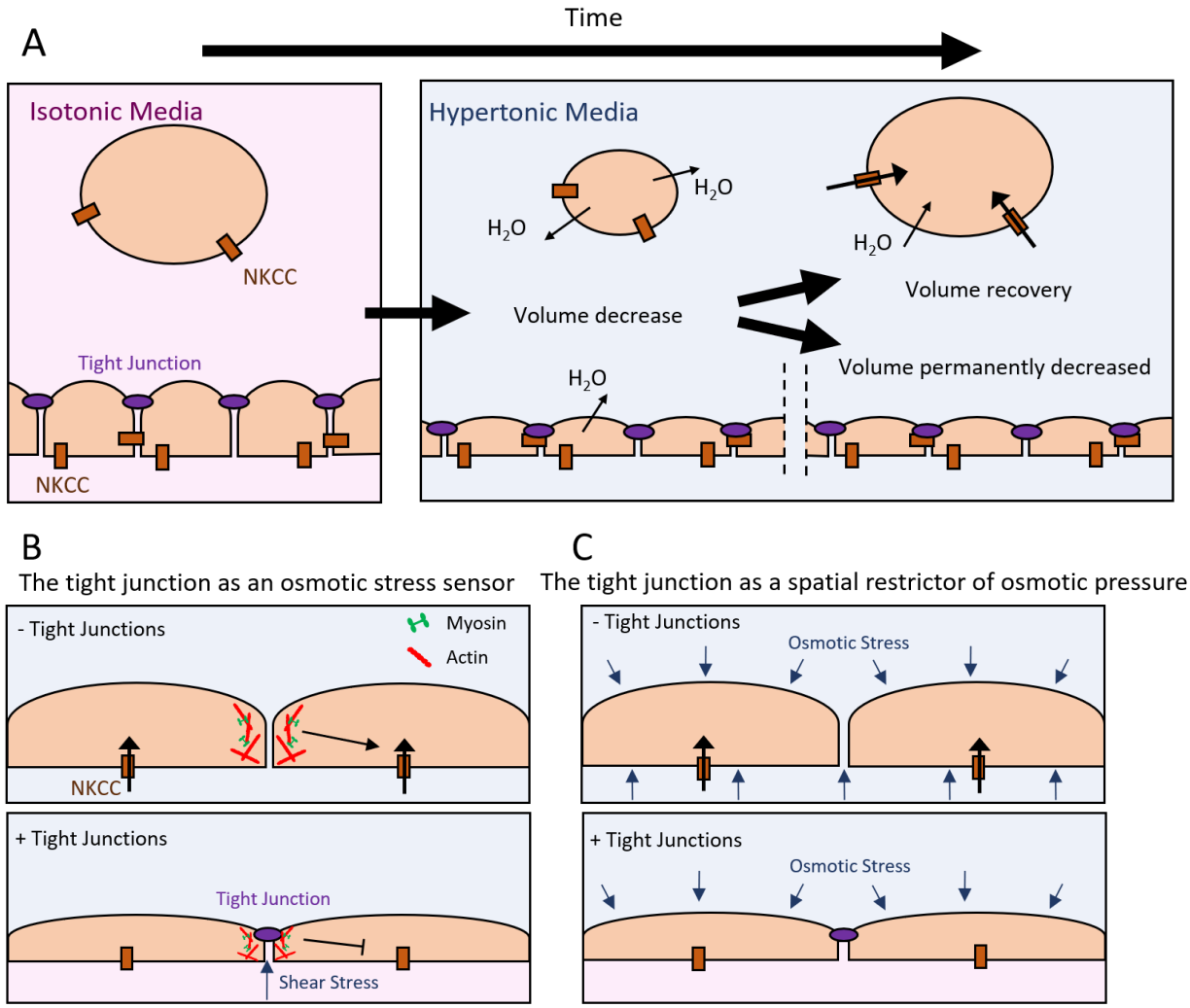

Figure 3.5: Tight junction regulation of volume homeostasis (A) A schematic depicting the dynamics of volume homeostasis in single cells and in mature epithelial tissue. With the addition of hyperosmotic media, single cells first shrink in volume as water exits the cell to the surrounding media. Over time, NKCC ion channels pump ions back into the cells, allowing water to follow the osmotic gradient and restore the cell's volume. A mature epithelium exposed to hypertonic media also reduces in volume as water exits into the surrounding media. However, the NKCC ion pumps are inactive and no RVI occurs. (B) A schematic of the potential role the tight junction plays as an osmotic stress sensor. In the case of epithelium with permeable, i.e. leaky, tight junctions (upper), the absence of the tight junction allows volume homeostasis to occur through NKCC ion channels. In confluent tissue with functioning tight junctions (lower), the stress across the tight junction is transmitted to the mechanosensitive actomyosin cytoskeleton. This results in the inhibition of volume homeostasis, and cell volume does not recover. (C) A schematic of the possible role the tight junction plays as a spatial restrictor of osmotic stress. In this model, epithelia with permeable tight junctions (upper) have zero osmotic gradient across the epithelium, and thus are surrounded at all membranes by hyperosmotic stresses, promoting regulatory volume increase reminiscent of single cell volume homeostasis.

Figure 3.5 Continued: In contrast, epithelia with impermeable tight junctions (lower) create a barrier preventing hyperosmotic media from reaching across to both sides of the epithelia, creating a nonzero osmotic gradient, and spatially restricting where osmotic pressure is applied to the cells in the epithelium.

this is not the case for mature epithelium. Following a long-term hyperosmotic shock, the volume of individual cells within mature epithelium is permanently decreased (Figure 3.6a). Thus, regulatory volume increase that allows for cell volume homeostasis in response to hyperosmotic stress does not occur in mature monolayers. This lack of RVI is dependent on the tight junction assembly. And so, we report an important role of the tight junctions in assisting cell volume regulation in epithelial tissue. Importantly, a relationship between the tight junctions and the NKCC family of ion channels has been previously reported. Results from Koumangoye et al., 2018 show that when NKCC1 is modified in MDCK cells, ZO-1 no longer localizes to the apical junction, instead distributing along lateral epithelial junctions. These results also indicate that the positioning of NKCC1 ion channels with respect to the osmotic pressure is not the primary driver of this response. We know that NKCC1 localizes basolaterally in MDCK-II tissue (Mykoniatis *et al.*, 2010; Koumangoye *et al.*, 2018) and so we would expect these ion channels to be sequestered away from regions of high osmotic pressure in our monolayer samples and exposed to regions of high osmotic pressure in our acini samples. Because we see similar volume recovery in both samples, we can conclude that the specific tissue membrane, either apical or basal, exposed to osmotic stress is not a significant concern for epithelial volume regulation.

Here, we surmise two possible explanations for how the tight junctions may be playing this regulatory role in epithelial tissue. One involves the tight junction as an osmotic sensor, able to communicate hydrostatic pressure across the barrier to the cytoskeleton, while the other

considers the osmotic barrier created by the tight junction and how it affects osmotic pressure across epithelial tissue.

It has been previously hypothesized that that the tight junction acts directly in mechanotransduction of osmolarity gradients and regulation of cell volume (Tokuda and Yu, 2019). Osmotic stress locally impacts stress at the tight junction and via action on mechanosensitive cytoskeleton may impact the activity of ion channels regulating regulatory volume increase (Figure 3.6b). Without functioning tight junctions, sub-confluent or inhibited tissue may lose its ability to detect the osmotic pressure gradient due to the hypertonic conditions as an immature or disrupted tight junctional structure would cause increased paracellular transport and the absence of any shear stress between the apical and basal surfaces of the tissue, resulting in the downstream effect of active NKCC ion channels facilitating RVI. In contrast, fully confluent and uninhibited epithelial monolayers sense this stress at their "leak-proof" tight junctions, and this results in the suppression of volume homeostasis through as yet unknown intercellular signaling. This model is supported by evidence that hydrostatic pressure on the tight junction affects both the localization of the tight junction protein claudin-1, which instead dispersed to the cytoplasm, and lateral actin structure (Tokuda *et al.*, 2009), meaning that stress on the tight junction cause tangible changes to the actin cytoskeleton. In turn, the actin cytoskeleton has been shown to regulate and organize variety of ion channels and related transporters associated with volume regulation (Papakonstanti *et al.*, 2000; Mazzochi *et al.*, 2006). Specifically, in airway epithelial tissue actin stabilization has been found to activate NKCC1 channels through the serine-threonine protein kinase PKC-δ (Liedtke et al., 2003).

An equally interesting explanation is that an intact tight junction serves to confine the osmotic pressure to only a small subsection of the epithelial membrane (Figure 3.6c). Meaning

that instead of an epithelial cell being surrounded by hyperosmotic pressure at all membranes as we see when examining single cell volume regulation, the tight junction restricts that osmotic pressure to only one side of the epithelial tissue and impacts regulatory volume increase. This hypothesized mechanism poses that geometrically constrained osmotic stress across the apical/basal surfaces of the tissue affects cellular volume regulation differently than osmotic stress across the cellular membrane. In our results, mature monolayers with functional tight junctions are only exposed to hyperosmotic pressure at the apical membrane and acini are only exposed at the basolateral membrane. Thus, our data does not indicate that the geometry of the osmotic shock is important for this response, as one might expect given known localization of the NKCC1 channel to the basolateral surface (Mykoniatis *et al.*, 2010; Koumangoye *et al.*, 2018) Instead, it suggests cells react differently to osmotic pressure gradients across the apical-basal plane than when to those across the cell membrane.

Future work is required to understand the mechanisms controlling of volume regulation in mature epithelium, including how tight junctions impact NKCC ion channel activity. The details of the relationship between NKCC activity and tight junctions have been linked to disfunction and inflammation in both the gut (Koumangoye *et al.*, 2020) and the brain (Wang *et al.*, 2022) where activating NKCC1 related pathways was found to disrupt the tight junctions of the blood brain barrier. And so, we are able to conclude that tight junctions in mature epithelium suppress volume homeostasis and, as such, cell volume regulation in epithelial tissue is qualitatively different from that of single cells. Given the known consequences of cell volume regulation for their physiology, these results have significant consequences for control of mechanotransduction pathways in epithelial tissue.

3.5 Methods

Cell culture: MDCK-II cells were cultured in Dulbecco's Modified Eagle's Medium (DMEM) and supplemented with 10% fetal bovine serum (FBS) (ThermoFisher Scientific), 2mM L-glutamine (Invitrogen), and penicillin-streptomycin (Invitrogen). Cells were incubated in a humidified environment at 37C and 5% $C0_2$. MDCK ZO-1/ZO-2 KD cells were generously provided by Mark Peifer (University of North Carolina).

Osmotic shock treatment: Hyperosmotic media was created through the addition of 200 mOsm of sorbitol (Phytotechnology Laboratories) to 290 mOsm DMEM media to make 490 mOsm hypertonic media.

Sample creation: To create small colonies, MDCK cell were plated sparsely to coat the glass bottom of a 4-well chamber (Ibidi) and incubated for 24 hours. To create a mature monolayer, MDCK cells were plated densely to coat the glass bottom of a 4-well (for timelapse imaging) or 8-well (for non-timelapse imaging) chamber (Ibidi). The cells were then incubated for 48 hours with a change of media at 24 hours. Acini were formed by sparsely plating MDCK cells in 2mg/mL collagen gel for 8 days with the addition of serum starve (1% FBS) DMEM changed every 48 hours. Inhibitors and osmotic treatments were added 3 hours prior to imaging. ROCK inhibited cells were treated with 25μM Y-27632 (Sigma) 3 hours before live imaging. NKCC inhibited cells were treated with 10μM Bumetanide (Sigma) 3 hours before live imaging.

Microscopy and live cell imaging: 2μl/ml of CellMask Orange (Invitrogen) was added to samples 30 minutes prior to imaging to stain the cell membrane. Samples were imaged on an inverted T-E microscope (Nikon) with a confocal CSU-X spinning disk (Yokogawa Electric Corporation), a stage controller (Prior), and a CMOS camera (Zyla-Andor). Metamorph software was used to control the microscope and collect images. A stage incubator (Chamlide and Quorum

Technologies) with CO-2, humidity, and temperature control was used for timelapse experiments while a stage heater (Nevtek, ASI 400) was used for non-timelapse experiments. A 561 nm laser (MPB Communications, VFL-P Series) was used to illuminate the CellMask Orange stain. Images were acquired using a 60x Plan Apo NA water immersion objective with a NA of 1.20 and a WD of 0.31-0.28 (Nikon). Three-dimensional images were collected using z-stacks of 0.25μm steps.

Height and volume analysis: Both ImageJ and Matlab were used for image analysis of monolayer height and volume. Average monolayer height (excluding ZO1/ZO2 KD monolayers) was measured using the method described above in section 2.5. Volume measurements for ZO-1/ZO-2 KD monolayers, as well as all colonies and acini, were found using an alternate method to that described above. For ZO-1/ZO-2 KD cells and colonies this is because their extended apical domain is not well characterized by the assumption that the apical membrane is flat, and for acini it is because the cells are not grown on a flat surface. In these cases, average cell volume was found by measuring cell junction height, maximum cell height, and basal area for sample cells. This allowed us to model the volume of the cell as a cylinder that is the height of the cell junction length plus a hemisphere on top.

Violin Plots: The width of each colored region represents volume kernel density which is an estimation of the probability density function of the average cell volume. The white point represents the median cell volume for all colonies measured, and the grey bar represents the interquartile range, meaning the middle 50% of the volume range.

Quantification and Statistical analysis: Image analysis and quantification was performed in Fiji, Excel, and Matlab. Matlab was used to perform statistical analysis and calculate statistical

significance using two-tailed student t-tests where ns=$p>0.05$, *=$p<0.05$, **=$p<0.01$, and ***=$p<0.0001$.

Chapter 4: Preferential stimulation of calcium in colony and wound edges during electrotaxis of epithelial monolayers

4.1 Preface and Abstract

4.1.1 Preface

The following chapter is work which grew out of a collaboration with Professor Sihong Wang and Yang Li at the University of Chicago. Through this collaboration we set out to set up a system capable of sustained electrotaxis of in vitro epithelial tissue cells in order to test the wound healing properties of biocompatible soft polymer electronics synthesized by the Wang lab. While this original goal remains an ongoing project under collaboration, the system for electrotaxis and electrical stimulation developed jointly by the Gardel and Wang labs resulted in the following fascinating study of intracellular calcium stimulation during electrotaxis.

4.1.2 Abstract

Electric fields have long been understood to direct the motion of migratory cells in a process known as electrotaxis. While this process is known to be effective in manipulating the motion of cells, the exact nature of how the microenvironment influences cell motility during electrotaxis is not well characterized. Intercellular calcium has long been thought to play a role in electrotaxis and its reorganization under an electric field is one of several signals thought to mediate cell motility in these conditions. Here, we examine the effects of an electric field on intercellular calcium of epithelial colonies and monolayer wounds. We find that calcium is enriched at these colony edges and monolayer wound regions even before an electric field is applied. We also show that intercellular calcium increases more intensely in response to an electric field at these edges than it does further into the monolayer.

4.2 Introduction

Living cells respond to the application of an electric field. Stimulus from an electric field is essential for processes from neural activation in the brain (Armstrong and Hille, 1998) to the well characterized function of exciting cardiac tissue (Geselowitz, 1973; Fozzard, 1977; Elmas, 2016). One increasingly well studied effect of electric fields on living tissue is the phenomenon of electrotaxis. Electrotaxis, also known as galvotaxis, is the directional motion of living cells in response to an electrical stimulus (Cortese *et al.*, 2014). It is well known to be extremely relevant in the fields of wound healing (Tai *et al.*, 2009; Li *et al.*, 2013), cancer metastasis (Li *et al.*, 2013; Cortese *et al.*, 2014; Oudin and Weaver, 2016), and neural migration during the development of the central nervous system (Yao *et al.*, 2011). Despite cell migration due to electrotaxis being observed over 150 years ago when German scientist Max Verworn first observed that most protists will crawl either towards the anode or the cathode when an electric field is applied to a sample (Pearl, 1900), much of the process has yet to be fully understood.

While we still have much to discover about exact processes which underlay electrotaxis directed cell migration and multiple theories have been published over the years, our current understanding is that a combination of factors are affecting the cellular microenvironment and acting as a migratory stimuli, including gradients of various extracellular solutes, direct rearrangement of charged particles in the cytoplasm, and effects on voltage gated ion channels and other surface receptors (Cortese *et al.*, 2014; Taghian *et al.*, 2015). However none of these environmental cues have been fully able to explain the mechanism by which cell migration is stimulated and controlled, and there is much still to be understood in terms of underlying molecular mechanisms and the roles of various regulatory pathways (Cortese *et al.*, 2014).

Understandably, this inducible directional migration is of particular interest to those studying wound healing. Direct application of an electric field to wounds in in-vitro immortalized epithelial tissue (Song *et al.*, 2007; Zajdel *et al.*, 2020) as well as mice (Nuccitelli *et al.*, 2008; Wang *et al.*, 2019), rat (Long *et al.*, 2018; Oliveira *et al.*, 2019; Kao *et al.*, 2022), and human skin wounds (Nuccitelli *et al.*, 2008) show faster healing times and reduced inflammation in the region (Tai *et al.*, 2009; Cheah *et al.*, 2021). While this technology is considered an extremely exciting field, electrical stimulation for wound-care is not widely practiced and with only a handful of clinical trials looking into its therapeutic use for skin graft healing (Cheah *et al.*, 2021), diabetic ulcer treatment (Miller *et al.*, 2017; Rajendran *et al.*, 2021) , and burn treatment (Gomes *et al.*, 2018).

One aspect of electrotaxis that has been well studied and described is the differential response of cells in a tissue compared to single cells. One study found that collective migration of cells in a tissue is fundamentally different than that of individual cells, with isolated mammary epithelial cells requiring more than twice the voltage/cm compared to cells in colonies which are experiencing cell-cell interactions (Lalli and Asthagiri, 2015). This indicates that collective migration of cell in a tissue are more sensitive to electric fields. The study also reported that these mammary cells migrating collectively in colonies take longer to start showing directed motion when exposed to an electric field than individual cells, but that when they ultimately do undergo electrotaxis the motion is more directed overall than isolated cells (Lalli and Asthagiri, 2015). Another study found that this is also true for MDCK cells as they show that larger and larger colonies see more and more aligned directed motion, and that disruption of the adherens junction or the tight junction reduced this affect and inhibited the directedness of motion during

electrotaxis (Li *et al.*, 2012). Ultimately these data suggest that cell-cell adhesion plays an important role in collective cell migration during electrotaxis.

This is corroborated by traction force data observed during collective migration due to electrotaxis. Traction force microscopy is a technique for measuring the stresses that samples exert onto the substrate they rest on and works by microscopically imaging deformations to an elastic substrate both with and without the object present (W. Style *et al.*, 2014). During collective migration due to electrotaxis, we see that it's the leading edges of non-confluent monolayers which deform the substrate the most (Li *et al.*, 2012). This implies that it is the edges of the monolayer which provides the majority of the forces necessary to lead the increased collective migration seen in cells within a tissue.

Here, we find a fascinating role for calcium during electrical stimulation. Calcium is one of the ions often hypothesized as a core mechanism for electrotaxis (Cortese *et al.*, 2014) and it's inflow into cells through voltage gated channels in response to electrical stimulation is well documented (Pesqueira *et al.*, 2017; Cole and Gagnon, 2019). We find increased intracellular calcium at wound edges and the edges of monolayers independent of electrical stimulation. In addition, we show that intercellular calcium increases more intensely in response to an electric field at these edges than it does further into the monolayer, implicating the role of calcium at these edges in a tissue's collective motility. We also show that cells grown on soft gel substrates do not experience these edge effects with intracellular calcium not strongly enriched at wound and colony edges and cells throughout the tissue showing strong responses to the application of an electric field, indicating that disruption to adhesion complexes affects the calcium response in a tissue.

4.3 Results

4.3.1 Electrotaxis induced by a DC electric field in MDCK monolayers.

In order to study the application of a DC electric field on MDCK epithelial tissue, we designed an agar bridge-based system capable of being setup in an incubator on a fluorescent microscope (Figure 4.1 a, b). The ends of the agar bridge were placed 1 cm apart from each other and epithelial cells in the sample were imaged in the center of this 1 cm wide region. To make the sample we plated MDCK-II cells densely on glass and allowed them to grow for 48 hours, into a confluent monolayer and imaged them fluorescently with the addition of a CellMask Orange membrane stain over the course of 10 hours imaging every 15 minutes under the application of 2V/cm of a DC electric field generated by the attached power supply (Figure 4.1c). We see that over the 10 hours, the cells collectively moved in the direction of the anode in the electric field, migrating between 40 and 160 μm in that time (Figure 4.1d). This motion is highly directed and out of the 20 cells tracked, all migrated in a direction within 30° of the electric field (Figure 4.1e). Together, this data describes the responsiveness of MDCK samples to collective migration during electrotaxis within this experimental setup.

4.3.2 Transient intracellular calcium spikes are present in cells throughout a tissue and are consistently enriched at colony and wound edges.

Ultimately, we want to be able to describe the role of calcium in organizing the collective dynamics seen in epithelial tissue under the influence of an electric field. These collective dynamics are can be seen in all types of epithelial tissue but are strongest in mature epithelial monolayers and significantly weaker in single cells and small colonies (Li *et al.*, 2012; Lalli and Asthagiri, 2015). To do this we employed the calcium probe fluo-8 to record the relative flux of

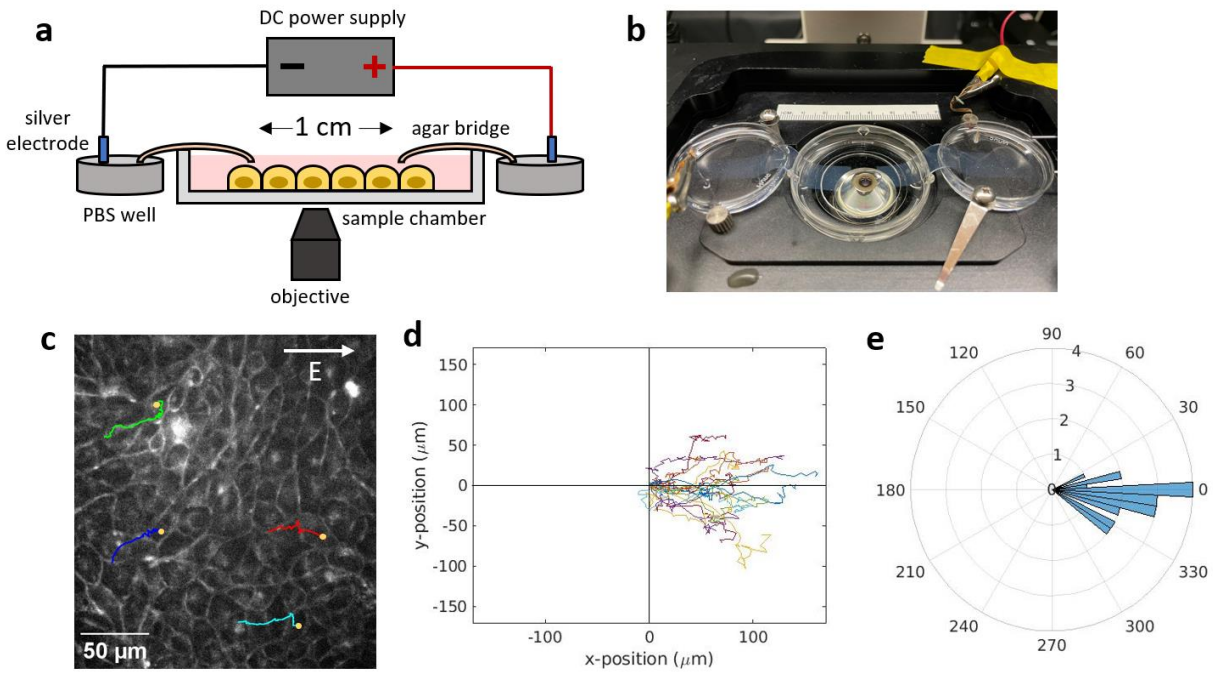

Figure 4.1: Electrotaxis induced by a DC electric field in MDCK monolayers (a, b) A depiction of the imaging setup as a diagram (a) and an image (b). An electric field is applied to live cells within an imaging chamber using a DC power supply with silver electrodes connected to two PBS wells on either side of the sample. Strips of agar connect the PBS well to the sample chamber and are placed to be 1 cm apart on top of the cells. (c) Cells in a monolayer undergoing electrotaxis. 2V/cm DC electric field was applied to the sample over 10 hours. Sample was imaged evert 15 minutes. Colored lines represent the path of four cells in the tissue. Yellow circles mark each cell's position after 10 hours. (d) x- and y-positions of 20 different cells in the tissue relative to their position at the start of imaging. (e) Polar histogram of the total direction traveled by each of these 20 cells.

intracellular calcium of cells in the tissue. Imaging MDCK monolayers over the course of 2 minutes showed transient calcium events of different intensities and at different times within cells in the monolayer (Figure 4.2 a, b). By examining the peak intensity for each cell compared to the baseline intensity, we found that some cells in the monolayer experienced strong calcium transient events during this time period, while other cells did not (Figure 4.2c). This is consistent with similar studies, which report a wide variety of peak intensities and time between spontaneous stimulation of calcium in MDCK monolayer tissue (Geyti *et al.*, 2008; Schaumann, 2020).

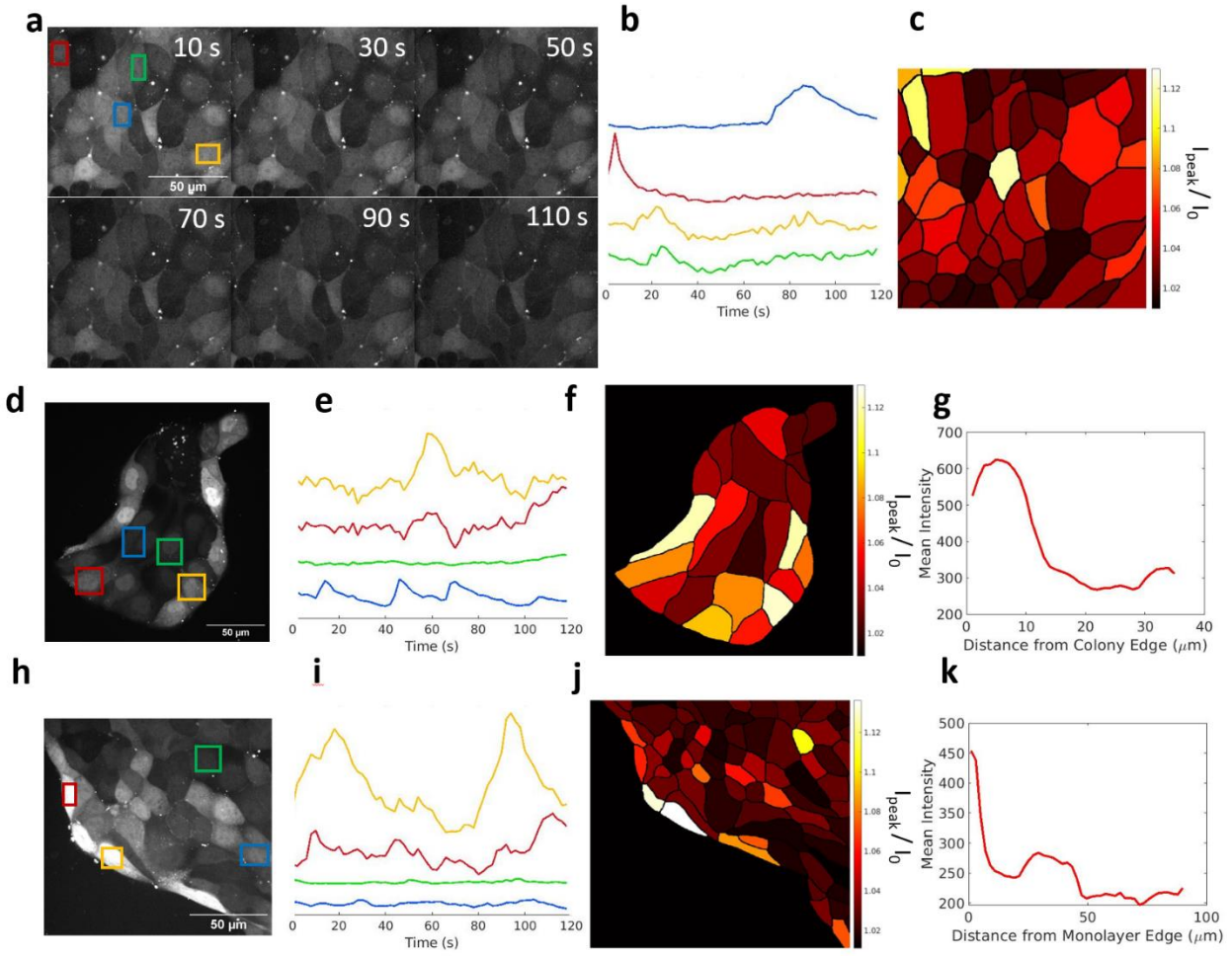

Figure 4.2: Transient intracellular calcium spikes are present in cells throughout a tissue and are consistently enriched at colony and wound edges (a) Images from a video of live MDCK cells grown into a monolayer and dyed with 2µM fluo-8, an intracellular calcium marker. Images taken every second for 120 seconds. (b) Intensity of calcium marker within the cells marked by the corresponding box in Figure a. Transient calcium spikes can be observed. Photobleach corrected. (c) Segmented image of the monolayer showing the peak intensity measured throughout the video compared to the mean background intensity for each individual cell. (d) A still from a video of a live MDCK colony dyed with fluo-8. Images taken every second for 120 seconds. (e) Intensity of calcium marker within the cells marked by the corresponding box in Figure d. Transient calcium spikes can be observed. Photobleach corrected. (f) Segmented image of the colony showing the peak intensity measured throughout the video compared to the mean background intensity for each individual cell. (g) Measurement of initial colony calcium intensity compared to that position's distance from the edge of the colony. (h) A still from a video of a live MDCK wound edge dyed with fluo-8. Images taken every second for 120 seconds. (i) Intensity of calcium marker within the cells marked by the corresponding box in Figure h. Transient calcium spikes can be observed. Photobleach corrected. (j) Segmented image of the wound edge showing the peak intensity

Figure 4.2 Continued: measured throughout the video compared to the mean background intensity for each individual cell. (k) Measurement of initial wound calcium intensity compared to that position's distance from the edge of the wound.

Unlike mature monolayer tissue, small colonies of MDCK cells show a distinct pattern when it comes to calcium distribution and transient calcium events. We see that calcium is strongly and consistently enriched in cells at edge of colonies (Figure 4.2 d). In addition, when we examine calcium transient peaks, we find that while we continue to see some transient events in cells at the center of the small colony, cells at the edge of the colony consistently exhibit strong calcium transient events during the two-minute time period imaged (Figure 4.2 e, f), indicating that calcium events are stronger and more consistent at these edges. When we quantify this through measuring the relative intensity of calcium in the colony compared to the distance from the edge of the colony, we find that there is a large peak in calcium intensity in cells close to the colony edge that quickly drops of as we go further into the center of the collection of cells.

Similarly, we examined how calcium behaved not at colony edges, but at artificial wound edges. To do this we developed samples of cells grown withing a 5x5 cm square through the use of a PDMS mask. When we remove this mask two hours prior to imaging, it disturbs the edges of the large colony, making an artificial and highly controllable wound edge. These wound edges behave comparably to the colony edges with enriched calcium at the edges (Figure 4.2 h), as well as stronger and more consistent transient calcium events in cells along the wound edge (Figure 4.2 i, j). When we quantify this calcium enrichment at the edge, we once again see that there is a large peak of calcium intensity right at the wound edge that falls off further into the large colony of cells (Figure 4.2 k). Together, this data indicates a role for transient calcium spikes in colony and wound edges that is not found further into the center of the tissue.

4.3.3 Intracellular calcium is preferentially stimulated at wound and colony edges by the application of a 10V/cm DC electric field.

Now that we have established the existing nature of calcium transient events and unique distribution of calcium at colony and wound edges, we're interested in probing how an electric field stimulates and regulates intracellular calcium to better understand the role that calcium might play in collective electrotaxis behavior. To do this, we applied a 10V/cm electric field for 20 seconds, turned it off for 20 seconds, and then pulsed the DC electric field a second time for 20 seconds (Figure 4.3a, b). Applying this electric field twice over the course of one timelapse experiment allows us to examine whether this event was likely a spontaneous calcium transient event, or whether we expect that an event was stimulated by the applied electric field because it occurred following both applications of the electric field.

What we find when we apply an electric field to colonies and wound edges, is that the electric field preferentially stimulates intracellular calcium at those colony and wound edges. Cells further from the edges do not experience consistent stimulation of a transient calcium event, while cells at and close to the edges are much more likely to have a strong increase in fluo-8 calcium intensity during the application of the electric field (Figure 4.3 c, g). Additionally, when we examine the mean intensity change in the calcium indicator signal just before and during the application of the first electric field, we find that it is preferentially cells at or near the edges of the field which experience increased intracellular calcium (Figure 4.3 d, h). When we examine the percent intensity change after the application of an electric field at different distances from the colony or wound edges, we find that there is a peak in calcium activation that occurs near to the edges which then rapidly drops further from the edge (Figure 4.3 e, i). This is

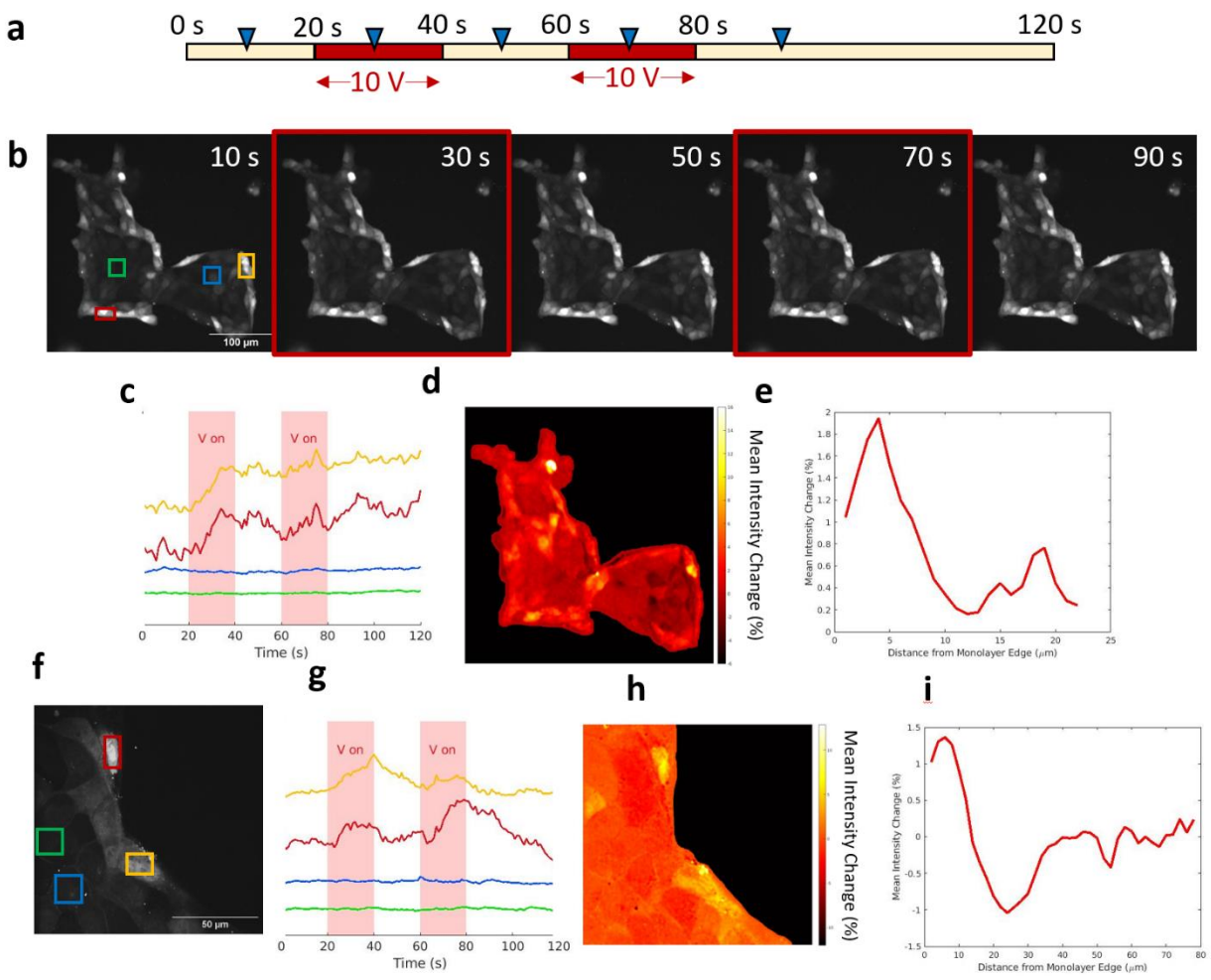

Figure 4.3: Intracellular calcium is preferentially stimulated at wound and colony edges by the application of a 10V/cm DC electric field. (a) Visual depiction of voltage application during each 120 second video. 20 seconds of 10V/cm are applied to each sample after 20 seconds and 60 seconds of imaging. Blue triangles represents the time position of the stills in Figure b. (b) Images from a video of live MDCK cells grown into a colony and dyed with 2µM fluo-8, an intracellular calcium marker. Images taken every second for 120 seconds. Stills with a red box were taken when electric field was applied. (c) Intensity of calcium marker within the cells marked by the corresponding box in Figure b. Red shading marks the periods of time when a DC voltage was applied on the tissue. (d) Map of the percent mean intensity change throughout the colony. Measurements were taken my averaging the intensity of each position for the five timepoints prior to the first application of the electric field and comparing that to the five timepoints 10 seconds later to determine the immediate calcium response to the application of the electric field. (e) The mean intensity change measured at each position in Figure d was used to find the mean intensity change of the colony compared to the position's distance from the edge of the colony. (f) A still from a video of a live MDCK wound edge dyed with fluo-8. Images taken every second for 120 seconds with two periods of 10V/cm applied to the wound edge. (g) Intensity of calcium marker within the cells marked by

Figure 4.3 Continued: the corresponding box in Figure f. Red shading marks the periods of time when a DC voltage was applied on the tissue. (h) Map of the percent mean intensity change throughout the wound edge. Measurements were taken my averaging the intensity of each position for the five timepoints prior to the first application of the electric field and comparing that to the five timepoints 10 seconds later to determine the immediate calcium response to the application of the electric field. (i) The mean intensity change measured at each position in Figure h was used to find the mean intensity change of the area near the wound edge compared to the position's distance from the edge of the wound.

further evidence that intracellular transients behave differently at colony and wound edges than they do more internally in a tissue and provides a potential role for calcium to explain why cells in a mature tissue or in larger colonies behave more collectively than cells single cells or small colonies during electrotaxis events.

4.3.4 Disruption to adhesion complexes using soft gel substrates prevents calcium enrichment at tissue edges and allows strong stimulation of calcium throughout the tissue.

Since it is the edges of colonies and wounds where we find the largest traction forces in cellular tissue (Li *et al.*, 2012; Schaumann *et al.*, 2018), we next examine the role of adhesive complexes in the organization of intracellular calcium in these samples. We do this by plating MDCK samples onto soft collagen substrates in order to disrupt the basal adhesion complexes (Collins *et al.*, 2017; Tang, 2020).

Wound edge cells plated on soft collagen do not show a higher intensity of calcium at wound edges, in fact the intensity of the calcium probe is largely consistent even far from the edge of the tissue layer (Figure 4.4 a, d). In addition, unlike samples grown on a stiffer substrate, we find transient calcium peaks present at equally strong intensities both near the wound edge and further from the wound edge (Figure 4.4 b, c). Interestingly, these spontaneous calcium events appear to be co-stimulated, meaning that we see the peaks take on similar shapes and are

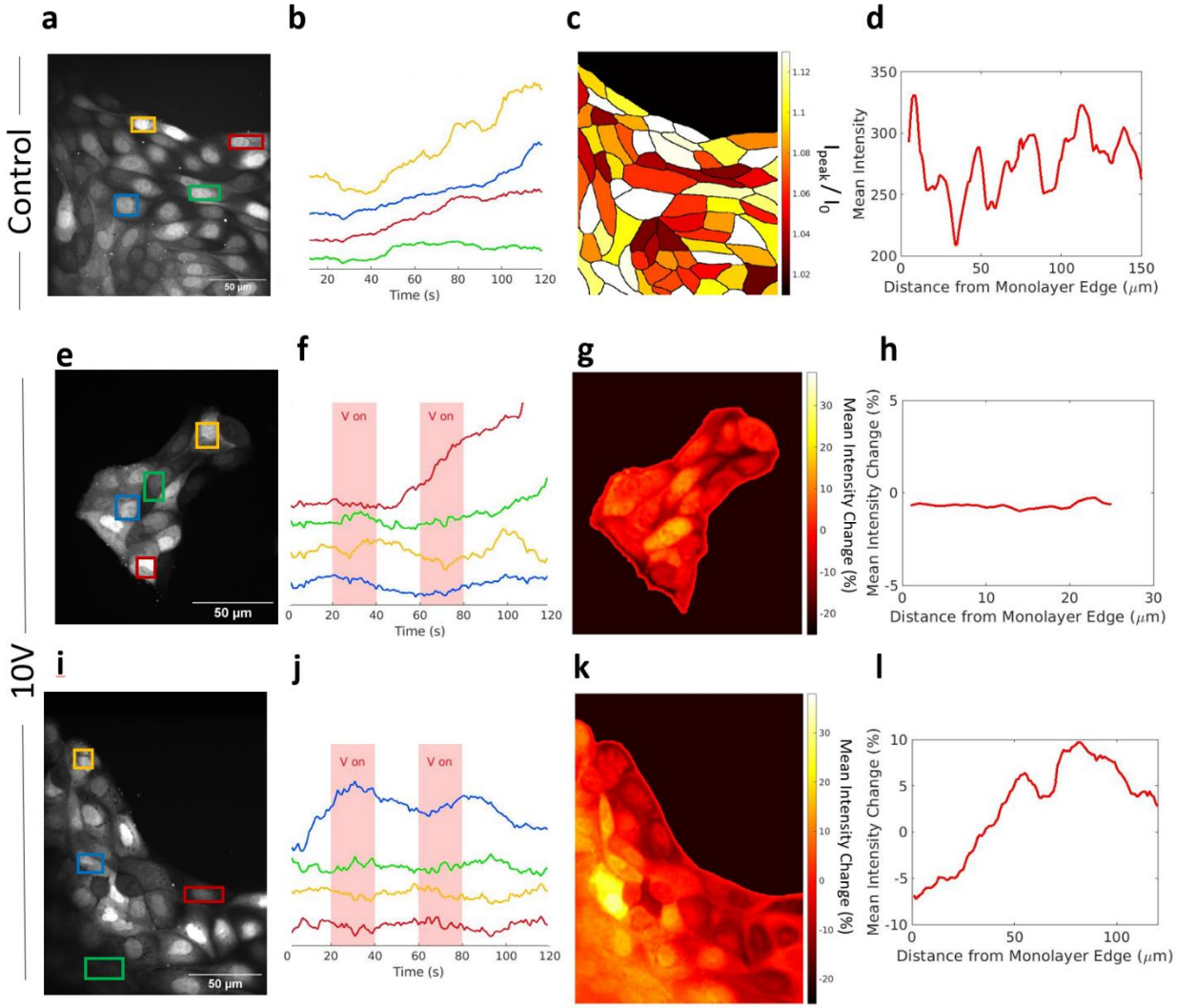

Figure 4.4: Disruption to adhesion complexes using soft gel substrates prevents calcium enrichment at tissue edges and allows strong stimulation of calcium throughout the tissue (a) A still from a video of a live MDCK wound edge grown on soft collagen and dyed with fluo-8. Images taken every second for 120 seconds. (b) Intensity of calcium marker within the cells marked by the corresponding box in Figure a. Transient calcium spikes can be observed. Photobleach corrected. (c) Segmented image of the wound edge showing the peak intensity measured throughout the video compared to the mean background intensity for each individual cell. (d) Measurement of initial wound calcium intensity compared to that position's distance from the edge of the wound. (e) A still from a video of a live MDCK wound edge grown on soft collagen and dyed with fluo-8. Images taken every second for 120 seconds with two periods of 10V/cm applied to the wound edge. (f) Intensity of calcium marker within the cells marked by the corresponding box in Figure e. Red shading marks the periods of time when a DC voltage was applied on the tissue. (g) Map of the percent mean intensity change throughout the colony. Measurements were taken by averaging the intensity of each position for the five timepoints prior to the first application of the electric field and

Figure 4.4 Continued: comparing that to the five timepoints 10 seconds later to determine the immediate calcium response to the application of the electric field. (h) The mean intensity change measured at each position in Figure g was used to find the mean intensity change of the colony compared to the position's distance from the edge of the colony. (i) A still from a video of a live MDCK wound edge dyed grown on soft collagen and dyed with fluo-8. Images taken every second for 120 seconds with two periods of 10V/cm applied to the wound edge. (j) Intensity of calcium marker within the cells marked by the corresponding box in Figure i. Red shading marks the periods of time when a DC voltage was applied on the tissue. (k) Map of the percent mean intensity change throughout the wound edge. Measurements were taken by averaging the intensity of each position for the five timepoints prior to the first application of the electric field and comparing that to the five timepoints 10 seconds later to determine the immediate calcium response to the application of the electric field. (l) The mean intensity change measured at each position in Figure k was used to find the mean intensity change of the area near the wound edge compared to the position's distance from the edge of the wound.

temporally related to each other, something that we did not observe in samples grown on more rigid substrates.

When we applied the same 10V/cm electric field onto the samples, we find that this softer substrate allows for strong calcium stimulation both at the edges of colonies and wounds and further in the center of the tissue layer (Figure 4.4 e, f, i, j). By analyzing the mean intensity change both before and after the application of the electric field, we see that once again we have lost the edge effects that were present in samples plated on rigid surfaces. There is no significant difference in calcium activation depending on distance from the edge in colonies (Figure 4.4 h) and there is an inverse effect in wound edges with the mean intensity enriched in this particular field of view 50-100 μm away from the edge of the wound (Figure 4.4 l).

Together this data indicates that disruption to basal adhesive complexes due to softer gel substrates results in the loss of the collective calcium edge dynamics which we observe in wound edges and small colonies.

4.4 Discussion

Our results indicate transient intracellular calcium's importance at wound and colony edges during electrotaxis-based cell migration. We show that calcium is highly enriched at these edges and that transient intracellular calcium spikes are consistently strongest in edge cells during stimulation by an electric field. We also find that soft substrates which disturb focal adhesive properties dispel these calcium edge effects, showing how the mechanical extracellular environment affects ion distribution in a tissue.

Why does it matter that calcium transients are found at wound and colony edges and are affected by substrate stiffness? Together, these results indicate a relationship between the traction forces also relegated to colony and wound edges, and calcium signaling stimulated by an electric field. When it comes to why colonies and wound edges migrate with more directiveness than single cells, we are able to show that the interesting dynamics in these collective systems are taking place at the tissue edges. Its these edges that are driving the collective migration and these edges that are preferentially stimulated by the electric field.

While these results illuminate a fascinating calcium-based reaction at tissue edges, the exact mechanisms which underscore the multitude of processes occurring during electrotaxis continues to be an open question, and a deeper understanding of why cells in a tissue react to electric fields with more directiveness and at lower voltages than single cells still remains to be fully explored. Here, we have examined a strong correlation between tissue and wound edges, calcium-based stimulation, and the adhesive forces which cells require for migration. This correlation is not the end of the story, but it does strongly implicate the ways in which edges of a

tissue, edges that are so rare in vivo outside of wound edges, play a strong role in our ex vivo and in vitro understanding of how cells respond to electric fields.

4.5 Methods

Cell Culture: MDCK-II cells were cultured in Dulbecco's Modified Eagle's Medium (DMEM) and supplemented with 10% fetal bovine serum (FBS) (ThermoFisher Scientific), 2mM L-glutamine (Invitrogen), and penicillin-streptomycin (Invitrogen). Cells were incubated in a humidified environment at 37C and 5% $C0_2$. Cells plated on soft gel were plated on 2μm/ml polymerized collagen.

Sample Creation: To create a mature monolayer, MDCK cells were plated densely to coat the glass bottom of a 50mm glass bottom petri dish with a 30mm glass diameter (MatTek). The cells were then incubated for 48 hours with a change of media at 24 hours. To create small colonies, MDCK cells were plated sparsely to coat the glass bottom of the same petri dish and incubated for 24 hours. To create wound edges, a square polydimethylsiloxane (PDMS) mask was used. The PDMS mask was made with a 10:1 ratio of elastomer to curing agent (Sylgard), placed in a vacuum desiccator for 30 minutes to degas, and then poured into a flat dish to a thickness of 0.5mm and cured at 50°C overnight. The PDMS was then cut into 2cm squares and a square 5mm leather punching tool (DGOL) was used to make a 5mm hole in the center of the mask. The mask was soaked in 100% acetone for 90 seconds and then rinsed and soaked in PBS overnight. The mask was then added to the bottom of the glass bottom petri dish prior to plating MDCK cells and then removed 2 hours prior to imaging, creating disturbed edges to the monolayer.

Electrotaxis: A DC voltage was applied to the sample using a variable DC power supply (Vlifree) with wires connected to silver electrodes placed in wells of PBS on either side of the sample. A 2% agarose gel poured 0.5 mm thick into a dish and left to solidify at room temperature for 30 minutes was cut to 1.5 cm wide and 6 cm long and used to connect the PBS wells to the sample. The two strips of agar gel were positioned so that they were 1 cm apart and on the bottom of the sample's glass bottomed petri dish. Tape was used to secure all wires and prevent any disturbance to the setup.

Microscopy and Live Cell Imaging: 2μM of fluo-8 (Invitrogen) was added to samples 30 minutes prior to imaging to illuminate intracellular calcium. Samples were imaged on an inverted T-E microscope (Nikon) with a confocal CSU-X spinning disk (Yokogawa Electric Corporation), a stage controller (Prior), and a CMOS camera (Zyla-Andor). Metamorph software was used to control the microscope and collect images. A stage incubator (Chamlide and Quorum Technologies) with CO-2, humidity, and temperature control was used for timelapse experiments with the lid slightly open to allow for wires to reach the sample. A 491 nm laser (Hubner Photonics Inc, Cobolt Calypso) was used to illuminate the fluo-8 dye. Images were acquired using a 40x Plan Apo NA water immersion objective with a NA of 1.15 and a WD of 0.59-0.61 (Nikon).

Quantification and Statistical Analysis Image analysis and quantification was performed in Fiji and MATLAB. Cell segmentation was performed using Fiji image software. Photobleach correction was performed on all intensity measurements using custom MATLAB code. I_{peak}/I_0 measurements were taken by measuring the ratio of the maximum value for each cells mean intensity trace and the baseline value for each cell's mean intensity trace. Mean intensity change measurements were taken by averaging the five timepoints prior to the first application of the

electric field, and the five timepoints 10 seconds later after the application of the electric field. A 2-pixel gaussian blur filter was applied to smooth the image results.

Chapter 5: Force-dependent intercellular adhesion strengthening underlies asymmetric adherens junction contraction

5.1 Preface and Abstract

5.1.1 Preface

The following chapter has been adapted from (Cavanaugh *et al.*, 2022) and is originally published in Current Biology volume 32, issue 9. This project grew out of experimental results performed by Kate Cavanaugh, who is the first author on the paper in which these results are published. My contribution to this work has been extensive data analysis, including novel image analysis techniques which we used to measure junction asymmetry and extensive statistical work on the resulting data. In particular, I developed and analyzed the motility, relative displacement, center of contraction of the activated cell vertices, and implementation of the Hartigan dip test of unimodality (Hartigan and Hartigan, 1985) to describe junctional asymmetry. This work is described in Figure 5.1 E,F,J-L, Figure 5.2 A-C,E,F,H,I, Figure 5.3 I,J, and Figure 5.4 B-F.

5.1.2 Abstract

Tissue morphogenesis arises from the culmination of changes in cell-cell junction length. Mechanochemical signaling in the form of RhoA underlies these ratcheted contractions, which occur asymmetrically. The underlying mechanisms of asymmetry remain unknown. We use optogenetically controlled RhoA in model epithelia together with biophysical modeling to uncover the mechanism lending to asymmetric vertex motion. Using optogenetic and pharmacological approaches, we find that both local and global RhoA activation can drive

asymmetric junction contraction in the absence of tissue-scale patterning. We find that standard vertex models with homogeneous junction properties are insufficient to recapitulate the observed junction dynamics. Furthermore, these experiments reveal a local coupling of RhoA activation with E-cadherin accumulation. This motivates a coupling of RhoA-mediated increases in tension and E-cadherin-mediated adhesion strengthening. We then demonstrate that incorporating this force-sensitive adhesion strengthening into a continuum model is successful in capturing the observed junction dynamics. Thus, we find that a force-dependent intercellular ‘‘clutch’’ at tricellular vertices stabilizes vertex motion under increasing tension and is sufficient to generate asymmetries in junction contraction.

5.2 Introduction

Morphogenesis relies on the tight spatiotemporal control of cell-cell junction lengths (Lecuit *et al.*, 2011). Contractile forces, acting at adherens junctions, alter junction lengths as a cyclic ratchet (Solon *et al.*, 2009; Rauzi *et al.*, 2010; Fernandez-Gonzalez and Zallen, 2011; Mason *et al.*, 2013). Preceding these ratcheted contractions are pulses of active RhoA (Rauzi *et al.*, 2010; Munjal *et al.*, 2015; Kerridge *et al.*, 2016), the strength and temporal pattern of which control junction tension to confer junction length (Staddon *et al.*, 2019; Cavanaugh *et al.*, 2020b). Through effector activation, contractile actomyosin arrays assemble rapidly in response to intracellular biochemical signals and/or physical cues from neighboring cells (García-Mata and Burridge, 2007). As such, RhoA GTPase cycling is thought to give rise to spatiotemporal changes in junction length which, in turn, drive tissue morphogenesis (Mason *et al.*, 2016). While the molecular components of these mechanochemical systems are well characterized, the

mechanisms by which RhoA regulates junctional tension and adhesion to control cell shape remains largely unknown.

A recent study has revealed the asymmetric nature of junction contraction that occurs during germband extension (Vanderleest *et al.*, 2018). Here, one tricellular vertex is highly mobile and contracts towards a more immobile, stationary vertex. The net result of this asymmetric vertex motion is coordinated asymmetry in junction deformation whose collective contractions facilitate global tissue rearrangements (Vanderleest *et al.*, 2018; Huebner *et al.*, 2021). A possible mechanism underlying this innate vertex asymmetry describes heterogeneous force production along the junction proper. Non-uniform force production may cause very local actomyosin flows to specific regions of the junction for qualitatively different junctional responses. Bicellular edges, for example, act as independent contractile units apart from tricellular vertices (Choi *et al.*, 2016; Vanderleest *et al.*, 2018). Medioapical actomyosin flows to the bicellular interfaces can also generate contractile forces sufficient to deform junctions (Rauzi *et al.*, 2010; Munjal *et al.*, 2015). Flows to the tricellular vertices may restrict these contractions, thus stabilizing the junctional ratchet (Vanderleest *et al.*, 2018). The coordination between these spatially distinct actomyosin flows may yield asymmetric junction shortening (Vanderleest *et al.*, 2018). Thus, sub-cellular mechanics that underlies this asymmetry remain unclear.

Cells sense and respond to mechanical cues through force-sensitive feedbacks within the cytoskeleton. Apical E-cadherin-based adhesions mediate intercellular cell-cell adhesion. However, E-cadherin should be envisaged not as a static participant of cellular adherence but rather as a dynamic sensor of force that dictates cellular behavior. For example, force stimulates the RhoA pathway and myosin light chain phosphorylation, resulting in an overall increase in actin polymerization at adherens junctions (Acharya *et al.*, 2017). Additionally, force-sensitive

processes within adherens junctions allows adhesive components to strengthen under force (Manibog *et al.*, 2014). Here, cadherin catch bonds are strengthened when adhesion complexes experience tensile force (Buckley *et al.*, 2014). Together these mechanisms cause clustering of E-cadherin molecules and actin to trigger adhesion complex growth (Hong *et al.*, 2013). In this way, these proteins subsequently generate a reinforcement response to anchor junctions against applied force (Pannekoek *et al.*, 2019). However, it is still unclear if and how cells' force-sensitive coupling of actomyosin and adhesion complexes modulate junction length to coordinate morphogenetic movements at the cellular scale.

Here, we investigated the origins of asymmetric junction contraction by using optogenetic and pharmacologic modulation of RhoA activity. This system allowed for sub-cellular control of RhoA stimulation to investigate the origins of asymmetric contraction. We then used computational modeling to offer predictions on the mechanistic origin of this asymmetric contraction. Our experimental data indicated that differential regulation of vertex tension, as predicted by canonical models of epithelial tissues, was insufficient to account for such asymmetry. We then explored whether local coupling between RhoA-mediated contraction and vertex friction could account for the experimental results. We found that force-dependent adhesion strengthening at tricellular vertices act to locally reinforce the vertex to restrict its movement. Thus, coupling between RhoA-mediated tension and adherens junction strengthening was sufficient to recapitulate experimental data. Modulating E-cadherin friction with pharmacological perturbations, we induced symmetry back into the system or abolished junction contraction entirely. Our modeling and experimental data therefore point to a unified model of asymmetry induced by both friction and local contraction that is mediated by a RhoA-dependent asymmetric recruitment of E-cadherin at tricellular vertices.

5.3 Results

5.3.1 RhoA stimulates asymmetric junction contraction in a model epithelium

To examine how RhoA controls junction contractions, we formed a model tissue by plating a colorectal adenocarcinoma (Caco-2) cell line at full confluency on collagen gels and CRISPR tagged for E-cadherin to facilitate the monitoring of junctional movements (Figure 5.1a) (Liang *et al.*, 2017). We then measured junction length by finding the interfacial distance from one tricellular vertex to the other tricellular vertex. In control conditions, there were negligible changes in junction length over the course of a two-hour period (Figure 5.1b). Here, the junction length was stable and only fluctuated about 1% over the two-hour period (Figure 5.1b).

We then treated cells with a cell permeable, pharmacological RhoA Activator, CN03, to globally and acutely increase RhoA activity across the entire tissue. We began imaging upon the addition of CN03, at time (t)=0 min, and examined junction length changes resulting from RhoA increases until (t)=125 min. About 30% of the junctions contracted, resulting in their shortening to about 80% of the initial length (Figure 5.1c). We manually tracked each vertex and measured its displacement in space over time (Figure 5.1d). In control conditions, we found that there was little to no vertex movement (Figure 5.1b, 5.1e). In contrast, in CN03 containing media one vertex moved significantly more than the other vertex (Figure 5.1c, 5.1f). This asymmetric contraction is reminiscent of observations in developmental systems (Vanderleest *et al.*, 2018; Huebner *et al.*, 2021).

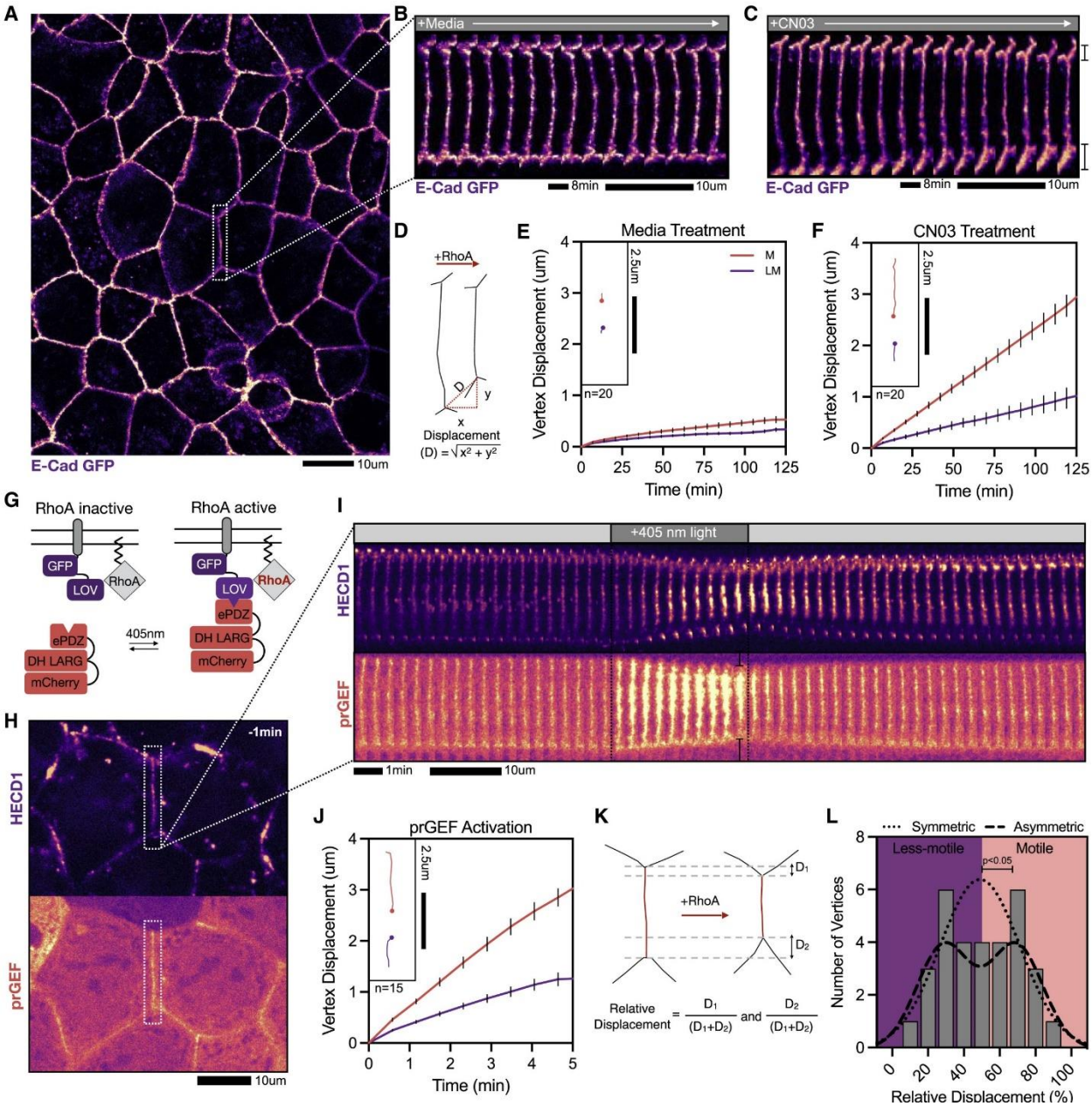

Figure 5.1: RhoA activation drives asymmetric vertex motion in model tissue (A) Representative image of a model epithelial tissue formed from confluent MDCK cells expressing E-Cadherin GFP. (B) Zoomed in images of WT junction over the course of two hours showing no junction length changes with the addition of media. (C) Representative images of timelapse video over the course of two hours showing asymmetric junction shortening with the addition of the CN03 compound. (D) Schematic of junction shortening and displacement measurement analysis. (E) Vertex displacement analysis for junctions in WT (Media Treatment) conditions showing little-to-no vertex motion. Inlay shows particle tracks for a representative vertex pair in WT conditions. (F) Vertex displacement analysis for junctions in CN03 treatment showing asymmetry in vertex displacements. Inlay shows trajectories for a representative vertex pair in CN03 treatment (G) Schematic of the TULIP

Figure 5.1 Continued: optogenetic system to drive local RhoA activation. (H) Zoomed out image of a targeted junction at -1min before optogenetic activation. Top image shows HECD1 junction labeling of E-cadherin and bottom image shows prGEF localization. (I) Timelapse of the junction in H undergoing a 5-min optogenetic activation showing asymmetric junction contraction within the activation period and junction relaxation post-activation. (J) Vertex displacement analysis for the junction within the 5-min optogenetic activation period. Displacement analysis shows asymmetric vertex displacement of the optogenetic Rho activation. Inlay shows particle tracks during the 5-min optogenetic activation period for a representative vertex pair. (K) Schematic documenting the percent movement analysis. (L) A histogram of the percent motions of all vertices in response to optogenetic stimulation shows two peaks at 30% and 70%. A Hartigan's dip test ($p=0.049$) shows that the movement of the vertices is bimodal.

To explore the mechanism of asymmetric contraction, we turned to an optogenetic approach. The logic behind this experiment was to have isolated junctions acutely experience heightened and targeted RhoA activation. For spatial and temporal control over RhoA activity, we used a Caco-2 cell line expressing the TULIP optogenetic two-component system (Strickland *et al.*, 2012; Wagner and Glotzer, 2016; Oakes *et al.*, 2017; Staddon *et al.*, 2019; Cavanaugh *et al.*, 2020b). TULIP's two components include the 1) membrane-tethered photosensitive LOVpep anchor protein and the 2) prGEF complex that houses the photorecruitable PDZ domain attached to the catalytic DH domain of the RhoA-specific GEF, LARG. Blue light (405nm) activation causes a conformational change in the LOVpep domain to expose a docking site for the engineered PDZ domain within the prGEF complex. This blue light activation increases the binding affinity between the two components, thereby recruiting the prGEF to the membrane where it drives local RhoA activation (Figure 5.1g) (Wagner and Glotzer, 2016; Oakes *et al.*, 2017; Staddon *et al.*, 2019; Cavanaugh *et al.*, 2020b). This system has high temporal resolution, as prGEF recruitment and dissociation occurs on the order of 30-60 seconds. prGEF recruitment was tightly confined to the targeted cell-cell junction, consistent with previously published work

(Figure 5.1i) (Cavanaugh *et al.*, 2020b). This system is advantageous, because it restricts junctional contraction to the optogenetically activated junction, so that the frame of reference for vertex motion is the surrounding junctions and tissue. Overall, this system gave tight spatiotemporal control over the prGEF and thus RhoA for which to study how junctions contract upon increased RhoA activity.

To visualize the distortion of the bicellular junction during asymmetric contraction, we labeled E-Cadherin using an antibody labeling technique targeting its extracellular domain. We bathed the cells for at least an hour in E-cadherin primary antibody, HECD1, and its corresponding fluorescently labeled secondary antibody. Upon washing out the antibody, we found that this labeling produced a punctate pattern of E-cadherin that delineated the cell-cell junctions and vertices (Figure 5.1h). HECD1 targets the EC2 domain region of the E-cadherin ectodomain, rather than the EC1 domain which mediates trans-binding. In this way, cellular cohesion and intercellular E-cadherin binding via EC1 domains was preserved. Indeed, we found that under the conditions of our experiments, HECD1 did not affect junction contraction dynamics (Figure 51i) (Cavanaugh *et al.*, 2020b). These light-stimulated contraction was surprisingly consistent across multiple junctions with different initial lengths and geometries.

We found that optogenetic recruitment of prGEF along the entire bicellular junction induced asymmetric contraction (Figure 5.1 i,j). To quantify the asymmetry, we measured Relative Displacement of each vertex in a vertex pair, as defined by the distance moved of one vertex (e.g. D1) over the total distance moved by both vertices (D1+D2), to yield D1/(D1+D2) and D2/(D1+D2) (Figure 5.1k). We then plotted the probability density of the relative movement. This revealed an asymmetry in the histogram with peaks around 30% and 70%, further indicating an inherent asymmetry in the distribution of vertex motion (Figure 5.1l). This

result was starkly contrasted against a symmetric contraction, where a single peak centered around 50% would be expected.

5.3.2 Asymmetric contraction can be driven by heterogeneity in active RhoA

Junctions could either contract uniformly along their length or the extent of contraction could vary as a function of position. To explore these possibilities, we used the variable intensity of HECD1 labeling to examine local variations in deformations along the junction. A line-scan along the junction, taken over time, created a kymograph for which to analyze fiduciary flows before, during, and after light-stimulated junction contraction (Figure 5.2a).

Using these kymographs, we then measured the displacement of different regions along the junction over time (Figure 5.2a). We identified the location of zero displacement to identify the contraction center. To compare junctions of varied lengths, we normalized both displacement and position along the junction by the junction length. For consistency, we identified the less mobile vertex position as “0” and the more mobile vertex position as “1”. For a symmetric contraction, we would expect to see the center of contraction at the midpoint of the junction, or 0.5, and a displacement proportional to distance from the contraction center. Instead, we found that the displacement is nonlinear, suggesting that contraction is heterogenous along the bicellular junction (Figure 5.2b). Further, we found the contraction center to be skewed towards the less-motile vertex (Figure 5.2 a,c). Analyzing multiple kymographs revealed that the mean center of junction contraction was consistently closer to the less-motile vertex with a mean of 0.32 (Figure 5.2c). By contrast, values of normalized center of contraction over 0.5 would be achieved in scenarios in which the center of contraction is proximal to the motile vertex.

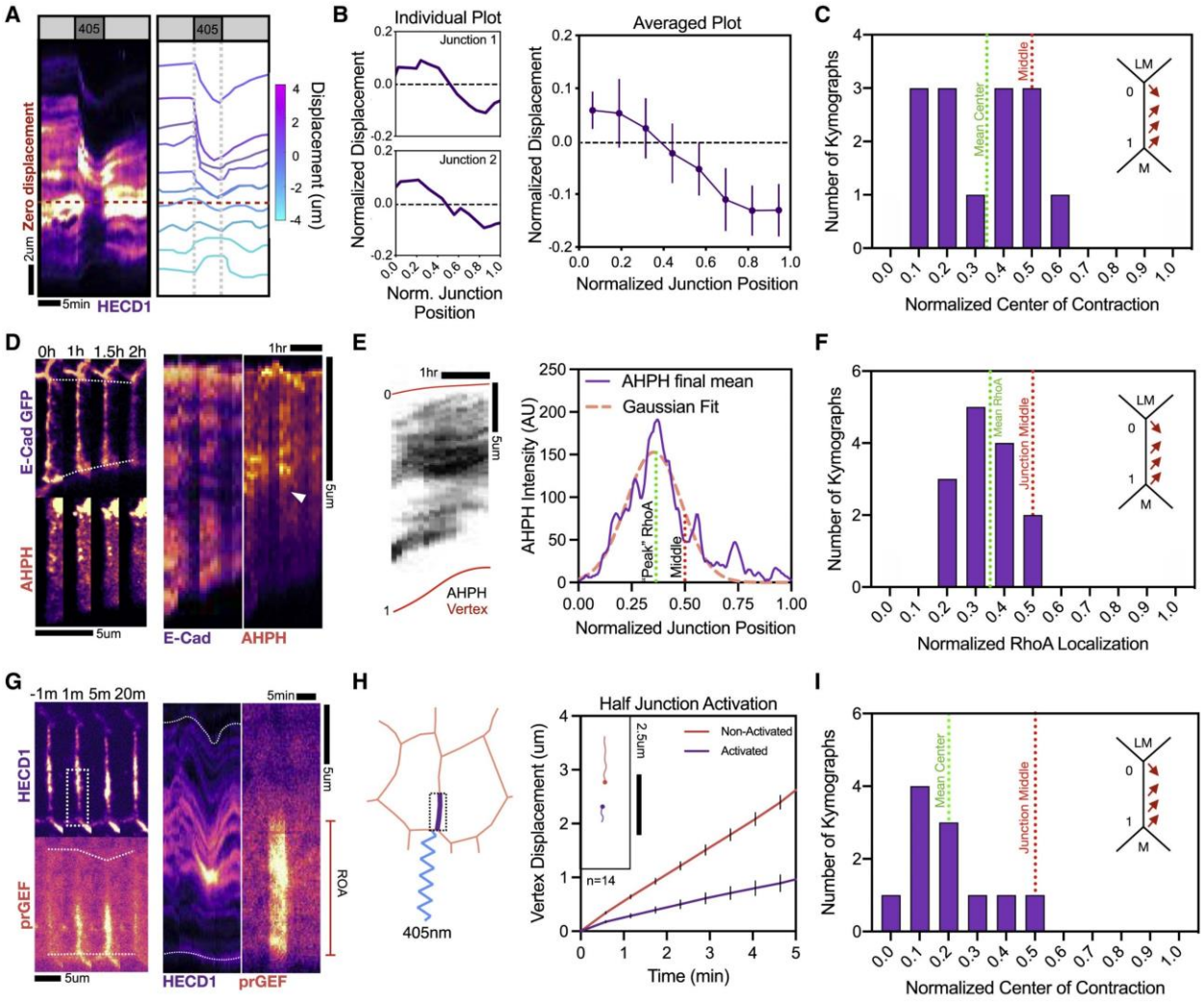

Figure 5.2: Asymmetric distribution of active RhoA drives contraction asymmetry (A) (Left) Representative kymograph of an optogenetically activated junction labeled with HECD1 showing asymmetry junction contraction and relaxation. (Right) Fiducial marks seen in the kymograph to the left are color coded according to the amount of displacement within the optogenetic activation period. The location of zero displacement of the fiducial marks is marked with a dashed red line. (B) (Left) Analysis of the displacement of each fiducial mark's flows as a function of the distance from the contraction center for two individual junctions showing nonlinear displacement from one end of the junction to the other, indicating a nonuniform contraction of each junction. (Right) Averaged plot showing the nonlinearity of fiducial displacement as a function of the normalized junction position. Error bars show standard deviation. (C) Inlay shows diagram of the Less-motile (LM) vertex being labeled as 0 and the Motile (M) vertex being labeled as 1. Red arrows represent the extent of the vertex motion along the junction during contraction. Analysis of the localization of zero displacement (as seen in A) of the fiduciary marks indicates the center of the junction as being skewed towards the less-motile vertex. (D) (Left) Representative image E-cadherin-GFP and RhoA biosensor, AHPH in a junction subjected to CN03 treatment. Junction shows

Figure 5.2 Continued: asymmetric contraction with a RhoA flare along the junction. (Right) Kymographs show asymmetric junction contraction and a RhoA flare that is biased towards the less-motile vertex. (E) Analysis of the junctional AHPH intensity plots averaged over the last 5 frames of the kymograph (left) fitted to a Gaussian curve. Green dotted line indicates the peak of the Gaussian fit, indicating the centralized location of the RhoA biosensor. (F) Pooled analysis of the peak of the RhoA biosensor, as calculated in E, showing mean junctional RhoA localization as being skewed towards the less-motile vertex. (G) Representative image and kymograph of a junction undergoing half-junction activation at the bottom junctional region. (H) Vertex displacement analysis of bottom-junction activation showing contractile asymmetry between two vertices. Inlay shows individual vertex tracks for two vertices of the same junction. (I) Normalized center of contraction analysis for bottom-junction activation showing the center of contraction is skewed towards the region of activation.

It is plausible that that RhoA activity is not uniform along the junctions, giving rise to heterogeneous stress along the junction. To explore this, we used the RhoA biosensor (AHPH) containing the GTP-RhoA binding C-terminal portion of Anillin (Piekny and Glotzer, 2008; Budnar *et al.*, 2019). We transfected the E-cadherin expressing cells with the AHPH and then visualized RhoA activity during a CN03 wash-in experiment. We observed discrete sub-junctional region of heightened active RhoA, which we termed flares (Figure 5.2 d,e). We measured the intensity of active RhoA along the junction and found that the peak, the central flare location, was skewed towards the less-motile vertex (Figure 5.2 d,e). Fitting a Gaussian curve to this data, we labeled the peak of this Gaussian as the location of the "peak" RhoA region (Figure 5.2e). By analyzing fourteen kymographs, we found that the mean RhoA flare position was skewed towards the less-motile vertex, with an average position of 0.35 (Figure 5.2f).

The above data indicated that the location of RhoA flares were critical in determining asymmetric contraction, with reduced mobility of the vertex proximal to active RhoA. To test

this hypothesis, we exploited the optogenetic approach to systematically activate only a portion of the junction. When the lower half of the junction was activated, the junction contracted to about 85% of its original length, similar to the extent for full junction activation. The vertex proximal to the region of activation (ROA) was significantly less mobile than the distal vertex (Figure 5.2 g-h). Kymograph analysis in the HECD1 channel revealed that the center of contraction for the half junction activation was at the relative position of 0.2 (Figure 5.2i). Altogether these data indicate that asymmetry in active RhoA dictates the bias in vertex motion.

5.3.3 Mechanosensitive E-cadherin induces vertex friction at less-motile vertices

RhoA acts at cell-cell interfaces to regulate cell morphology through its effect on actomyosin tension and adhesion strength (Levayer *et al.*, 2011; Cavanaugh *et al.*, 2020b). To explore the possibility that changes in adhesion strength underlie vertex immobility, we analyzed E-cadherin localization, as visualized by HECD1 fluorescence, at tricellular vertices during whole junction optogenetic stimulation. We observed HECD1 fluorescence in punctate along the junction and at both vertices. We monitored the HECD1 fluorescence at both vertices during an activation experiment. At the more motile (M) vertex, we found that the HECD1 intensity did not vary significantly during the experiment (Figure 5.3a, red arrow). By contrast, at the less motile (LM) vertex, we found there was a marked increase of HECD1 immediately after activation which diminished after exogenous stimulation was removed (Figure 5.3 a,b). This trend was consistent across numerous junctions and paired vertices (Figure 5.3c). To further explore the contribution of E-cadherin levels to vertex asymmetry, we analyzed the relative HECD1 fluorescence intensities between the motile and less-motile vertices. We found that before optogenetic activation, at T0, we found no significant difference in normalized vertex

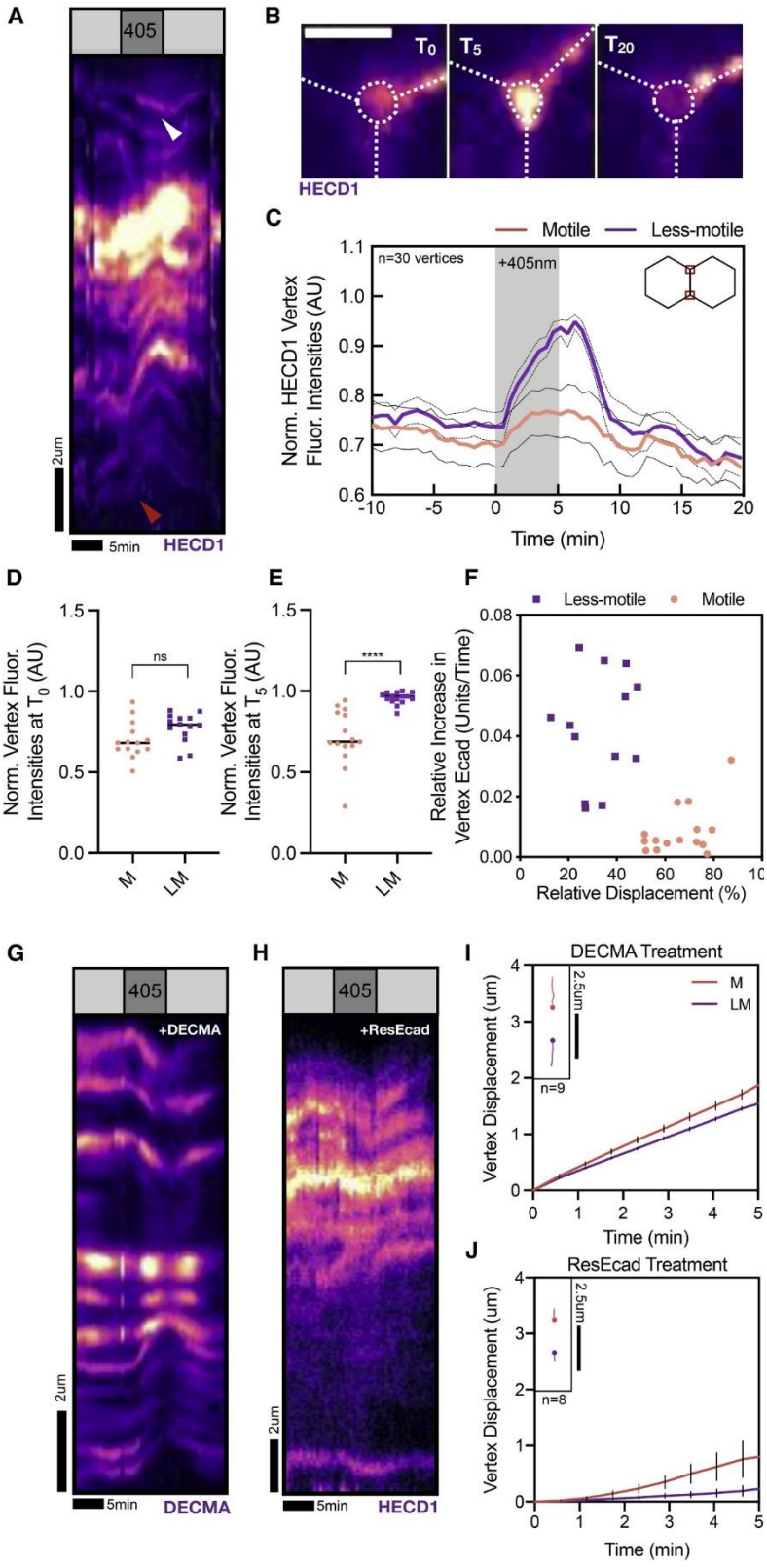

Figure 5.3: E-Cadherin accumulates at less-motile vertex and perturbations to E-cad alter contraction dynamics (A) Representative kymograph of optogenetic activation showing increases in E-cadherin pooling at the less-motile vertex (white arrow) versus the motile vertex (red arrow). (B) Representative image of a less-motile tricellular contact showing E-cadherin pooling at the vertex after 5 minutes of optogenetic activation. Scale bar is 2.5µm. (C) Quantification of vertex fluorescence intensities of motile and less-motile vertices. Less-motile vertices show increases in E-cadherin pooling and subsequent vertex fluorescence compared to motile vertices. (D) Quantification of the normalized HECD1 fluorescence vertex intensities before optogenetic activation at T_0 for motile and less-motile vertex shows no significant difference. (E) Quantification of the normalized HECD1 fluorescence vertex intensities after optogenetic activation at T_5 for motile and less-motile vertex shows a significant, heightened level of E-cadherin at less-motile vertices. ****=p<0.0001 as calculated by the Student's t-Test. (F) Relative increases of the Vertex HECD1 (E-Cad) plotted against the relative displacement of that vertex shows highly motile vertices with less HECD1 changes and

Figure 5.3 Continued: less-motile vertices showing more HECD1 level changes. (G) Representative kymograph of junction treated with the E-cadherin blocking antibody, DECMA. (H) Representative kymograph of cells treated with ResEcad. (I) Vertex displacement analysis of DECMA-treated junctions showing symmetric contraction. Inlay shows particle tracks of a representative vertex pair during optogenetic activation. (J) Vertex displacement analysis of ResEcad-treated junctions showing a severe reduction in the contraction. Inlay shows particle tracks of a representative vertex pair during optogenetic activation.

HECD1 fluorescence intensities (Figure 5.3d). After five minutes of optogenetic activation, at T5, we found a significant increase in HECD1 fluorescence intensities at the less-motile vertex compared to the less-motile vertex (Figure 5.3e). We then plotted the relative increase in vertex HECD1 as a function of the relative displacement of each vertex and saw a clear trend suggesting that the higher the relative increase in E-Cadherin, the less the vertex would move in space, thus promoting vertex asymmetry (Figure 5.3f). Together these data indicate that changes in tricellular junction adhesion strength may contribute to the observed asymmetry.

To explore whether E-cadherin-mediated adhesion acts to impede contraction via its contribution as a source of frictional drag, we next sought to modulate E-cadherin interactions. First, we used a function blocking antibody, DECMA, and its conjugated secondary antibody to visualize junctional dynamics. DECMA binds specifically to EC1 domains on E-cadherin, abolishing any trans interactions between E-cadherin molecules, thereby reducing E-cadherin binding. Upon addition of DECMA, we found a similar labeling pattern of E-cadherin that coated the junction (Figure 5.3g). Optogenetic activation induced similar junctional contractions compared to WT conditions, but the contraction was more symmetric (Figure 5.3 g-i) To increase junctional friction, we next sought to increase the levels of E-cadherin through the cell-permeable, pharmacological isoxazolocarboxamide compound, ResEcad (Stoops *et al.*, 2011).

This compound has been shown to induce a dose-dependent increase in E-cadherin levels in adenocarcinoma cells, thereby modulating junctional friction levels. We found ResEcad treatment severely suppressed optogenetically induced junction contraction (Figure 5.3 h,j). These data indicate that modulating E-Cadherin levels and interactions, inducing either low or high adhesion strength, can dramatically influence both the magnitude and asymmetric nature of vertex motions.

5.3.4 Local RhoA drives E-cadherin Accumulation

The above data hint at active RhoA driving E-cadherin recruitment to modify adhesion strength along the bicellular or tricellular junction; an idea that has been explored recently (Iyer *et al.,* 2019; Noordstra *et al.,* 2021). To explore this, we used our optogenetic approach to selectively recruit prGEF to the tricellular junction or a small portion of the bicellular junction. Interestingly, tricellular vertex prGEF recruitment was insufficient to induce junction contraction, with the vertices exhibiting little to no vertex displacement compared to WT full-length activation (Figure 5.4 a,b). However, tricellular vertex activation did induce a 30% increase in E-cadherin intensity (Figure 5.4 a,c). These data indicated that RhoA activation locally recruits E-cadherin, even in the absence of visible junction contraction.

We next activated a small portion of the bicellular junction (Figure 5.4d). Activation at the center third of the junction created a contraction whose extent was similar to WT full-length activation. As the center was being activated, there was a noticeable concentration of E-cadherin puncta to the region of activation (Figure 5.4d). Displacement analysis for the center activation indicated that the contraction was more symmetric, with both vertices moving considerably and relatively evenly upon prGEF recruitment (Figure 5.4e). Moreover, analysis of the HECD1

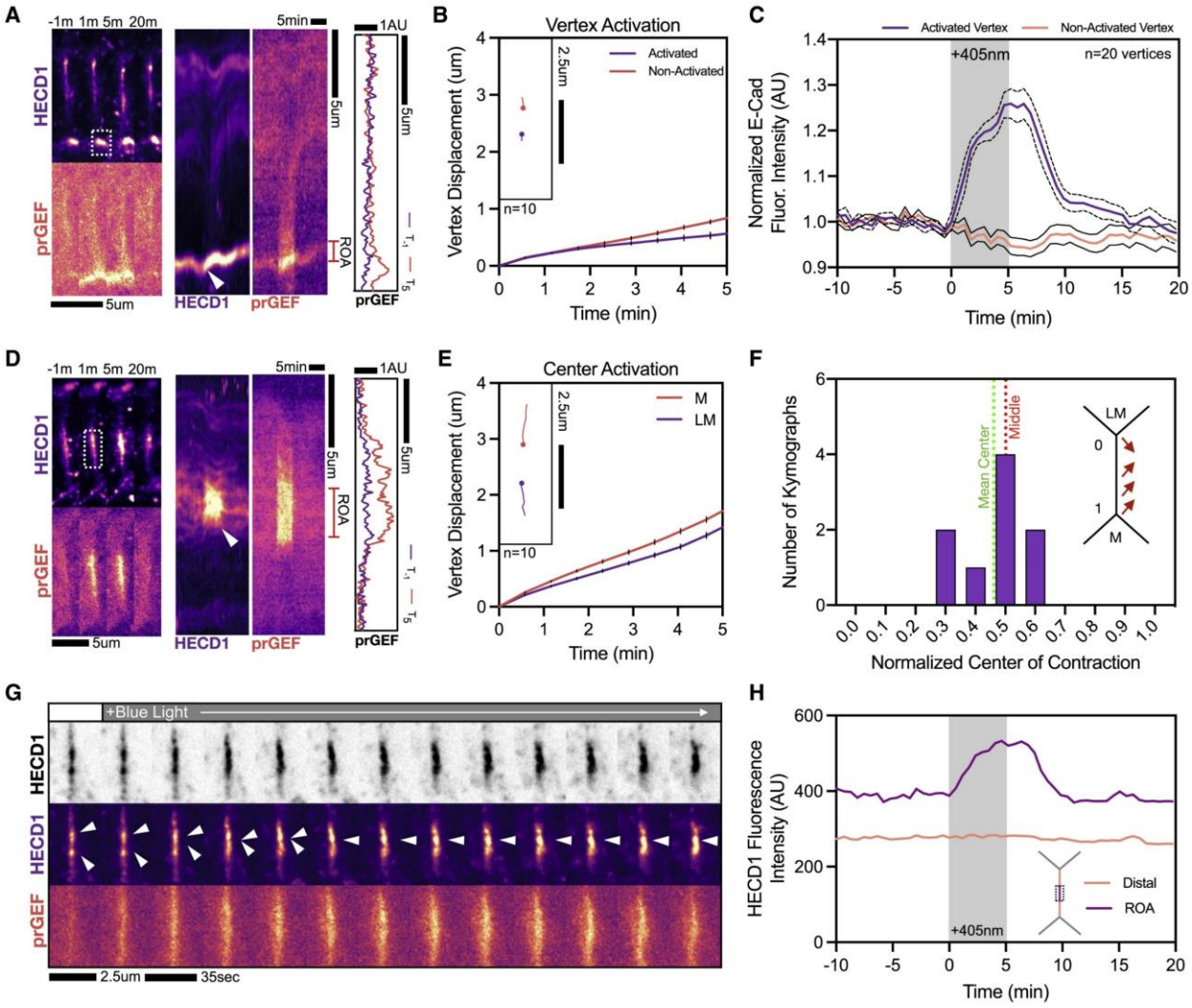

Figure 5.4: RhoA activation drives local E-cadherin accumulation (A) Representative image and kymograph of a junction undergoing only vertex activation at the tricellular contact. (B) Vertex displacement analysis of vertex activation showing little-to-no vertex motion within the optogenetic activation period. Inlay shows individual vertex tracks for two vertices of the same junction. (C) Normalized HECD1 (E-cadherin) fluorescence intensities for vertices during vertex activation between the activated and non-activated vertices. Activated vertices show increases in E-cadherin fluorescence intensities. (D) Representative image and kymograph of a junction undergoing center-junction activation. (E) Vertex displacement analysis of center-junction activation showing contractile symmetry is restored. Inlay shows individual vertex tracks for two vertices of the same junction. (F) Normalized center of contraction analysis for center-junction activation showing the center of contraction is in the middle of the junction, consistent with where RhoA is activated. (G) Representative images of HECD1 and prGEF before and during optogenetic activation, showing displacement E-cadherin puncta upon activation (white arrows). (H) Quantification of average fluorescence intensities of HECD1 of data in Fig. 5.4G both within the region of activation (ROA) and the two flanking regions proximal to the ROA.

fiducial marks revealed that the center of contraction was symmetric, with a mean center of contraction of 0.47 (Figure 5.4h).

We observed E-cadherin accumulation with this stimulation geometry, which also provided a means to explore its possible mechanisms. E-cadherin punctae coalescence upon junctional prGEF recruitment within the activation period (Figure 5.4g). Here, prGEF recruitment preceded this concentration of E-cadherin, as smaller punctae of E-cadherin coalesced to a concentrated point upon blue light activation (Figure 5.4g, white arrows). We then measured the fluorescence intensities of the HECD1 at the region of activation (ROA) and the non-activated flanking regions (Figure 5.4h). This analysis revealed heightened accumulation of HECD1 at the region of activation compared to the distal portion, where the overall intensity change was negligible. There was no depletion of HECD1 fluorescence intensities within the flanking regions, indicating minimal lateral motion of punctae from the flanking to activated region. Rather, these data led us to suspect that E-cadherin accumulation occurs from diffuse membrane-associated E-cadherin, including from those regions outside the focal plane and/or along the basolateral interface. Further, the coalescences suggests that the punctae are relatively stable and accumulate intensity from diffusing E-cadherin. This is not dissimilar to the increase in intensity of focal adhesion proteins within plaques during their assembly (Gardel *et al.*, 2010).

Together, these data hint that junctional RhoA activity serves both to generate stresses required for contraction as well as modify cell-cell adhesion through E-cadherin recruitment. Thus, we surmise their coordination drives the nature of junction contraction, which we explore with mathematical modeling.

5.3.5 Mechanical model of asymmetric junction contraction

To quantitatively explain the biomechanical origins of the observed asymmetric contraction, we developed a continuum mechanical model for the junction dynamics arising from the balance of tensional forces of the primary junction with the two neighboring shoulder junctions, and a frictional drag acting at the vertices to resist their motion (Fig. 5.5 a,b). We modeled the junction as a linear elastic continuum with compressional elastic modulus E, tension Λ, and dissipating stresses with a friction coefficient μ. The shoulder junctions provide an elastic spring-like resistance to motion with stiffness k. We surmise that the regions flanking those of heightened tension are the primary source of friction and dominated by the shoulder junctions and/or the bicellular interface. Building upon molecular clutch models regulating cell adhesion (Aratyn-Schaus and Gardel, 2010; Noordstra *et al.*, 2021), we surmise that friction arises from the relative motion between the E-cadherin-bound membrane and the actin cortex, mediated by turnover of linkers such as the ERM proteins, α- and β-catenins as well as from differential motion of the contracting junction with the flanking shoulder junctions (Figure 5.5a).

Our continuum modeling approach for the intercellular junction stood in contrast to existing vertex models of epithelial tissues (Farhadifar *et al.*, 2007; Fletcher *et al.*, 2014; Alt *et al.*, 2017), where the epithelia are modelled as networks of edges under uniform and constant tension (Noll *et al.*, 2020) , with the vertex positions determined by force balance from the neighboring junctions. By modeling the junction as an elastic continuum, we allowed for the junction tension and friction forces to vary along the length of the junction, such that the displacement along the junction would be tracked during a contraction event (Figure 5.5c). Mechanical force balance at a point along the junction was written as

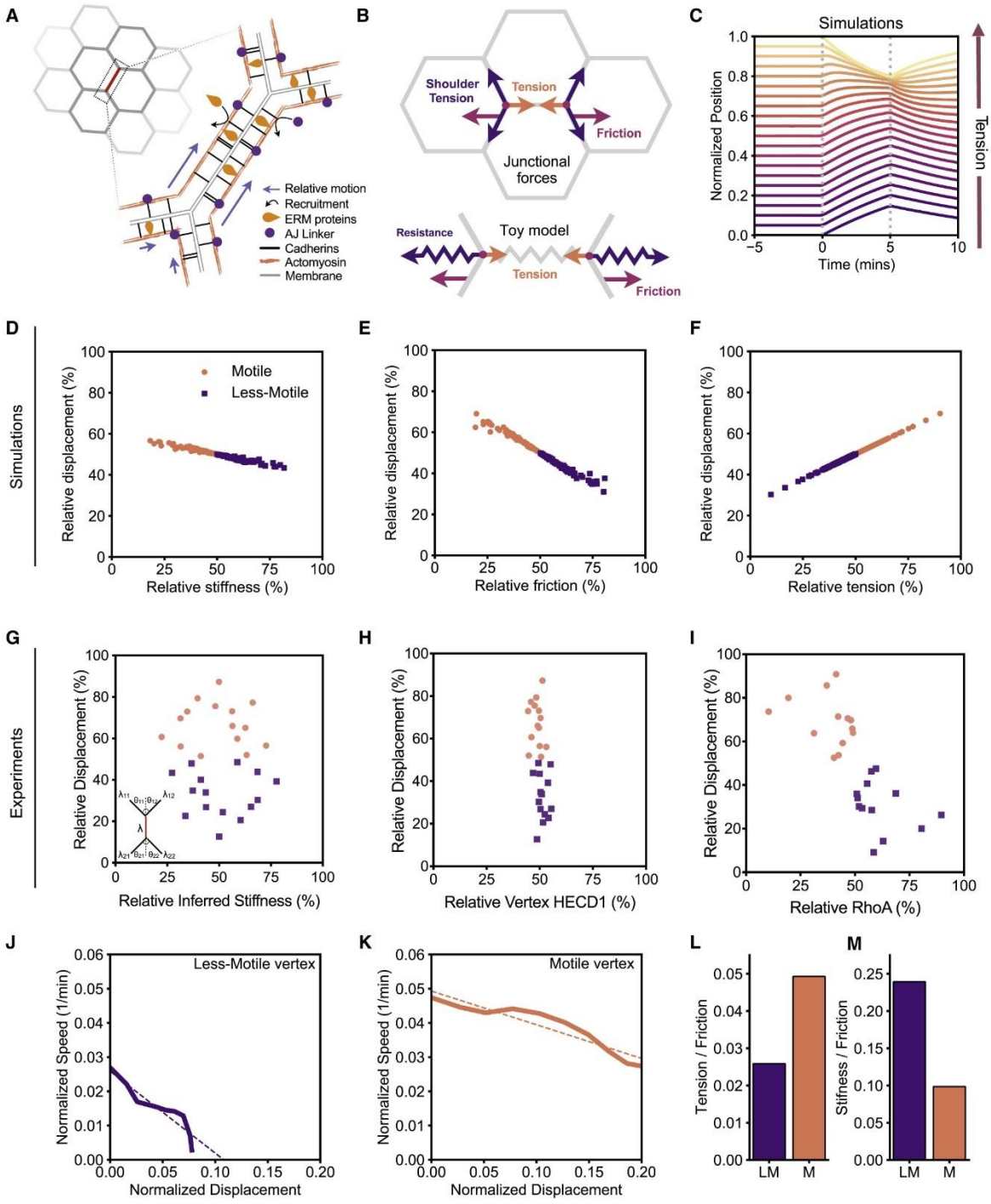

Figure 5.5: Mechanical forces regulating vertex motion asymmetry (A) Schematic showing a single junction's architecture at the bicellular interface, with speculation on molecular scale interactions built from existing literature. (B) Toy model schematic, illustrating the forces that control junction contraction dynamics. Shoulder junctions are modeled through a spring-like tensions and friction that resist the extent and rate of deformation. Junction is modeled as an elastic continuum, where tension and friction may vary along the junction, and at the vertices. (C) Kymograph of simulation junction during

Figure 5.5 Continued: contraction. Lines show the motion of points along the junction with brighter colors showing higher tension, with $\Lambda(0) = 1$, $\Lambda(1) = 2$. (D) Simulation results of the relative displacement of the two vertices as a function of their relative stiffness. (E) Simulation results of the relative displacement of two vertices as a function of their relative friction. (F) Simulations results of the relative displacement of two vertices as a function of their the relative tension. (G) Experimental data plotting relative motion as a function of relative stiffness. (H) Experimental data of relative displacement as a function of the HECD1 intensity ratio at T-10 before optogenetic activation. (I) Experimental data plotting relative displacement as a function of the RhoA percentage at each vertex. (J-K) Average normalized speed against normalized position from experiments for (J). the less motile vertex, and (K) the motile vertex. Dashed line indicates a linear fit. (L) Tension over friction, equal to the intercept of the fit, and (M) stiffness over friction, equal to the gradient of the fit, for the less-motile and motile vertices.

$$\mu \frac{\partial u}{\partial t} = E \frac{\partial^2 u}{\partial x^2} + \frac{\partial \Lambda}{\partial x} \dots\dots (1)$$

where $u(x,t)$ was the displacement along the junction at time t, and x was the position along the junction. The shoulder junctions were modeled as providing a spring-like resistance to motion, with an effective stiffness k that depended both on both the tension and the geometry of the shoulder junctions. For simplicity we normalize distance by the length of the junction, such that $x = 0$ and $x = 1$ are the ends of the junction and normalize stresses by the Young's modulus of the junction, only keeping the units of time. Force balance at the tricellular vertices was given by

$$\mu \frac{\partial u}{\partial t} = E \frac{\partial u}{\partial x} + \Lambda - k_{LM} u \dots\dots\dots (2)$$

at $x = 0$ and

$$\mu \frac{\partial u}{\partial t} = -E \frac{\partial u}{\partial x} - \Lambda - k_M u \dots\dots (3)$$

at $x = 1$, with k_{LM} and k_M being the stiffnesses of the two shoulder junctions corresponding to the less-motile (LM) and the motile (M) vertices, respectively. We estimate the model parameters by analyzing the motion of vertices measured in experiments. Assuming a simple linear spring model for the effective elastic response at each vertex, $\dot{u_i} = (\Lambda_i - (k_i + E)u_i)/\mu_i$, where Λ_i is the tension acting on the vertex i ($i = LM, M$), μ_i is the friction, and k_i is the shoulder stiffness, we estimate the tension to friction ratio Λ_i/μ_i from the intercept, and stiffness to friction ratio $(k_i + E)/\mu_i$ from the slope of the speed-displacement curve.

To simulate RhoA-induced contraction, we applied a uniform contractile stress for a duration of 5 minutes to a junction initially at rest and recorded the resulting displacements of the two vertices (Figure 5.5c). These displacements were obtained by solving Eq. (1) subject to the boundary conditions given by Eqs (2) and (3). We then used the model to test three different mechanisms for asymmetric vertex motion and heterogeneous mechanical response arising from (i) differential elastic resistance at the shoulder junctions, (ii) differential friction and (iii) asymmetric tension along the junction.

We first tested how the asymmetry in vertex motion was regulated by differential elastic resistance from the shoulder junctions using our continuum mechanical model. For each vertex, we sampled the shoulder junction stiffness k_i from a normal distribution with mean k_0 and standard deviation $k_0/3$. For each vertex, we then compared the percentage of total vertex displacement (relative displacement), $u_i/(u_{LM} + u_M)$, against the percentage of total shoulder stiffness (relative stiffness), $k_i/(k_{LM} + k_M)$. Expectedly, we found that vertex displacement depended linearly on shoulder stiffness, with relative displacement decreasing with increasing relative stiffness (Figure 5.5d).

To test the model predictions using our experimental data, we estimated the elastic resistance at shoulder junctions by computing the tensions along shoulder junctions and change in their geometries during a contraction event, as measured by calculating junction length and the interior angles normal to the activated junction**.** From the angles between the activated junction and its neighbors, we calculated the relative tensions on each junction by balancing forces both along the junction and perpendicular to it. From these tensions, we then calculated the differential change in force due to a change in vertex position, which defines the effective stiffness of the shoulder junctions. However, when we quantified the relative stiffness using data from our optogenetic experiments, we found no correlation with relative vertex displacement (Figure 5.5g), indicating that asymmetric elastic resistance at the vertices do not play a role in predicting asymmetric vertex motion upon contraction.

An alternative mechanism for asymmetric vertex motion could arise from heterogeneous adhesive properties at the tricellular vertices or even along the junction proper that may alter the frictional drag. Indeed, our experimental data showed that there is a marked increase in E-cadherin levels at the less motile vertex compared to the motile one during an optogenetic activation (Figure 5.3a). We therefore sought to test if different frictional forces at the vertices could capture the asymmetric vertex motion. At each vertex, friction was set to a random value sampled from a normal distribution with mean μ_0 and standard deviation $\mu_0/3$, and values were linearly interpolated along the junction. We found a linear dependence of relative displacement on relative friction $\mu_i/(\mu_{LM} + \mu_M)$, with μ_{LM} and μ_M being the friction coefficient at the less-motile and the motile vertices, such that increased friction resulted in reduced motion (Figure 5.5e). As an estimate of the friction in experimental measurements, we measured the relative percentage of HECD1 at each vertex compared to the total amount of HECD1 within each vertex

pair. To our surprise, we did not find any correlation between vertex motion and initial cadherin-mediated friction (Figure 5.5h). Instead, we found that HECD1 intensities were relatively even between each vertex before optogenetic activation.

Finally, we considered the effects of varying tension along the junction induced by RhoA mediated contractility. We varied tension along the junction by setting the tension at each vertex to be a random value sampled from a normal distribution with mean Λ_0 and standard deviation $\Lambda_0/3$, and linearly interpolated tension along the junction. We found that vertices under higher tension (more contractility) underwent larger displacements (Figure 5.5f). To measure relative junction tension, we returned to our CN03 wash in experiments to measure RhoA intensities. We split the junction into two halves and measured the relative intensity of AHPH at each junctional portion compared to the total amount of AHPH along the junction proper. Plotting relative displacement as a function of this percentage of RhoA intensity, we found a correlation between less-motile vertices and the relative amount of junctional RhoA present (Figure 5.5i). Here, data suggested that the closer the RhoA was to a vertex, the less it moved, consistent with our data in Figure 5.2g. This was starkly contrasted to highly motile vertices, which were distal to RhoA regions and experienced little RhoA-mediated tension. Together these data suggest that asymmetries in friction, tension, and stiffness parameters alone were insufficient to explain asymmetries in vertex movement during junction contractions.

5.3.6 RhoA recruitment of E-cadherin reduces vertex motion

Our experimental data demonstrated that vertices with higher recruitment of RhoA moved less (Figure 5.2). In contrast, simulations predicted that tension increased proximal vertex displacements (Figure 5.5f). At the same time, less mobile vertices also showed a marked

increase in E-cadherin levels during an optogenetic activation (Figure 5.3 a-c). This suggests a likely coupling between force and adhesion strength. To explore how these change over time, we plotted the normalized vertex speed as a function of its normalized displacement (Figure 5.5 j-k). We observe that the initial velocity of the less-motile vertex is smaller than the motile vertex (Figure 5.5 j-k, y-intercept). Moreover, the less-motile vertex slows down more rapidly over time (Figure 5.5 j-k, slopes of curves). By assuming a simple linear spring model for vertex displacements, $\dot{u_i} = (\Lambda_i - (k_i + E)u_i)/\mu_i$, we can make estimates of the tension and stiffness relative to the friction and find that the ratio of the tension to friction is lower in the less-motile vertex than the motile vertex (Figure 5.5l). However, the less-motile vertex also has higher levels of RhoA which suggests higher levels of tension. Thus, the overall friction in the less-motile vertex must be overall higher than that of the motile one. Further, since the experimental data showed a higher ratio of stiffness to friction in the less-motile vertices (Figure 5.5m), the local effective stiffness of these is much higher than the motile vertices.

These experimental data motivate introducing a coupling into our model, such that the friction is tension-dependent (Figure 5.6a). This is conceptually like previously described tension-dependent strengthening of focal adhesions (Aratyn-Schaus and Gardel, 2010). With a high coupling between tension and friction, an increase in tension would increase friction to such an extent that the vertex would move slower. Thus, we allowed tension-dependent friction and stiffness by tension along the junction in our continuum model. Again, we varied tension along the junction by setting the tension at each vertex to be a random value sampled from the normal distribution with mean Λ_0 and standard deviation $\Lambda_0/3$, and linearly interpolated tension along the junction. Using a low-force catch bond model, the friction coefficient was given by $\mu(\Lambda) = \mu_M \left(\frac{\mu_{LM}}{\mu_M}\right)^{\Lambda-1}$ where μ_M and μ_{LM} are the estimated mean friction coefficients at the motile and

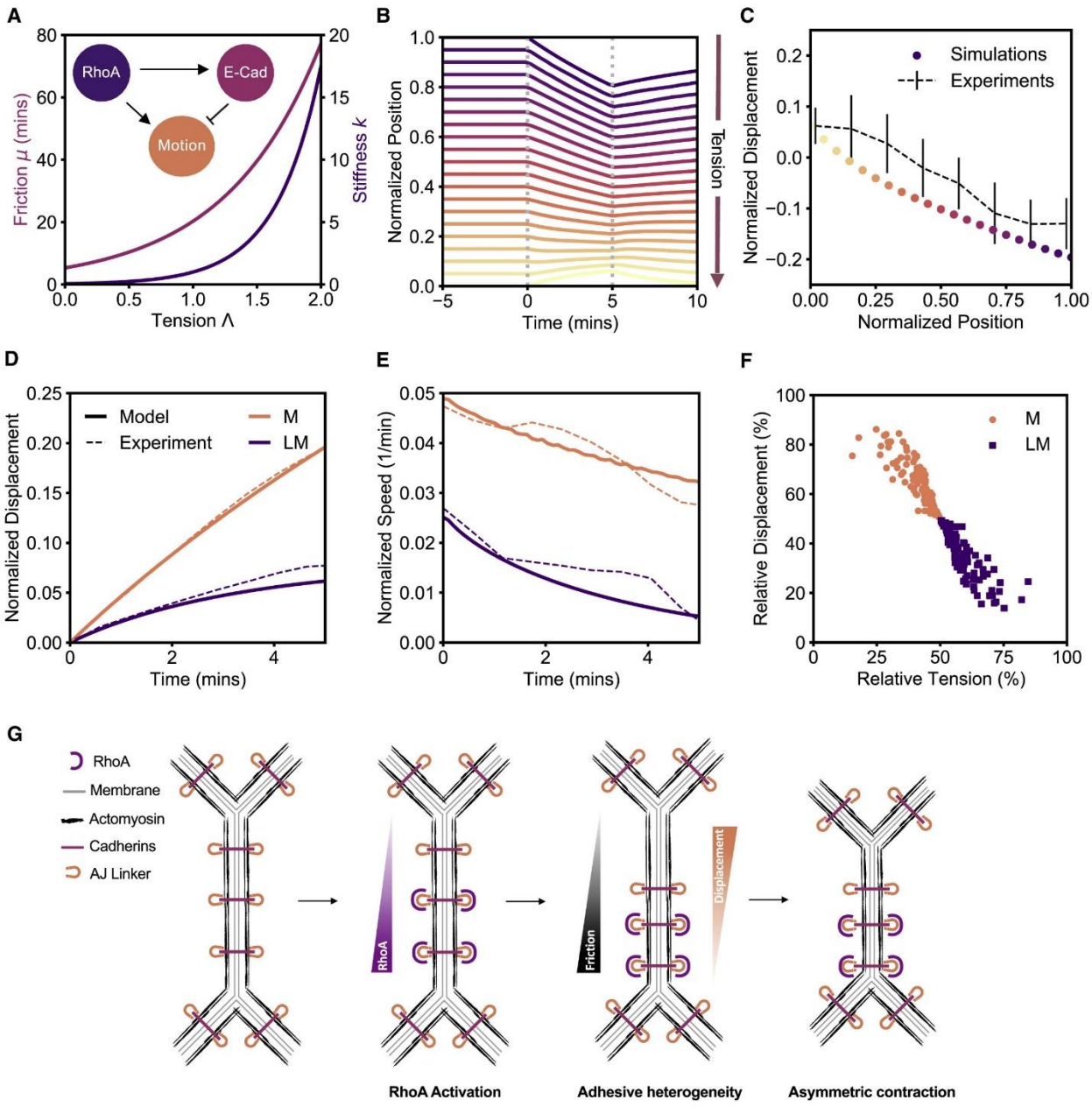

Figure 5.6: Force-dependent adhesion strengthening is sufficient to recapitulate junction dynamics (A) Illustrative coupling of adhesion strength (friction) to tension for strong (pink) and weaker (purple) coupling values. Inset: Rho-dependent increases in E-cadherin adhesion will counteract its effects on local motion. (B) Simulated Kymograph of junction contraction that includes this coupling. Lines show the motion of points along the junction, with brighter colors showing higher tension, using the best fit parameters. (C) Simulated (dots) and experimental (lines) relative displacement against relative position. Error bars show standard deviation. (D) Vertex displacement and (E) vertex speed over time using best fit parameters in the model (solid lines), and in experiments (dashed lines). (F) Normalized displacement against relative tension for the model (solid line), using randomly distributed tensions. (G)

non-motile vertices respectively. Similarly, the shoulder stiffness increases with tension $k(\Lambda) = k_M \left(\frac{k_{LM}}{k_M}\right)^{\Lambda-1}$ where k_M and k_{LM} are the estimated mean stiffnesses at the motile and non-motile vertices respectively (Figure 5.6a).

Placing this coupling into the model is sufficient to quantitatively reproduce the experimental data heterogeneous junction contraction (Figure 5.6 b,c), the asymmetric vertex displacement (Figure 5.6d) and the vertices speeds over time (Figure 5.6e) and the inverse correlation between relative displacement and tension (Figure 5.6f compared to Figure 5.5i). Thus, together these support the notion that force-dependent recruitment of E-cadherin results in increased adhesion strength (e.g. friction) and stiffness at the vertex. Indeed, ours and others' data point to a common coupling mechanism between junctional RhoA and E-cadherin, modulation of which alters the frictional landscape of tricellular vertices (Acharya *et al.*, 2018; Iyer *et al.*, 2019; Noordstra *et al.*, 2021).

5.4 Discussion

We present here a new model for vertex mechanoresponse that that successfully recapitulates asymmetric junction contraction via a coupling between local tension and E-cadherin-mediated adhesion strengthening (Figure 5.6g). We find that RhoA-dependent contraction induces a heterogeneous contraction of the bicellular junction, with the center of contraction and RhoA localization skewed towards the less-motile vertex. In order to quantitatively model these data, we find that asymmetries in junctional stiffness, friction, and tension parameters alone cannot successfully recapitulate experimental data. Instead, we suggest

a coupling of friction with tension such that local RhoA induces both tension and E-cadherin recruitment to increase adhesion strength (and associated friction). Described previously for focal adhesions, this coupling is a natural means to reduce vertex mobility as force increases (Aratyn-Schaus and Gardel, 2010). Incorporating this coupling into our quantitative model, we were able to successfully recapitulate the observed dynamics of Rho-induced junction contraction. Needless to say, the complex feedbacks underlying cell junction dynamics make it difficult to constrain such models and other plausible physical models, including variation in junction elasticity and viscosity, may likely exist.

Our study supports a "clutch" model for tricellular contact engagement during junction contraction. In the absence of RhoA activity, or at distal regions with less RhoA, little E-cadherin is recruited to the vertices. When RhoA-mediated tension is applied to the junction, proximal tricellular adhesions undergo a rapid accumulation of E-cadherin to strengthen adhesion and restrict motion in a process similar to that previously in focal adhesions (Aratyn-Schaus and Gardel, 2010). We envision a similar mechanism operating at tricellular vertices such that mechanosensitive reinforcement of tricellular contacts engages the clutch to strengthen adhesions under load. This adhesion reinforcement restricts vertex motions asymmetrically, as RhoA-mediated tension is stochastically skewed towards one vertex.

These data beg the question as to how RhoA is stochastically placed along the junction. We believe the junction is split into discrete domains that are primed for RhoA activation. These primed regions could be borne out of heterogeneities in adhesive complexes, which exist as puncta along the junction (Cavey *et al.*, 2008). For example, lower junctional E-cadherin levels spatially orient medioapical contractile flows to coordinate junction contractions (Levayer and Lecuit, 2013). These domains' potential for RhoA activation can be exacerbated by the

junctional landscape. The local junction composition, specifically lipid and other protein signaling, could generate these distinct contractile units. Indeed, lifetimes of active GTP-RhoA can be enhanced via a coincidence detection scheme upon cyclic binding to the lipid PIP2 and the junctional protein Anillin (Budnar *et al.*, 2019). Protein-lipid microdomains, scattered along the junction, could therefore create a permissive environment for RhoA activation that is necessary for junction contractions. Spatial heterogeneities in adhesion, lipids, and protein localization could therefore be critical in determining which portion of the junction is capable of activating RhoA. Further work is needed to discern what specifies these unique microdomains.

These data have serious implications for the canonical mathematical models of epithelial tissues. In traditional vertex models, the tissue is a network of edges and nodes whose geometry and topology depends on active forces. The positions of these vertices anchoring bicellular interfaces are determined by the parameters of interfacial tension and pressure within each cell (Fletcher *et al.*, 2014). Vertices can then move in response to mechanical forces, but the extent of this movement is proportional to the parameters describing vertex friction, shoulder edge tension, and tricellular contact stiffness. Using our heterogeneous junction model, no one single parameter describing friction, tension, or stiffness was able to recapitulate experimental data. Instead, we find that the incorporation increases in friction arising from local RhoA activation successfully modeled vertex asymmetry.

Most studies of cell shape changes, to date, concern the movement of bicellular interfaces between two neighboring cells. In development, these junctional zones experience spatially distinct contractile flows that drives qualitatively different and rather opposing junctional responses. Medioapical flows to the bicellular region correspond to junction deformations while flows to the tricellular contacts restrict such contractions (Rauzi *et al.*, 2010; Vanderleest *et al.*,

2018). We see similar junctional responses by optogenetically activating specific junctional zones, with the region of RhoA activation accumulating E-cadherin. Our previous work examining stable junction deformations show that longer optogenetic activations facilitate junction length changes through E-cadherin clustering and internalization9. It would be of interest to see how optogenetic activation of these junctional zones at longer timescales would facilitate their remodeling.

Yet what is the physiological benefit in restricting vertex motion? In the Drosophila Germband, tricellular E-cadherin recruitment is associated with the stabilization of the junctional ratchet. This stabilization ensures progressive interface shortening to facilitate cellular rearrangements (Vanderleest *et al.*, 2018). In our optogenetic system, we do not find stable, irreversible contractions at short timescales but rather reversible junctional deformations. As such, it is unlikely that this vertex reinforcement is sufficient to stabilize junctional shortening. However, it may be necessary to maintain epithelial cohesion under increased tension of neighboring cells. Strong contractions, in principle, could compromise intercellular junctions and barrier functions. Indeed, vertices are principal sites of epithelial fracture in highly tensile epithelia (Acharya *et al.*, 2018). Mechanosensitive reinforcement of vertices could therefore restrict major cell and tissue deformations to maintain tissue homeostasis. This mechanism seems plausible, as RhoA-mediated junctional mechanotransduction is a known regulator of tissue integrity (Acharya *et al.*, 2018).

5.5 Methods

Live-cell imaging and transfection: To ensure a confluent and mature epithelial monolayer, Caco-2 cells were plated densely on 2μm/ml polymerized collagen gels (unless specified

otherwise) (Cavanaugh *et al.*, 2020b, 2020a) coating the bottom of a 4-well Ibidi Chamber (Ibidi). Cells were then allowed to grow for at least 1-2 days to ensure a polarized and confluent monolayer. Ibidi chambers were then placed into a stage incubator with temperature, humidity, and CO2 control (Chamlide TC and FC-5N; Quorum Technologies). All pieces of the stage incubator (stage, adapter, cover, and objective) were maintained at 37C. To analyze RhoA dynamics, 5μg of mCherry-AHPH RhoA biosensor DNA was transfected into GFP E-cadherin CRISPR cells using Lipofectamine 3000 (Invitrogen) at least 24 hours before imaging. For CN03 wash-in experiments, cells were imaged in the 488 and 561 channels every 5 or 8 minutes, until 2 hours of timelapse imaging was completed. At the beginning of imaging, either media or 1μg/ml CN03 was added to the media to document junctional responses. To visualize E-Cadherin in the optogenetic system, we bathed the cells in HECD1 (Abcam) primary and secondary antibody, Alexa Fluor goat Anti-Mouse 647 (Invitrogen), both at a 1:1500 dilution in normal media for at least 24 hours. When applicable, E-cadherin was visualized using DECMA (Abcam) primary and secondary Alexa Fluor Goat Anti-Rat (Invitrogen) antibodies at 1:1500 dilution in normal media for at least 24 hours. Before imaging, cells were washed with PBS and replaced with normal media or media containing chemical perturbations described below. For optogenetic experiments, cells were imaged in the 561 and 647 channel every 35 seconds. The first 10 minutes was to establish a baseline junctional response before the 5-minute optogenetic activation, with the last 15 minutes documenting junctional relaxation. During the activation period, a region around the junction was manually drawn in MetaMorph and adjusted in real time for illumination by the 405nm laser for 1000ms immediately before the acquisition of each image. Laser power was at 1000AU. For junction and vertex movement analysis, via both CN03 and optogenetic means, we chose to analyze junctions that were distal from cell divisions and/or

apoptotic extruding cells to ensure a cohesive monolayer. For picking optogenetic cells, cells were chosen based off of their expression level, which showed junctional recruitment and depletion of the prGEF from the cytosol. All junctions were imaged at the apical plane just below the surface to visualize all vertices and junctional connections.

Drug Treatments: Cells were treated with a 1:1500 dilution DECMA antibody treatment 24 hours before experimentation. Optogenetic and WT cells were treated with 500μM ResEcad (Calbiochem) or 100μM NSC23766 (Tocris) 24-48 hours before optogenetic activation or downstream applications such as fix-and-stains or qPCR.

qPCR: Total RNA was isolated with NucleoSpin kits (Macherey-Nagel). First-strand synthesis was carried out using the SuperScript III system (Invitrogen) with an oligo dT primer and 200 ng of total RNA as input. First-strand reactions were diluted 5-fold and 2 μl was used as template in 20 µl reactions prepared with PrimeTime master mix (IDT) and PrimeTime pre-designed qPCR primer/probe mixtures from IDT (CDH1: Hs.PT.58.3324071; GAPDH: Hs.PT.39a.22214836). A StepOnePlus instrument (Applied Biosystems) was used for running the qPCR reactions. Relative mRNA levels were determined by the 2-ΔΔCt method utilizing GAPDH as a reference gene.

Immunofluorescence: Cells were plated onto polymerized collagen gels coating a Lab Tek II Chamber slide (Thermo Fisher Scientific). Once a confluent monolayer was formed, cells were fixed with 4%PFA with 0.1% Triton X-100 in PBS solution (Corning). Permeabilization was achieved through 0.5% Triton X-100 for 10 min and then cells were blocked with 2.5% BSA and 0.1% Triton X-100 in PBS for one hour. Primary antibody, Paxillin (Millipore) at 1:300 or HECD1 at 1:300, was incubated in blocking solution overnight at 4C and then washed at least 3 times for 20 minutes in 0.1% Triton X-100. Slides were the coated with secondary antibody,

Alexa Fluor Goat anti-Mouse 647 (Invitrogen), and Alexa Fluor phalloidin 488 (ThermoFisher) in blocking solution for one hour. After 3 consecutive 20-minute washes in 0.1% Triton X-100, slide chambers were removed and coated with 20ul ProLong Gold (ThermoFisher Scientific). Slides were then sealed with glass coverslips before drying and sealing with nail polish. Slides were then stored at 4C.

Microscopy: Optogenetic experiments were performed on an inverted Nikon T-E (Nikon, Melville, NY) with a laser merge module with 491, 561, and 642nm laser lines (Spectral Applied Research, Ontario, Canada) with a Yokogawa CSU-X confocal scanning head (Yokogawa Electric, Tokyo, Japan). The Zyla 4.2 sCMOS Camera (Andor, Belfast, UK) collected the images. Optogenetic activation was achieved using a Mosaic digital micromirror device (Andor) attached to a 405nm laser. Images were collected on a 60X 1.2 Plan Apo water (Nikon) objective. MetaMorph Automation and Image Analysis Software (Molecular Devices, Sunnyvale, CA) controlled all hardware. Fix-and-stain and live-cell imaging of CN03 wash-ins were performed on an LSM 980 system with an Airyscan 2 (Zeiss) detector in super resolution-mode with a 63x NA1.4 oil objective (Zeiss). Microscopy software used was the Zen digital imaging suite (Zeiss).

Junction Contraction and Vertex Displacement: Vertex displacement and individual vertex traces were acquired by manually tracking each vertex in a vertex pair using the Manual Tracking tool in Fiji (Schneider *et al.*, 2012). Junction lengths were analyzed by manually measuring in each frame the junction length using the free hand line tool in FIJI software. Junction kymographs were generated with a python script written in FIJI to reconstruct user-drawn line segments along the junction proper. Kymographs were made from unregistered image stacks to preserve asymmetry in junction contraction. Linescans of activated regions and E-

cadherin along the junction were taken using the Plot Profile tool of a hand-drawn line along the junction in FIJI. Linescans were taken before optogenetic activation and after 5 minutes of activation. Junction intensity profiles were then normalized for the junction length from 0 to 1. Contracted length was calculated by dividing the length of the junction at T=5 divided by the length at T=0 during optogenetic activation. Percent movement was calculated as the displacement of each vertex from the original vertex position in a kymograph divided by the sum of both vertex displacements.

Calculating HECD1 Intensities: Vertex fluorescence HECD1 intensities were calculated by drawing a circle around the vertex region in each frame and measuring the intensities over the time course using the FIJI intensity analysis tool. HECD1 fluorescence intensities over time for center-third activations were measured by taking the outline of the activation mask and measuring intensities within that region of activation with the FIJI measure tool. To analyze a region distal to the region of activation, the mask was once again used as a reference length but manually adjusted to exclude tricellular vertices and the activation region.

Quantification of Focal Adhesion Size: To analyze focal adhesion size and number, the paxillin channel was thresholded and made into a binary mask to calculate the area of focal adhesions within a cell, as indicated by boundary edges seen from apical actin staining, as performed in (Huang *et al.*, 2019). The binary mask was then overlaid onto the paxillin channel to segment the image and calculate the area of paxillin with a threshold of $0.25\mu m^2$ and also the number of focal adhesions within that cellular region identified by apical actin staining.

Contractile Uniformity and Center Calculations: Contractile uniformity within each junction was analyzed by manually tracking E-cadherin puncta in each kymograph using the paintbrush tool in FIJI. Both the displacement and position along the junction were normalized by the initial

junction length, and set so that the less-motile vertex has position 0 and the motile vertex has position 1. The maximal displacement of each contracting E-cad puncta as a function of the initial position along the junction was found. The data was then binned by normalized junction position, and the mean and standard deviation plotted (Figure 5.2b). The kymograph's center of contraction was determined by the root value of the linear fit through a graph of vertex displacement vs average distance from junction center, and the center of contraction was then normalized so that the position of the less-motile vertex was 0 and the more motile vertex as 1, meaning the center of the junction would be the position of 0.5. RhoA localization along the junction was found by averaging the AHPH RhoA intensity at the final five timepoints within the kymograph and fitting it to a gaussian using the Matlab fit function. The junction position of the gaussian peak was determined to be the center of RhoA localization and normalized.

Computational model and Model Parameters: Computational model details including a detailed description of the model contractility, friction, equations of motion used, and model parameter values are detailed in (Cavanaugh *et al.*, 2022).

Quantification and statistical analysis: Statistical analysis was performed in Excel, GraphPad Prism, and Matlab, to establish statistical significance under specific experimental conditions. Where applicable, boxes indicate Standard Deviation and whiskers indicate Standard Error. Normally distributed data were analyzed for significance with ****=$p<0.0001$, ***=$p<0.0009$, and **=$p<0.05$ as calculated by the two-tailed Student's t-Test. Bimodal data was calculated for significance using a Hartigan Dip Test (Hartigan and Hartigan, 1985). n represents the number of junctions or vertices analyzed in each experiment, which is indicated in the figure and its respective legend. Data was only excluded if the optogenetically activated junction was proximal

to a cell division event and/or extruding cell because this mechanical perturbation affected local junctional mechanics within the analyzed tissue area.

Chapter 6: Atherosclerotic-like shear stresses alter cytoskeletal organization, cell-cell junctions, and LIM protein localization

6.1 Preface and Abstract

6.1.1 Preface

The following chapter is work which grew out of a collaboration with Shailaja Seetharaman, a post-doc in the Gardel lab. Shailaja conceived of the experiment, performed the experiments and provided guidance of interpretation of the results. The shear stress experiments were carries out through a collaboration with Professor Yun Fang's lab at the University of Chicago. My contribution to this project has been in the image analysis of this project as well as the data representation in the form of graphs, figures, and other visuals. This includes generating novel methods of preferential protein localization, relative intensity and position, and junctional characterization. This chapter is a summary of our collective work in the analysis and interpretation of this project and is currently unpublished.

6.1.2 Abstract

Mechanical forces are exerted on the endothelial cells of blood vessels during blood flow. These forces act as cues that drive overall vascular homeostasis and can profoundly alter various regulatory mechanism in the endothelial tissue. Numerous members of the evolutionarily conserved superfamily of LIM domain proteins including FHL2 have been implicated in actin cytoskeletal mechanosensitivity. Here, we experimentally manipulate apical fluidic shear stress applied to model endothelial tissue to determine how FHL2 relocalizes to tensed structures in cells. Here, we report loss of cell shape alignment and altered junctional characteristics resulting in the increased presence of focal adherens junctions compared to linear adherens junctions in

tissue under atherosclerotic-like shear stress conditions as well as enrichment of FHL2 at stress fibers under the conditions of this disturbed flow.

6.2 Introduction

Blood vessels experience constant and repeated shear mechanical forces due to blood flow. In healthy vessels under physiological conditions, this blood flow is largely laminar with minimal turbulence and flow moving parallel to the vessel walls (Gordon *et al.*, 2020). Disturbed, non-laminar flow occurs at places in the blood vessel where the vessel bends, branches, or constricts due to obstruction (Cooke, 2003). Greater obstruction, such as under atherosclerotic conditions, causes increased disturbed flow and additional stress on the tissue (Li *et al.*, 2014).

This disturbed flow and associated shear stress is known to be mechanically sensed by the endothelial cells in the blood vessels and cause substantial changes to tissue phenotype. Endothelial cells under disturbed flow conditions show reduced cell shape alignment (Topper and Gimbrone Jr, 1999), increased cell turnover (Davies *et al.*, 1986), weakened cell-cell junctions (Krouwer *et al.*, 2012), increased inflammation (Zhou *et al.*, 2014; Wu *et al.*, 2017), and reduced focal adhesion size (Ting *et al.*, 2012), all of which indicates that these stress cues are being translated to the cell through mechanosensitive signals. However, it remains unclear precisely how this shear force is sensed by the endothelial tissue and by what mechanism they respond under both physiological and pathological conditions.

The actin cytoskeleton and its related regulatory and accessory proteins are a critical sensor of mechanical stress in the cells and is largely responsible for translating mechanical

information from stress sensors to regulatory mechanisms throughout the cell (Chanet and Martin, 2014; Fang *et al.*, 2019). In particular, the superfamily of LIM-domain proteins has been shown to mediate mechanosensitive signal transduction within the actin cytoskeleton (Khurana *et al.*, 2002; Sun *et al.*, 2020; Anderson *et al.*, 2021). LIM-domain proteins, named for the three homeodomain proteins where it was discovered Lin1 1, Isl-1, and Mec-3, contain one or more regions of double zinc finger motifs in the protein structure (Bach, 2000). This superfamily of proteins are a critical component of mechanical signaling pathways and have been implicated in numerous strain-sensing regulatory roles including stress fiber remodeling and repair (Smith *et al.*, 2010), cell adhesion mechanisms (Brown *et al.*, 1998; Razzell *et al.*, 2018; Anderson *et al.*, 2021) , and substrate stiffness detection (Wang *et al.*, 2021; Swiatlowska *et al.*, 2022).

The protein Four-and-a-half LIM -2 (FHL2) is a member of this LIM-domain superfamily, and in particular is highly expressed in vascular endothelial tissue (Neuman *et al.*, 2009) with demonstrated roles in mediating the inflammatory response in blood vessel walls (van de Pol *et al.*, 2020) and thickening of arterial walls (Chen *et al.*, 2020). Additionally, depletion of FHL2 decreases atherosclerotic symptoms in mice and improves overall vascular outcomes (Kong *et al.*, 2001; Ebrahimian *et al.*, 2015), further indicating that FHL2 is an important mediator of mechanical stress in endothelial tissue.

Here, we experimentally manipulate apical shear stress applied to model endothelial tissue to determine how FHL2 relocalizes under shear mechanical forces. We report higher junctional tension in tissue under atherosclerotic-like disturbed flow conditions with altered junctional shape and organization. We also show shear stress dependent FHL2 localization to actin stress fibers.

6.3 Results

6.3.1 Disturbed atherosclerotic-like flow affects junctional shape and tissue organization

Blood vessels experience distinct shear fluid forces depending on the shape of the blood vessel. Healthy open blood vessels undergo mostly unidirectional laminar flow in the blood vessel with most of the forces associated with the fluid flow parallel to the cells lining the vessels. In contrast, atherosclerotic-like blood vessels force fluid through a constricted passage which results in disturbed turbulent flow with increased shear stress applied directly to the tissue (Figure 6.1a) (Li *et al.*, 2014). To measure the response of endothelial tissue to atherosclerotic-like disturbed flow conditions, we grew human aortic TeloHAEC endothelial cells to confluence and applied either uniform or disturbed flow patterns to the surface of the tissue for 24 hours. The flow patterns were generated using a rotating metal cone attached to a UMD-17 stepper motor from Arcus Technology to mimic either unidirectional or disturbed flow patterns found in human carotid arteries (Wu *et al.*, 2015, 2017). These results were then fixed and immunostained for actin, FHL2, and the junctional protein vascular endothelial cadherin (VE-cadherin).

Using the VE-cadherin stains to outline cell shape in the endothelial tissue, we can see that under unidirectional flow cells are elongated horizontally as they align with the direction of the laminar flow (Figure 6.1b, left). This is not the case for the tissue under disturbed flow. These cells more circular (Figure 6.1d) and have little directional alignment (Figure 6.1b, right). When we take a closer look at the structure of the cell-cell junctions (Figure 6.1b, bottom), we also see that while adherens junctions under unidirectional flow are linear with few disruptions or breaks, adherens junctions under disturbed flow show a much more feathered structure with significant gaps in the VE-cadherin presence (Figure 6.1c). Despite these significant changes to

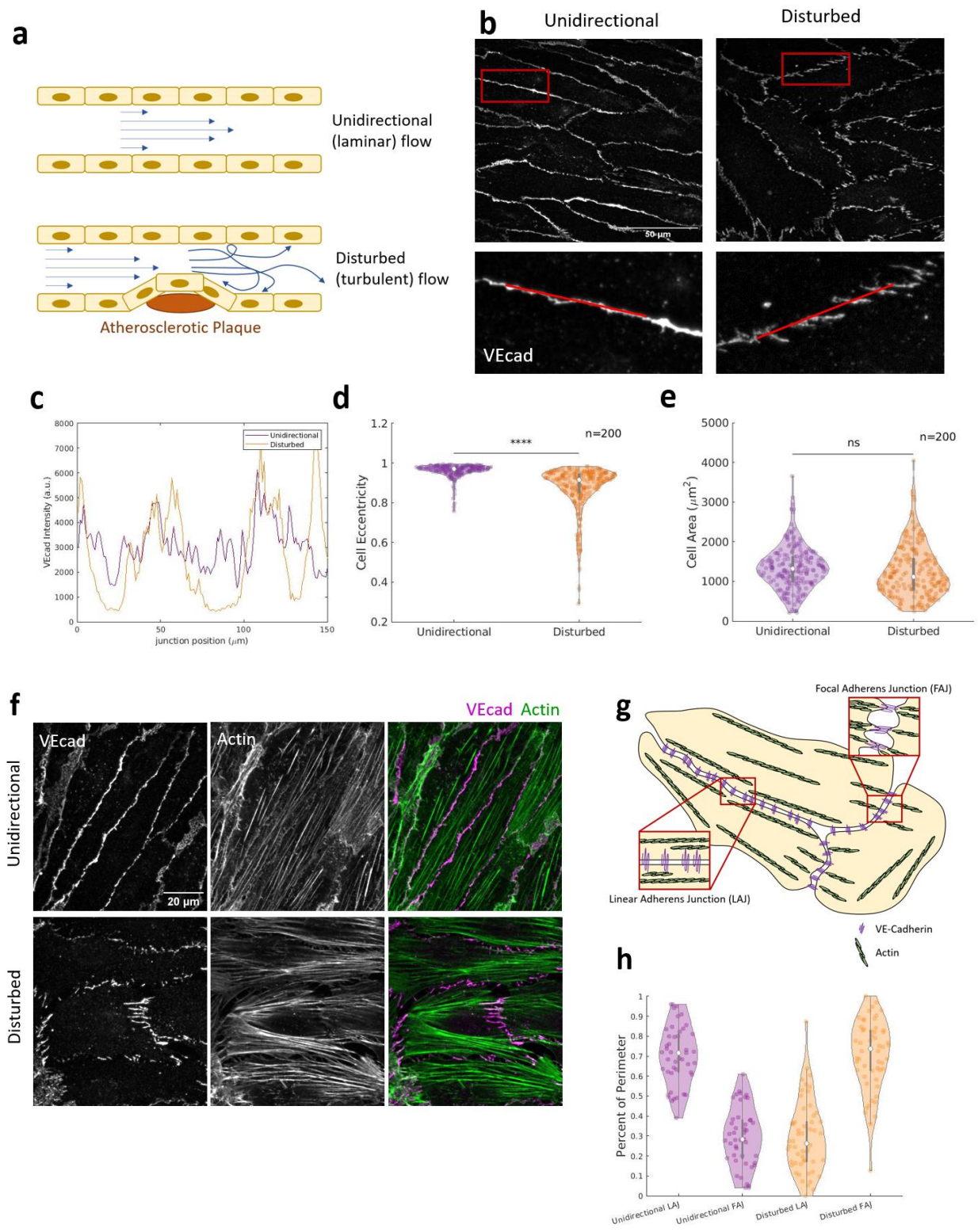

Figure 6.1: Disturbed atherosclerotic-like flow affects junctional shape and tissue organization (a) Diagram of health (top) and atherosclerotic-like (bottom) flow in a blood vessel lined with endothelial cells and the resulting pattern of blood flow. (b) Immunostained

Figure 6.1 Continued: VE-Cadherin (VEcad) of cells experiencing either unidirectional or disturbed flow for 24 hours prior to fixation. (c) Line scans of VE-cadherin intensity across junctional cross section given by red line in b. (d) Violin plot of cell eccentricity (n=200). ****=$p<0.000001$ as calculated by the student's t-test. (e) Violin plot of cell areas (n=200). ns=$p>0.05$ as calculated by the student's t-test. (f) Immunostained VE-cadherin and phalloidin stained actin. (g) Diagram of linear and focal adherens junctions in endothelial tissue based on the structure of actin and VE-cadherin in the immediate vicinity of the adherens junction. (h) Violin plot of the percent of the perimeter represented by either linear adherens junctions (LAJ,) or focal adherens junctions (FAJ). For each sample type, unidirectional (n=45) or disturbed (n=54), the percent of linear and focal adherens junctions sum to 100%.

tissue structure and membrane organization, both unidirectional and disturbed samples maintained similar cross sectional cell areas (Figure 6.1e).

By examining how phalloidin stained actin interacts with the VE-cadherin at the cell-cell junctions, we can characterize differences in tension at cell junctions between cells under unidirectional and disturbed flow (Figure 6.1f). This tension differential is observed through the comparison of linear and focal adherens junctions in the tissue. Linear adherens junctions are defined by a continuous and clearly defined junction with actin filaments running parallel to the cell membrane while focal adherens junctions are characterized by a discontinuous punctate-like appearance of the junction and actin bundles oriented perpendicular to the junction (Figure 6.1g) (Angulo-Urarte *et al.*, 2020). These distinct junctional phenotypes have well studied differences in local membrane tension with linear adherens junctions under lower mechanical tension and focal adherens junctions under higher mechanical tension (Huveneers *et al.*, 2012; Oldenburg and de Rooij, 2014).

We see that cells under unidirectional flow have a greater percentage of linear adherens junctions compared to focal adherens junctions with an average of 70% of cell perimeters across 45 measured cells characterized by linear adherens junctions and 30% by focal adherens

junctions. In comparison, cells under disturbed flow have an average of 29% linear adherens junctions in the perimeter of 54 measured cells and have 71% focal adherens junctions (Figures 6.1 h). This difference in junctional makeup indicated that cells under disturbed flow are characterized by cell-cell junctions under higher mechanical tension than cells under unidirectional flow.

6.3.2 FHL2 localizes to stress fibers under tension in disturbed atherosclerotic-like flow

Because we are interested in understanding the mechanism for how information about mechanical tension is transmitted biochemically, we chose to examine the localization of the LIM domain protein FHL2. Immunostaining for actin and FHL2, we find that FHL2 while FHL2 is fairly dispersed throughout the cytoplasm in unidirectional cells, FHL2 localizes to stress fibers in the disturbed samples (Figure 6.2a). This can be seen in line scans of the stained stress fibers where we observe that for cells experiencing unidirectional flow the punctate FHL2 only occasionally colocalize at peaks of actin intensity (Figure 6.2b), but in the cells experiencing disturbed flow, stress fibers have a much stronger colocalization with FHL2 (Figure 6.2c).

In order to better quantify the colocalization between FHL2 and actin under these two flow conditions, we took rectangle scans of 100 different stress fibers with varying actin intensities. These rectangle scans were drawn perpendicular to the stress fiber (Figure 6.2d, solid line) and took the mean intensity of both actin and FHL2 within 3μm of the scan line (Figure 6.2d, dotted line). A rectangle scan was used in this analysis instead of a simple line scan due to the punctate nature of FHL2, averaging over the intensity reduces the effect of small FHL2 puncta affecting the overall average intensity. We use these line scans to find the peak actin intensity, representing the center of the stress fiber, and record the FHL2 intensity at that point of

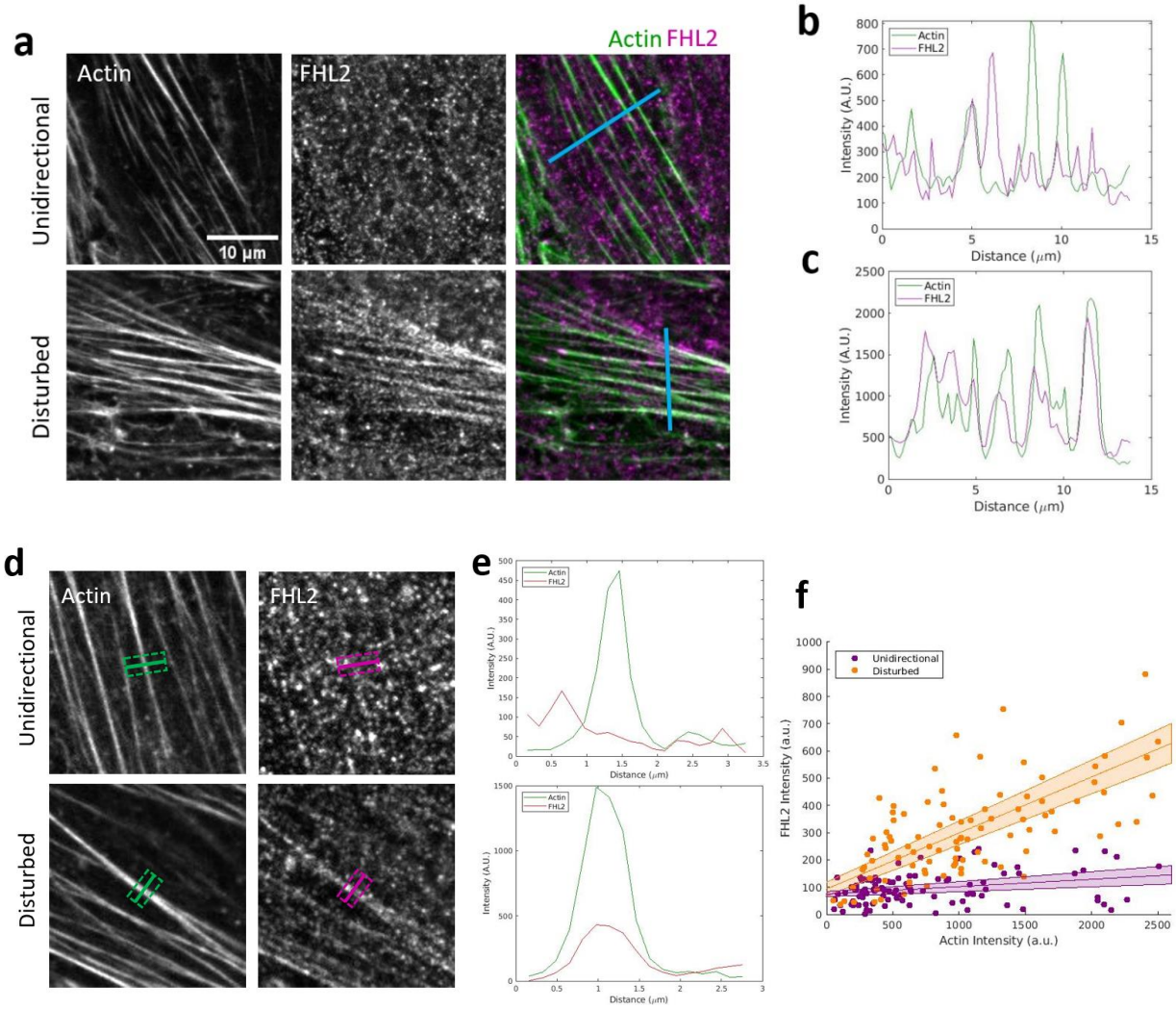

Figure 6.2: FHL2 localizes to stress fibers under tension in disturbed atherosclerotic-like flow (a) Immunostained FHL2 and phalloidin stained actin for cells experiencing unidirectional or disturbed flow for 24 hours. (b) Line scans of actin and FHL2 intensity across stress fibers of sample experiencing unidirectional flow from blue line given in a (top). (c) Line scans of actin and FHL2 intensity across stress fibers of sample experiencing disturbed flow from blue line given in a (bottom). (d) Sample rectangle scans taken across stress fibers. Solid line represents the direction of the scan across the stress fiber. Dotted line rectangle represents the 3μm range averaged over to generate a mean fluorescent intensity across the scan. (e) Sample traces of the rectangle scan for unidirectional (top) and disturbed (bottom) stress fibers. Distance is measured along the solid line in d. (f) Relative FHL2 and actin intensities at the location of the peak actin intensity along the rectangle scan (n=100). Slopes calculated using linear regression analysis. Shading represents the region of 68% confidence for the measurement of the slope and y-intercept of the linear fit.

the rectangle scan (Figure 6.2e). From here, we plot the actin and FHL2 intensity for each of these 100 stress fibers (Figure 6.2f). In cells experiencing both unidirectional and disturbed flows, there is a wide variety of actin intensities, indicating that cells in both conditions contain both high-intensity fibers with thick bundles of actin and lower intensity fibers with actin bundled into thinner structures. We find that in the case of cells experiencing unidirectional flow, no matter how high intensity and thickly bundled the actin stress fiber is, FHL2 does not strongly colocalize. In cells experiencing disturbed atherosclerotic-like flow however, there is a strong correlation between the intensity of the actin stress fiber and the localization of FHL2 to that stress fiber, indicating that under these conditions FHL2 not only localizes to stress fibers, but localizes more strongly to stress fibers with more actin.

6.3.3 Overexpression of FHL2 in cases of unidirectional flow mimic effects of disturbed atherosclerotic-like flow

In order to further examine the relationship between FHL2, cellular tension, and junctional shape under atherosclerotic-like flow conditions, we employ a Tet-On line of TeloHAEC cells. In the presence of doxycycline (+dox), these cells experience the overexpression of FHL2. When we expose these FHL2 overexpressing cells to either unidirectional or disturbed flow, we find that the shape of the cells in unidirectional flow drastically changes (Figure 6.3a). These cells are much more similar in shape to their disturbed flow counterparts with reduced elongation causing them to take on a more circular shape (Figure 6.3b). They also have a larger spread area than either the +dox cells under disturbed flow (Figure 6.3c) or either sample type with normal levels of FHL2 expression (Figure 6.1e).

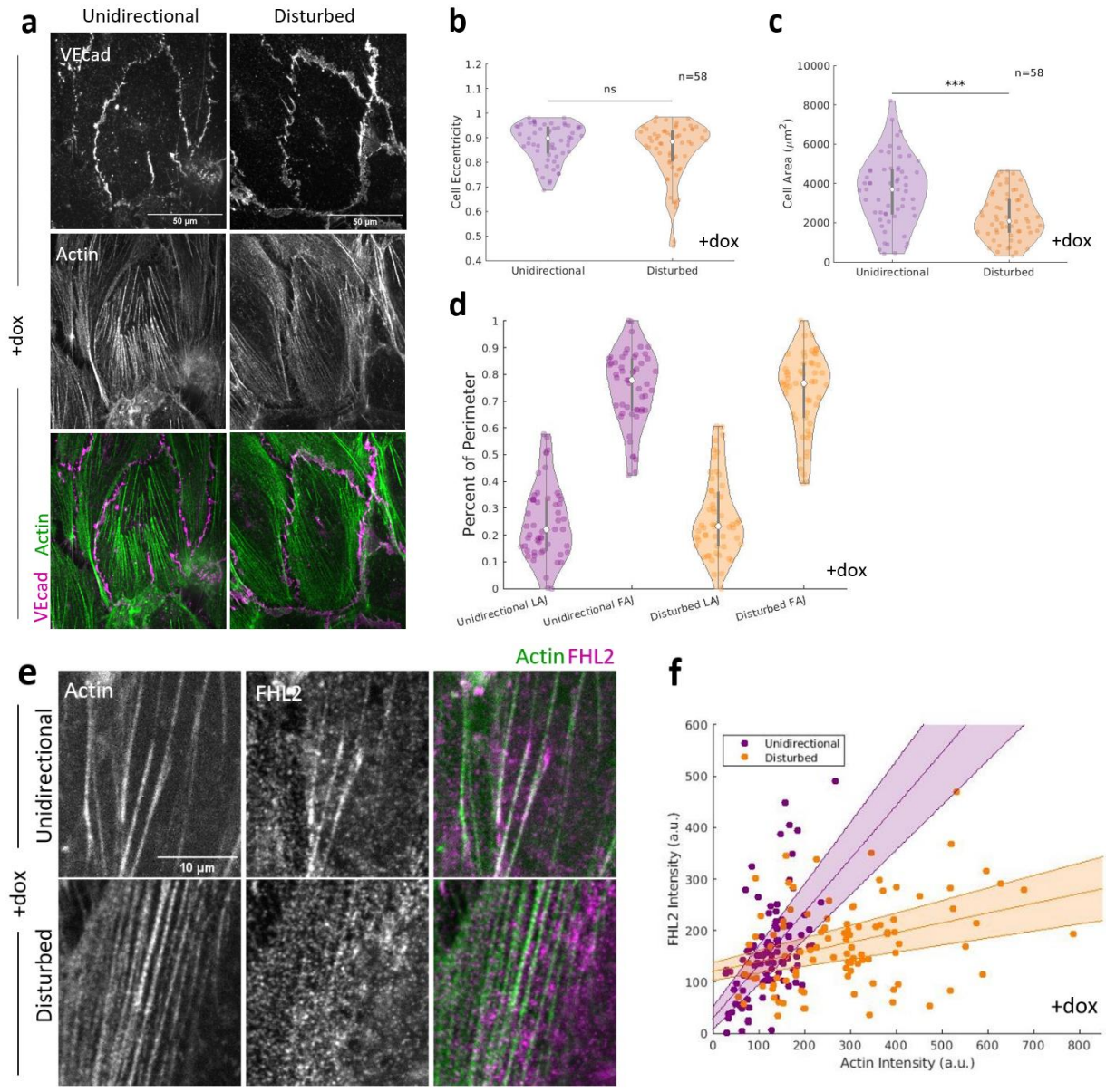

Figure 6.3: Overexpression of FHL2 in cases of unidirectional flow mimic effects of disturbed atherosclerotic-like flow (a) Immunostained VE-cadherin and phalloidin stained actin for Tet-inducible FHL2 overexpressing cells. 100 ng/μl doxycycline added 24 hours prior to application of flow onto the cells in order to stimulate FHL2 overexpression (+dox). (b) Violin plot of cell eccentricity in FHL2 overexpressing cells (n=58). ns=p>0.05 as calculated by the student's t-test. (c) Violin plot of cell areas in FHL2 overexpressing cells (n=58). ***=p<0.01 as calculated by the student's t-test. (d) Violin plot of the percent of the perimeter represented by either linear adherens junctions (LAJ,) or focal adherens junctions (FAJ) in FHL2 overexpressing cells. For each sample type, unidirectional (n=58) or disturbed (n=58), the percent of linear and focal adherens junctions sum to 100%. (e) Immunostained FHL2 and phalloidin stained actin for FHL2 overexpressing cells. (f) Relative FHL2 and actin

Figure 6.3 Continued: intensities at the location of the peak actin intensity along the rectangle scan (n=100). Slopes calculated using linear regression analysis. Shading represents the region of 68% confidence for the measurement of the slope and y-intercept of the linear fit.

When we then examine the makeup of the adherens junctions of these FHL2 overexpressing cells, we find that once again the cells under unidirectional flow more closely resemble their disturbed counterparts with an average of 78% of the total junctions appearing as focal adherens junctions compared to an average of 77% for the cells under disturbed flow (Figure 6.3d). This indicates that even in the case of unidirectional flow, the overexpression of FHL2 leads to increased mechanical tension in the tissue as shown by the structure of the adherens junction.

In addition to FHL2 overexpression resembling the effects of disturbed flow in cases of unidirectional flow, we find that excess FHL2 in these samples localizes to stress fibers through immunofluorescent stains (Figure 6.3e). Unlike in cells expressing normal amount of FHL2, these +dox cells experiencing unidirectional flow show FHL2 localizing to stress fibers similar to what we expect to see in the case of disturbed flow. Using the same method of quantification described for Figure 6.2f, we see that in the case of unidirectional flow with FHL2 overexpression, not only is there a lack of high-intensity thick stress fibers in these cells, but FHL2 strongly localizes to these stress fibers (Figure 6.3f).

Taken together, we are able to show that the overexpression of FHL2 mimics the effects of disturbed atherosclerotic-like flow in cases of more healthy unidirectional flow, changing the overall shape of cells in the tissue, increasing the observed mechanical tension at the cell-cell junctions, and localizing to stress fibers. This allows us to conclude that FHL2 plays a role in

reinforcing the actin cytoskeleton and mechanical tension in the tissue in response to the increased shear stress experienced from more turbulent flow.

6.4 Discussion

Our data reveals that atherosclerotic-like flow has a genuine impact on tissue morphology that affects tissue shape, junctional structure, and the localization of the mechanosensitive protein FHL2. More disturbed, turbulent flow in blood vessels naturally places higher stress on the endothelial cells lining the vessel (Li *et al.*, 2014). Here we show that the tissue responds to this increased stress with a loss of cell alignment as the elongated cells under unidirectional flow are parallel to the direction of flow while the cells under a disturbed flow lose their elongation and thus their directionality. This increased and turbulent shear stress also affects junctional composition as the adherens junction show increased amounts of focal adherens junctions compared to linear adherens junctions. As focal adherens junctions are strongly associated with areas of high mechanical tension within the tissue (Huveneers *et al.*, 2012; Oldenburg and de Rooij, 2014), our data indicates increased mechanical tension not just incident on the tissue as a result of atherosclerotic-like flow, but also as a direct result of that flow.

Our search for the molecular mechanism for mediating this ability of endothelial cells to sense increased shear stress from fluid flow and translate that into mechanical tension in the cells lead us to the LIM domain protein FHL2. Our results agree with similar findings (Nakazawa *et al.*, 2016; Wagh *et al.*, 2021) that FHL2 localizes to areas of high mechanical tension in a cell as they show increased affinity for actin stress fibers in the cells under disturbed flow with higher all around mechanical tension. While FHL2 has been shown to behave in a force sensing manner, our results directly link this behavior to atherosclerotic-like flow in blood vessels.

As we work to further understand the molecular mechanism of this mechanical relationship between strain sensing and atherosclerotic-like flow, there are important follow-up experiments which we are working to perform an analyze. One being that there is evidence that activated RhoA may attract LIM domain proteins to attach to stress fibers at sites of strain (Sala and Oakes, 2021) and we want to better understand the role of RhoA and other GTPases which may mediate this reaction. Another approach which we would like to explore is the role of additional force sensitive proteins implicated in vascular disease, namely Pdlim7 and LIMD1 (Krcmery *et al.*, 2013; Wang *et al.*, 2021). Is the role of FHL2 in strain sensing within endothelial tissue under exposure to disturbed flow limited to just FHL2, or is it a general role of force sensitive LIM domain proteins in blood vessel walls?

6.5 Materials and Methods

Cell Culture: Human aortic endothelial (TeloHAEC) cells were cultured in EGM-2 and supplemented with SingleQuots from Lonza (CC-3156 and CC-417.) Cells were incubated in a humidified environment at 37°C and 5% $C0_2$. To generate samples for the flow device, cells were plated densely in 6-well plates and grown for 24 hours. 4% dextran (Sigma-Aldrich) was added to sample media before exposure to flow. In all FHL2 overexpression experiments, Tet-inducible gene expression was activated with 100 ng/µl doxycycline (+dox) 24 hours prior to application of flow.

Application of Flow: Flow was generated using a computerized stepper motor (Arcus Technology) with an attached stainless-steel cone which generates shear stresses for the unidirectional and disturbed flow. Sample cells were placed withing this flow device for 24

hours prior to fixation in an incubator at 37°C and 5% CO2. More details on the nature of this flow mechanism are given in (Wu *et al.*, 2017).

Staining: Prior to fixation, cells were washed with 1xPBS. Cells were fixed in a solution of 4% PFA in 1x Cytoskeletal for 15 minutes at room temperature. Fixed cells were permeabilized using a solution 0.2% Triton X-100 in 1xPBS for 5 minutes, and then blocked with 5% BSA in 1x PBS for 30 min. Primary antibodies were prepared in 5% BSA solution using 1:1000 anti-VEcadherin, and 1:100 anti-FHL2 and incubated for 1 hour. Secondary antibodies were 1:500 Alexa Fluor phalloidin, 1:100 Alexa Fluor Rb 560, and 1:1000 Alexa Fluor anti-mouse 647.

Microscopy and Imaging: Samples were imaged on an inverted T-E microscope (Nikon) with a confocal CSU-X spinning disk (Yokogawa Electric Corporation), a stage controller (Prior), a CMOS camera (Zyla-Andor), and 491, 561, and 642 laser lines. Metamorph software was used to control the microscope and collect images. Images were acquired using a 60x Plan Apo NA water immersion objective with a NA of 1.20 and a WD of 0.31-0.28 (Nikon). Images were acquired at room temperature.

Violin Plots: The width of each colored region represents volume kernel density which is an estimation of the probability density function of the average measurement. The white point represents the median measurement for all cells, and the grey bar represents the interquartile range, meaning the middle 50% of the volume range.

Cell Area and Eccentricity Measurements: Cells were segmented by hand using Fiji image analysis software to find the outline of cell-cell junctions in multiple cells and fields of view across the sample. Custom Matlab code was then used to find individual cell areas and fit the

outline of each cell to an ellipse. The major and minor axis of this ellipse was then used to measure the eccentricity of each cell.

Analysis of Linear and Focal Adherens Junctions: Using the outlines of cell-cell junctions generated through cell segmentation, Composite images of VE-cadherin and actin were examined to determine the nature of the adherens junction in different areas along the tissue. Every region of each segmented cell perimeter was marked as either liner or focal by referencing the shape of the VE-cadherin and actin in the vicinity of the junction. Segmented cell perimeters where junctions are defined by a continuous VE-cadherin with actin filaments running parallel to the cell membrane were marked as linear adherens junctions. Regions of the segmented perimeter where the VE-Cadherin junction was discontinuous with punctate-like features and actin bundles oriented perpendicular to the junction were marked as focal adherens junctions. Matlab code was then used to measure the percent of each cell's perimeter marked as each.

Stress Fiber Rectangle Scans and Intensity Measurements: Stress fibers were identified in 100 separate cells for each measurement. Stress fibers were deliberately selected to provide intensities along a wide range of actin intensities when possible and so represent the intensity range of the population of stress fibers in each sample, but not the distribution. The peak intensity of each selected stress fiber was measured using a rectangle scan. A line was drawn perpendicularly across the stress fiber and the mean intensity across that line was measured within 3μm of the scan line. The peak intensity of actin is then located from this rectangle scan, indicating the center of the stress fiber, and FHL2 intensity at the stress fiber is calculated based on the location of the peak actin intensity.

Quantification and Statistical Analysis: Image analysis and quantification was performed in Fiji, Excel, and Matlab. Matlab was used to perform statistical analysis and calculate statistical

significance using two-tailed student t-tests where ns=$p>0.05$, *=$p<0.05$, **=$p<0.01$, ***=$p<0.0001$ and ****=$p<0.000001$.

Appendix A: Extended Protocols

A.1 Live Cell Imaging

Live Sample Preparation: To prepare cells for live cell imaging, add imaging media to sample when preparing sample for the microscope. The lack of phenol-red dye of this media helps reduce autofluorescence in your sample and the additional hepes buffer helps to keep cells in a CO_2 rich environment.

50 ml Imaging Media: Appropriate for MDCK cells

45 ml phenol-red free DMEM (17-205-CV)

4.5 ml FBS

225 µl Pen-Strep

225 µl L-Glutamine

450 µl hepes (1M)

Incubation: When imaging cells for 2 hours or less on the microscope, it may be appropriate to use the Nevtek airstream incubator to keep the sample warm as opposed to an enclosed incubator. The Nevtek heater resembles a hairdryer and can keep most cells happy and unstressed when imaging for 2 hours or less. If you are imaging any longer or are working with particularly sensitive cells, use one of the enclosed incubators. Be sure to warm the incubators up at lest 20 minutes prior to use. If you are having any issues with humidity in the incubator chamber, line the chamber with ~6 Kimwipes soaked in water to help maintain humidity.

Cell Mask Orange Membrane Stain: When imaging live cell samples, I prefer to stain cell membranes with 2µl/ml of CellMask Orange (Invitrogen) 30 minutes prior to staining. The stain is good for imaging for approximately 5 hours after wash-in, after which it begins to be internalized by the cell and starts to outline internal cell membranes such as the nuclear

membrane. The stain occasionally fails and results in bright globs of dye across the sample. If this occurs, toss the aliquot and use a new one, being careful that each time you defrost the new aliquot you use it immediately and move it back to the freezer as quickly as possible. The aliquots are very sensitive to repeated cycles of freezing and thawing as well as remaining at high temperatures for longer than 5 minutes.

A.2 Osmotic Shock Treatment

For my experiments, I used sorbitol to apply a hyperosmotic shock to my cells. After changing the media to wash-in the sorbitol containing media, the cells took approximately 30 minutes to reduce in size, and then about 3 hours to recover their volume afterwards in the case that they recovered it. When changing the media to add sorbitol, be extremely gentle, as cell volumes change in react to agitation as well as osmotic pressure. I used sorbitol amounts ranging from 100mM to 500mM. Most of my final work has cells in 200mM sorbitol, any less and you don't see significant volume reduction, and at around 400-500mM cells start to undergo apoptosis and extrusion.

A.3 PDMS Fabrication and Biocompatibility

PDMS Fabrication

1. Weigh out 1:10 ratio of crosslinker to base
2. Place in vacuum desiccator for 30 minutes.
3. Carefully pour solution into mold, can be any glass or plastic dish or a more complex mold
4. Cure in 70°C incubator overnight

PDMS Biocompatible:

1. Soak 90 seconds in 100% acetone

2. Soak PDMS in 1xPBS overnight
3. Immediately before adding to sample, place in UV ozone for 2 minutes (if growing cells on top of PDMS substrate, do this immediately before adding a collagen layer)

A.4 Electrotaxis Protocol

Sample Creation: After creating a biocompatible PDMS mask as described above, press the mask onto a 50mm glass bottom petri dish with a 30mm glass diameter (MatTek). The purpose of using this specialized dish is to give you room to work with the agar salt bridge later. The low sides of the imaging chamber and the extra area will make it significantly easier to maneuver around during setup than a standard 25mm magnetic imaging chamber. Grow cells to confluency as needed and remove mask 2 hours prior to imaging. Be gentle during removal, it's possible for the mask to lift up the entire monolayer and destroy the sample.

Agar Bridge: Prep the agar at least 20 minutes before you mean to start assembling the electrotaxis setup. Add 2% agarose to 5ml PBS in an Erlenmeyer flask and stop the top up loosely with a Kimwipe. Microwave the solution until the agarose is dissolved stopping each time it starts to boil over. Pour into a petri dish and leave to solidify at room temperature for 10-15 minutes. Using a razer blade, cut agar into two strips 1.5cm wide and 6 cm long.

Assembly: Attach stage incubator to microscope (Chamlide and Quorum Technologies) and add sample first. This moderately protects the microscope in the event that there is a spill as it prevents any direct openings to the objective or center of the stage. Add 2 wells of 3 ml PBS to either side of the imaging chamber using 10cm petri dishes. Don't spill anything. Add agar bridges to connect each PBS well to the sample, aligning them so that they are 1 cm apart and centered on the area of the sample you want to image. Connect the variable DC power supply

(Vlifree) with wires to silver electrodes and add electrodes to PBS well using tape to hold wires in place.

Imaging: Most videos were taken for 2 minutes imaging every second. At the 20 second mark I pressed the output button on the power supply to turn on the voltage and pressed the same button again at 40 seconds to turn it off. I repeated this at 60-80 seconds. When the voltage was on and at 10V, the instrument registered a non-zero but very small current. If there was an issue with the connection and I saw the current was 0 when the output was on, then I knew there was a connection issue somewhere. At smaller currents (<5V) the current was too small for the power supply to measure, and I couldn't perform that check with this setup.

Fluo-8: Calcium was visualized using fluo-8 (Invitrogen). 2μM Fluo-8 was added to samples 30 minutes prior to imaging and illuminated with a 491nm laser. Fluo-8 aliquots are very sensitive to the freeze/thaw cycle. I used a new aliquot for each day of imaging. After approximately an hour of imaging, the dye began to degrade. The dy did not significantly bleed through to other channels and can be used with a Cellmask Orange stain to outline cell membranes.

Bibliography

Acharya, BR et al. (2018). A Mechanosensitive RhoA Pathway that Protects Epithelia against Acute Tensile Stress. Dev Cell 47, 439-452.e6.

Acharya, BR, Wu, SK, Lieu, ZZ, Parton, RG, Grill, SW, Bershadsky, AD, Gomez, GA, and Yap, AS (2017). Mammalian Diaphanous 1 Mediates a Pathway for E-cadherin to Stabilize Epithelial Barriers through Junctional Contractility. Cell Rep 18, 2854–2867.

Alt, S, Ganguly, P, and Salbreux, G (2017). Vertex models: from cell mechanics to tissue morphogenesis. Philos Trans R Soc B Biol Sci 372, 20150520.

Amano, M, Ito, M, Kimura, K, Fukata, Y, Chihara, K, Nakano, T, Matsuura, Y, and Kaibuchi, K (1996). Phosphorylation and Activation of Myosin by Rho-associated Kinase (Rho-kinase) *. J Biol Chem 271, 20246–20249.

Anderson, CA, Kovar, DR, Gardel, ML, and Winkelman, JD (2021). LIM domain proteins in cell mechanobiology. Cytoskeleton 78, 303–311.

Angulo-Urarte, A, van der Wal, T, and Huveneers, S (2020). Cell-cell junctions as sensors and transducers of mechanical forces. Biochim Biophys Acta BBA - Biomembr 1862, 183316.

Anti, M, Armuzzi, A, and Gasbarrini, G (1998). Epithelial cell turnover and apoptosis. Ital J Gastroenterol Hepatol 30 Suppl 3, S276-8.

Aratyn-Schaus, Y, and Gardel, ML (2010). Transient Frictional Slip between Integrin and the ECM in Focal Adhesions under Myosin II Tension. Curr Biol 20, 1145–1153.

Armstrong, CM, and Hille, B (1998). Voltage-Gated Ion Channels and Electrical Excitability. Neuron 20, 371–380.

Bach, I (2000). The LIM domain: regulation by association. Mech Dev 91, 5–17.

Beck, FX, Burger-Kentischer, A, and Müller, E (1998). Cellular response to osmotic stress in the renal medulla. Pflugers Arch 436, 814–827.

Benninger, RKP, Zhang, M, Head, WS, Satin, LS, and Piston, DW (2008). Gap Junction Coupling and Calcium Waves in the Pancreatic Islet. Biophys J 95, 5048–5061.

Bertet, C, Sulak, L, and Lecuit, T (2004). Myosin-dependent junction remodelling controls planar cell intercalation and axis elongation. Nature 429, 667–671.

Bi, D, Lopez, JH, Schwarz, JM, and Manning, ML (2015). A density-independent rigidity transition in biological tissues. Nat Phys 11, 1074–1079.

Bi, D, Yang, X, Marchetti, MC, and Manning, ML (2016). Motility-Driven Glass and Jamming Transitions in Biological Tissues. Phys Rev X 6, 021011.

Blanchoin, L, Boujemaa-Paterski, R, Sykes, C, and Plastino, J (2014). Actin Dynamics, Architecture, and Mechanics in Cell Motility. Physiol Rev 94, 235–263.

Bozzone, D, and Light, D (2021). Cells, Tissue, and Skin, Third Edition, Infobase Holdings, Inc.

Brown, MC, Perrotta, JA, and Turner, CE (1998). Serine and Threonine Phosphorylation of the Paxillin LIM Domains Regulates Paxillin Focal Adhesion Localization and Cell Adhesion to Fibronectin. Mol Biol Cell 9, 1803–1816.

Brückner, BR, and Janshoff, A (2018). Importance of integrity of cell-cell junctions for the mechanics of confluent MDCK II cells. Sci Rep 8, 14117.

Bruewer, M, Hopkins, AM, Hobert, ME, Nusrat, A, and Madara, JL (2004). RhoA, Rac1, and Cdc42 exert distinct effects on epithelial barrier via selective structural and biochemical modulation of junctional proteins and F-actin. Am J Physiol-Cell Physiol 287, C327–C335.

Buckley, CD, Tan, J, Anderson, KL, Hanein, D, Volkmann, N, Weis, WI, Nelson, WJ, and Dunn, AR (2014). Cell adhesion. The minimal cadherin-catenin complex binds to actin filaments under force. Science 346, 1254211.

Buckley, CE, and St Johnston, D (2022). Apical–basal polarity and the control of epithelial form and function. Nat Rev Mol Cell Biol 23, 559–577.

Budnar, S, Husain, KB, Gomez, GA, Naghibosadat, M, Varma, A, Verma, S, Hamilton, NA, Morris, RG, and Yap, AS (2019). Anillin Promotes Cell Contractility by Cyclic Resetting of RhoA Residence Kinetics. Dev Cell 49, 894-906.e12.

Burlacu, S, Janmey, PA, and Borejdo, J (1992). Distribution of actin filament lengths measured by fluorescence microscopy. Am J Physiol-Cell Physiol 262, C569–C577.

Carmosino, M, Giménez, I, Caplan, M, and Forbush, B (2008). Exon Loss Accounts for Differential Sorting of Na-K-Cl Cotransporters in Polarized Epithelial Cells. Mol Biol Cell 19, 4341–4351.

Cavanaugh, KE, Oakes, PW, and Gardel, ML (2020a). Optogenetic Control of RhoA to Probe Subcellular Mechanochemical Circuitry. Curr Protoc Cell Biol 86, e102.

Cavanaugh, KE, Staddon, MF, Chmiel, TA, Harmon, R, Budnar, S, Yap, AS, Banerjee, S, and Gardel, ML (2022). Force-dependent intercellular adhesion strengthening underlies asymmetric adherens junction contraction. Curr Biol 32, 1986-2000.e5.

Cavanaugh, KE, Staddon, MF, Munro, E, Banerjee, S, and Gardel, ML (2020b). RhoA Mediates Epithelial Cell Shape Changes via Mechanosensitive Endocytosis. Dev Cell 52, 152-166.e5.

Cavey, M, Rauzi, M, Lenne, P-F, and Lecuit, T (2008). A two-tiered mechanism for stabilization and immobilization of E-cadherin. Nature 453, 751–756.

Chanet, S, and Martin, AC (2014). Chapter Thirteen - Mechanical Force Sensing in Tissues. In: Progress in Molecular Biology and Translational Science, ed. AJ Engler, and S Kumar, Academic Press, 317–352.

Cheah, YJ, Buyong, MR, and Mohd Yunus, MH (2021). Wound Healing with Electrical Stimulation Technologies: A Review. Polymers 13, 3790.

Chen, C, Tsai, H, Tsai, S, Chu, P, Huang, P, Chen, J, and Lin, S (2020). Deletion of the FHL2 gene attenuates intima-media thickening in a partially ligated carotid artery ligated mouse model. J Cell Mol Med 24, 160–173.

Choi, W, Acharya, BR, Peyret, G, Fardin, M-A, Mège, R-M, Ladoux, B, Yap, AS, Fanning, AS, and Peifer, M (2016). Remodeling the zonula adherens in response to tension and the role of afadin in this response. J Cell Biol 213, 243–260.

Cole, J, and Gagnon, Z (2019). A flow-based microfluidic device for spatially quantifying intracellular calcium ion activity during cellular electrotaxis. Biomicrofluidics 13, 064107.

Collins, C, Denisin, AK, Pruitt, BL, and Nelson, WJ (2017). Changes in E-cadherin rigidity sensing regulate cell adhesion. Proc Natl Acad Sci 114, E5835–E5844.

Colombelli, J, Besser, A, Kress, H, Reynaud, EG, Girard, P, Caussinus, E, Haselmann, U, Small, JV, Schwarz, US, and Stelzer, EHK (2009). Mechanosensing in actin stress fibers revealed by a close correlation between force and protein localization. J Cell Sci 122, 1665–1679.

Cooke, JP (2003). Flow, NO, and atherogenesis. Proc Natl Acad Sci 100, 768–770.

Cooper, GM (2000). Structure and Organization of Actin Filaments. Cell Mol Approach 2nd Ed.

Cortese, B, Palamà, IE, D'Amone, S, and Gigli, G (2014). Influence of electrotaxis on cell behaviour. Integr Biol 6, 817–830.

Craig, R, and Woodhead, JL (2006). Structure and function of myosin filaments. Curr Opin Struct Biol 16, 204–212.

Czirok, A, Isai, DG, and Neufeld, Z (2016). Mechanics of cell motility within stratified epithelia. FASEB J 30, 1031.2-1031.2.

Dasbiswas, K, Hu, S, Schnorrer, F, Safran, SA, and Bershadsky, AD (2018). Ordering of myosin II filaments driven by mechanical forces: experiments and theory. Philos Trans R Soc B Biol Sci 373, 20170114.

Davies, PF, Remuzzi, A, Gordon, EJ, Dewey, CF, and Gimbrone, MA (1986). Turbulent fluid shear stress induces vascular endothelial cell turnover in vitro. Proc Natl Acad Sci U S A 83, 2114–2117.

Delpire, E, and Gagnon, KB (2018). Water Homeostasis and Cell Volume Maintenance and Regulation. In: Current Topics in Membranes, Elsevier, 3–52.

Delva, E, Tucker, DK, and Kowalczyk, AP (2009). The Desmosome. Cold Spring Harb Perspect Biol 1, a002543.

Desai, LP, Aryal, AM, Ceacareanu, B, Hassid, A, and Waters, CM (2004). RhoA and Rac1 are both required for efficient wound closure of airway epithelial cells. Am J Physiol-Lung Cell Mol Physiol 287, L1134–L1144.

Devany, J, Falk, MJ, Holt, LJ, Murugan, A, and Gardel, ML (2022). Tissue confinement regulates cell growth and size in epithelia. 2022.07.04.498508.

Devany, J, Sussman, DM, Yamamoto, T, Manning, ML, and Gardel, ML (2021). Cell cycle–dependent active stress drives epithelia remodeling. Proc Natl Acad Sci 118, e1917853118.

Di Meglio, I, Trushko, A, Guillamat, P, Blanch-Mercader, C, and Roux, A (2021). Pressure and curvature control of contact inhibition in epithelia growing under spherical confinement, Cell Biology.

Dominguez, R, and Holmes, KC (2011). Actin Structure and Function. Annu Rev Biophys 40, 169–186.

Du, X, Osterfield, M, and Shvartsman, SY (2014). Computational analysis of three-dimensional epithelial morphogenesis using vertex models. Phys Biol 11, 066007.

Durney, CH, and Feng, JJ (2021). A three-dimensional vertex model for Drosophila salivary gland invagination. Phys Biol 18, 046005.

Ebrahimian, T, Simon, D, Lemarié, CA, Simeone, S, Heidari, M, Mann, KK, Wassmann, S, and Lehoux, S (2015). Absence of Four-and-a-Half LIM Domain Protein 2 Decreases Atherosclerosis in ApoE−/− Mice. Arterioscler Thromb Vasc Biol 35, 1190–1197.

Elmas, O (2016). Effects of electromagnetic field exposure on the heart: a systematic review. Toxicol Ind Health 32, 76–82.

Etienne-Manneville, S, and Hall, A (2002). Rho GTPases in cell biology. Nature 420, 629–635.

Ettensohn, CA (1985). Mechanisms of Epithelial Invagination. Q Rev Biol 60, 289–307.

Fang, Y, Wu, D, and Birukov, KG (2019). Mechanosensing and Mechanoregulation of Endothelial Cell Functions. Compr Physiol 9, 873–904.

Farhadifar, R, Röper, J-C, Aigouy, B, Eaton, S, and Jülicher, F (2007). The Influence of Cell Mechanics, Cell-Cell Interactions, and Proliferation on Epithelial Packing. Curr Biol 17, 2095–2104.

Fernandez-Gonzalez, R, and Zallen, JA (2011). Oscillatory behaviors and hierarchical assembly of contractile structures in intercalating cells. Phys Biol 8, 045005.

Finan, JD, and Guilak, F (2010). The effects of osmotic stress on the structure and function of the cell nucleus. J Cell Biochem 109, 460–467.

Fischbarg, J (2010). Fluid Transport Across Leaky Epithelia: Central Role of the Tight Junction and Supporting Role of Aquaporins. Physiol Rev 90, 1271–1290.

Fletcher, AG, Osterfield, M, Baker, RE, and Shvartsman, SY (2014). Vertex Models of Epithelial Morphogenesis. Biophys J 106, 2291–2304.

Fletcher, DA, and Mullins, RD (2010). Cell mechanics and the cytoskeleton. Nature 463, 485–492.

Fozzard, HA (1977). Heart: Excitation-Contraction Coupling. Annu Rev Physiol 39, 201–220.

Garcia, MA, Nelson, WJ, and Chavez, N (2018). Cell–Cell Junctions Organize Structural and Signaling Networks. Cold Spring Harb Perspect Biol 10, a029181.

García-Mata, R, and Burridge, K (2007). Catching a GEF by its tail. Trends Cell Biol 17, 36–43.

Gardel, ML, Schneider, IC, Aratyn-Schaus, Y, and Waterman, CM (2010). Mechanical integration of actin and adhesion dynamics in cell migration. Annu Rev Cell Dev Biol 26, 315–333.

Gaush, CR, Hard, WL, and Smith, TF (1966). Characterization of an Established Line of Canine Kidney Cells (MDCK). Proc Soc Exp Biol Med 122, 931–935.

Gerthoffer, WT, and Gunst, SJ (2001). Invited Review: Focal adhesion and small heat shock proteins in the regulation of actin remodeling and contractility in smooth muscle. J Appl Physiol 91, 963–972.

Geselowitz, DB (1973). Electric and Magnetic Field of the Heart. Annu Rev Biophys Bioeng 2, 37–64.

Geyti, CS, Odgaard, E, Overgaard, MT, Jensen, MEJ, Leipziger, J, and Praetorius, HA (2008). Slow spontaneous [Ca2+]i oscillations reflect nucleotide release from renal epithelia. Pflüg Arch - Eur J Physiol 455, 1105–1117.

Gibson, MC, and Perrimon, N (2003). Apicobasal polarization: epithelial form and function. Curr Opin Cell Biol 15, 747–752.

Gilles-Baillien, M, and Gilles, R (2012). Intestinal Transport: Fundamental and Comparative Aspects, Springer Science & Business Media.

Gomes, RC, Guirro, ECO, Gonçalves, AC, Farina Junior, JA, Murta Junior, LO, and Guirro, RRJ (2018). High-voltage electric stimulation of the donor site of skin grafts accelerates the healing process. A randomized blinded clinical trial. Burns J Int Soc Burn Inj 44, 636–645.

Gómez-Gálvez, P, Vicente-Munuera, P, Anbari, S, Buceta, J, and Escudero, LM (2021). The complex three-dimensional organization of epithelial tissues. Development 148, dev195669.

González-Mariscal, L, Betanzos, A, Nava, P, and Jaramillo, BE (2003). Tight junction proteins. Prog Biophys Mol Biol 81, 1–44.

Goodlad, RA (2017). Quantification of epithelial cell proliferation, cell dynamics, and cell kinetics in vivo. WIREs Dev Biol 6, e274.

Gordon, E, Schimmel, L, and Frye, M (2020). The Importance of Mechanical Forces for in vitro Endothelial Cell Biology. Front Physiol 11.

Green, KJ, and Jones, JCR (1996). Desmosomes and hemidesmosomes: structure and function of molecular components. FASEB J 10, 871–881.

Greer, PL, and Greenberg, ME (2008). From Synapse to Nucleus: Calcium-Dependent Gene Transcription in the Control of Synapse Development and Function. Neuron 59, 846–860.

Grewe, J, and Schwarz, US (2020). Mechanosensitive self-assembly of myosin II minifilaments. Phys Rev E 101, 022402.

Günzel, D, and Yu, ASL (2013). Claudins and the Modulation of Tight Junction Permeability. Physiol Rev 93, 525–569.

Guo, W, and Wang, Y (2007). Retrograde Fluxes of Focal Adhesion Proteins in Response to Cell Migration and Mechanical Signals. Mol Biol Cell 18, 4519–4527.

Haas, M (1994). The Na-K-Cl cotransporters. Am J Physiol-Cell Physiol 267, C869–C885.

Harmon, RM, Devany, J, and Gardel, ML (2022). Dia1 coordinates differentiation and cell sorting in a stratified epithelium. J Cell Biol 221, e202101008.

Harris, TJC (2012). An Introduction to Adherens Junctions: From Molecular Mechanisms to Tissue Development and Disease. In: Adherens Junctions: From Molecular Mechanisms to Tissue Development and Disease, ed. T Harris, Dordrecht: Springer Netherlands, 1–5.

Hartigan, JA, and Hartigan, PM (1985). The Dip Test of Unimodality. Ann Stat 13, 70–84.

Hartman, MA, and Spudich, JA (2012). The myosin superfamily at a glance. J Cell Sci 125, 1627–1632.

Hirase, T, Kawashima, S, Wong, EYM, Ueyama, T, Rikitake, Y, Tsukita, S, Yokoyama, M, and Staddon, JM (2001). Regulation of Tight Junction Permeability and Occludin Phosphorylation by RhoA-p160ROCK-dependent and -independent Mechanisms *. J Biol Chem 276, 10423–10431.

Hirashima, T, and Adachi, T (2019). Polarized cellular mechano-response system for maintaining radial size in developing epithelial tubes. Development 146, dev181206.

Hirsch, M, and Noske, W (1993). The tight junction: Structure and function. Micron 24, 325–352.

Hoenderop, JGJ, Nilius, B, and Bindels, RJM (2005). Calcium Absorption Across Epithelia. Physiol Rev 85, 373–422.

Hoffmann, EK, Lambert, IH, and Pedersen, SF (2009). Physiology of Cell Volume Regulation in Vertebrates. Physiol Rev 89, 193–277.

Hohmann, T, and Dehghani, F (2019). The Cytoskeleton—A Complex Interacting Meshwork. Cells 8, 362.

Holthöfer, B, Windoffer, R, Troyanovsky, S, and Leube, RE (2007). Structure and Function of Desmosomes. In: International Review of Cytology, Academic Press, 65–163.

Hong, S, Troyanovsky, RB, and Troyanovsky, SM (2013). Binding to F-actin guides cadherin cluster assembly, stability, and movement. J Cell Biol 201, 131–143.

Huang, JX, Lee, G, Cavanaugh, KE, Chang, JW, Gardel, ML, and Moellering, RE (2019). High throughput discovery of functional protein modifications by Hotspot Thermal Profiling. Nat Methods 16, 894–901.

Huebner, RJ, Malmi-Kakkada, AN, Sarıkaya, S, Weng, S, Thirumalai, D, and Wallingford, JB (2021). Mechanical heterogeneity along single cell-cell junctions is driven by lateral clustering of cadherins during vertebrate axis elongation. ELife 10, e65390.

Humphries, MJ (2000). Integrin Structure. Biochem Soc Trans 28, 311–340.

Huttenlocher, A, Ginsberg, MH, and Horwitz, AF (1996). Modulation of cell migration by integrin-mediated cytoskeletal linkages and ligand-binding affinity. J Cell Biol 134, 1551–1562.

Huveneers, S, Oldenburg, J, Spanjaard, E, van der Krogt, G, Grigoriev, I, Akhmanova, A, Rehmann, H, and de Rooij, J (2012). Vinculin associates with endothelial VE-cadherin junctions to control force-dependent remodeling. J Cell Biol 196, 641–652.

Irfan Maqsood, M, Matin, MM, Bahrami, AR, and Ghasroldasht, MM (2013). Immortality of cell lines: challenges and advantages of establishment. Cell Biol Int 37, 1038–1045.

Itoh, M, Tsukita, S, Yamazaki, Y, and Sugimoto, H (2012). Rho GTP exchange factor ARHGEF11 regulates the integrity of epithelial junctions by connecting ZO-1 and RhoA-Myosin II signaling. Proc Natl Acad Sci 109, 9905–9910.

Iyer, KV, Piscitello-Gómez, R, Paijmans, J, Jülicher, F, and Eaton, S (2019). Epithelial Viscoelasticity Is Regulated by Mechanosensitive E-cadherin Turnover. Curr Biol 29, 578-591.e5.

Kao, F-C, Ho, H-H, Chiu, P-Y, Hsieh, M-K, Liao, J, Lai, P-L, Huang, Y-F, Dong, M-Y, Tsai, T-T, and Lin, Z-H (2022). Self-assisted wound healing using piezoelectric and triboelectric nanogenerators. Sci Technol Adv Mater 23, 1–16.

Keller, R, Davidson, LA, and Shook, DR (2003). How we are shaped: The biomechanics of gastrulation. Differentiation 71, 171–205.

Kerridge, S, Munjal, A, Philippe, J-M, Jha, A, de las Bayonas, AG, Saurin, AJ, and Lecuit, T (2016). Modular activation of Rho1 by GPCR signalling imparts polarized myosin II activation during morphogenesis. Nat Cell Biol 18, 261–270.

Khurana, T, Khurana, B, and Noegel, AA (2002). LIM proteins: association with the actin cytoskeleton. Protoplasma 219, 1–12.

Kondo, T, and Hayashi, S (2015). Mechanisms of cell height changes that mediate epithelial invagination. Dev Growth Differ 57, 313–323.

Kong, Y, Shelton, JM, Rothermel, B, Li, X, Richardson, JA, Bassel-Duby, R, and Williams, RS (2001). Cardiac-Specific LIM Protein FHL2 Modifies the Hypertrophic Response to β-Adrenergic Stimulation. Circulation 103, 2731–2738.

Koride, S, Loza, AJ, and Sun, SX (2018). Epithelial vertex models with active biochemical regulation of contractility can explain organized collective cell motility. APL Bioeng 2, 031906.

Koumangoye, R, Omer, S, and Delpire, E (2018). Mistargeting of a truncated Na-K-2Cl cotransporter in epithelial cells. Am J Physiol Cell Physiol 315, C258–C276.

Koumangoye, R, Omer, S, Kabeer, MH, and Delpire, E (2020). Novel Human NKCC1 Mutations Cause Defects in Goblet Cell Mucus Secretion and Chronic Inflammation. Cell Mol Gastroenterol Hepatol 9, 239–255.

Kovács, M, Tóth, J, Hetényi, C, Málnási-Csizmadia, A, and Sellers, JR (2004). Mechanism of Blebbistatin Inhibition of Myosin II. J Biol Chem 279, 35557–35563.

Krcmery, J, Gupta, R, Sadleir, RW, Ahrens, MJ, Misener, S, Kamide, C, Fitchev, P, Losordo, DW, Crawford, SE, and Simon, H-G (2013). Loss of the Cytoskeletal Protein Pdlim7 Predisposes Mice to Heart Defects and Hemostatic Dysfunction. PLOS ONE 8, e80809.

Krouwer, VJD, Hekking, LHP, Langelaar-Makkinje, M, Regan-Klapisz, E, and Post, JA (2012). Endothelial cell senescence is associated with disrupted cell-cell junctions and increased monolayer permeability. Vasc Cell 4, 12.

Kumar, NM, and Gilula, NB (1996). The Gap Junction Communication Channel. Cell 84, 381–388.

Lalli, ML, and Asthagiri, AR (2015). Collective Migration Exhibits Greater Sensitivity But Slower Dynamics of Alignment to Applied Electric Fields. Cell Mol Bioeng 8, 247–257.

Lawson-Keister, E, and Manning, ML (2021). Jamming and arrest of cell motion in biological tissues. Curr Opin Cell Biol 72, 146–155.

Lecuit, T, Lenne, P-F, and Munro, E (2011). Force Generation, Transmission, and Integration during Cell and Tissue Morphogenesis. Annu Rev Cell Dev Biol 27, 157–184.

Lee, B, Moon, KM, and Kim, CY (2018). Tight Junction in the Intestinal Epithelium: Its Association with Diseases and Regulation by Phytochemicals. J Immunol Res 2018, e2645465.

Lee, DBN, Huang, E, and Ward, HJ (2006). Tight junction biology and kidney dysfunction. Am J Physiol-Ren Physiol 290, F20–F34.

Lee, J-Y, and Harland, RM (2010). Endocytosis Is Required for Efficient Apical Constriction during Xenopus Gastrulation. Curr Biol 20, 253–258.

Lessey, EC, Guilluy, C, and Burridge, K (2012). From Mechanical Force to RhoA Activation. Biochemistry 51, 7420–7432.

Levayer, R, and Lecuit, T (2013). Oscillation and Polarity of E-Cadherin Asymmetries Control Actomyosin Flow Patterns during Morphogenesis. Dev Cell 26, 162–175.

Levayer, R, Pelissier-Monier, A, and Lecuit, T (2011). Spatial regulation of Dia and Myosin-II by RhoGEF2 controls initiation of E-cadherin endocytosis during epithelial morphogenesis. Nat Cell Biol 13, 529–540.

Li, L et al. (2012). E-cadherin plays an essential role in collective directional migration of large epithelial sheets. Cell Mol Life Sci CMLS 69, 2779–2789.

Li, L, He, Y, Zhao, M, and Jiang, J (2013). Collective cell migration: Implications for wound healing and cancer invasion. Burns Trauma 1, 2321-3868.113331.

Li, X, Yang, Q, Wang, Z, and Wei, D (2014). Shear Stress in Atherosclerotic Plaque Determination. DNA Cell Biol 33, 830–838.

Liang, X et al. (2017). Tyrosine dephosphorylated cortactin downregulates contractility at the epithelial zonula adherens through SRGAP1. Nat Commun 8, 790.

Liu, W-Y, Wang, Z-B, Zhang, L-C, Wei, X, and Li, L (2012). Tight Junction in Blood-Brain Barrier: An Overview of Structure, Regulation, and Regulator Substances. CNS Neurosci Ther 18, 609–615.

Liu, Z, Tan, JL, Cohen, DM, Yang, MT, Sniadecki, NJ, Ruiz, SA, Nelson, CM, and Chen, CS (2010). Mechanical tugging force regulates the size of cell–cell junctions. Proc Natl Acad Sci 107, 9944–9949.

Lloyd-Lewis, B, Gobbo, F, Perkins, M, Jacquemin, G, Huyghe, M, Faraldo, MM, and Fre, S (2022). In vivo imaging of mammary epithelial cell dynamics in response to lineage-biased Wnt/β-catenin activation. Cell Rep 38, 110461.

Lommel, ATL van (2003). From Cells to Organs: A Histology Textbook and Atlas, Springer Science & Business Media.

Long, Y et al. (2018). Effective Wound Healing Enabled by Discrete Alternative Electric Fields from Wearable Nanogenerators. ACS Nano 12, 12533–12540.

Lunkenheimer, P, Schneider, U, Brand, R, and Loid, A (2000). Glassy dynamics. Contemp Phys 41, 15–36.

Luo, T, Mohan, K, Iglesias, PA, and Robinson, DN (2013). Molecular mechanisms of cellular mechanosensing. Nat Mater 12, 1064–1071.

Macara, IG, Guyer, R, Richardson, G, Huo, Y, and Ahmed, SM (2014). Epithelial Homeostasis. Curr Biol 24, R815–R825.

Mackay, DJG, and Hall, A (1998). Rho GTPases *. J Biol Chem 273, 20685–20688.

Mackenzie, IC, and Fusenig, NE (1983). Regeneration of Organized Epithelial Structure. J Invest Dermatol 81, S189–S194.

Mader, CC, Hinchcliffe, EH, and Wang, Y (2007). Probing cell shape regulation with patterned substratum: requirement of myosin II-mediated contractility. Soft Matter 3, 357–363.

Maekawa, M, Ishizaki, T, Boku, S, Watanabe, N, Fujita, A, Iwamatsu, A, Obinata, T, Ohashi, K, Mizuno, K, and Narumiya, S (1999). Signaling from Rho to the actin cytoskeleton through protein kinases ROCK and LIM-kinase. Science 285, 895–898.

Manibog, K, Li, H, Rakshit, S, and Sivasankar, S (2014). Resolving the molecular mechanism of cadherin catch bond formation. Nat Commun 5, 3941.

Marieb, EN (1995). Human anatomy and physiology, Redwood City, Calif. : Benjamin/Cummings.

Mason, FM, Tworoger, M, and Martin, AC (2013). Apical domain polarization localizes actin–myosin activity to drive ratchet-like apical constriction. Nat Cell Biol 15, 926–936.

Mason, FM, Xie, S, Vasquez, CG, Tworoger, M, and Martin, AC (2016). RhoA GTPase inhibition organizes contraction during epithelial morphogenesis. J Cell Biol 214, 603–617.

Mattila, PK, and Lappalainen, P (2008). Filopodia: molecular architecture and cellular functions. Nat Rev Mol Cell Biol 9, 446–454.

Mazzochi, C, Benos, DJ, and Smith, PR (2006). Interaction of epithelial ion channels with the actin-based cytoskeleton. Am J Physiol Renal Physiol 291, F1113-1122.

McMillan, JR, and Shimizu, H (2001). Desmosomes: Structure and Function in Normal and Diseased Epidermis. J Dermatol 28, 291–298.

Meng, W, and Takeichi, M (2009). Adherens Junction: Molecular Architecture and Regulation. Cold Spring Harb Perspect Biol 1, a002899.

Messal, HA, Alt, S, Ferreira, RMM, Gribben, C, Wang, VM-Y, Cotoi, CG, Salbreux, G, and Behrens, A (2019). Tissue curvature and apicobasal mechanical tension imbalance instruct cancer morphogenesis. Nature 566, 126–130.

Miller, C, McGuiness, W, Wilson, S, Cooper, K, Swanson, T, Rooney, D, Piller, N, and Woodward, M (2017). Venous leg ulcer healing with electric stimulation therapy: a pilot randomised controlled trial. J Wound Care 26, 88–98.

Munjal, A, Philippe, J-M, Munro, E, and Lecuit, T (2015). A self-organized biomechanical network drives shape changes during tissue morphogenesis. Nature 524, 351–355.

Mykoniatis, A et al. (2010). Phorbol 12-myristate 13-acetate-induced endocytosis of the Na-K-2Cl cotransporter in MDCK cells is associated with a clathrin-dependent pathway. Am J Physiol-Cell Physiol 298, C85–C97.

Nagar, B, Overduin, M, Ikura, M, and Rini, JM (1996). Structural basis of calcium-induced E-cadherin rigidification and dimerization. Nature 380, 360–364.

Nakazawa, N, Sathe, AR, Shivashankar, GV, and Sheetz, MP (2016). Matrix mechanics controls FHL2 movement to the nucleus to activate p21 expression. Proc Natl Acad Sci 113, E6813–E6822.

Neuman, NA, Ma, S, Schnitzler, GR, Zhu, Y, Lagna, G, and Hata, A (2009). The Four-and-a-half LIM Domain Protein 2 Regulates Vascular Smooth Muscle Phenotype and Vascular Tone. J Biol Chem 284, 13202–13212.

Niggli, V, Schmid, M, and Nievergelt, A (2006). Differential roles of Rho-kinase and myosin light chain kinase in regulating shape, adhesion, and migration of HT1080 fibrosarcoma cells. Biochem Biophys Res Commun 343, 602–608.

Noordstra, I, Hermoso, MD, Schimmel, L, Bonfim-Melo, A, Kalappurakkal, JM, Mayor, S, Gordon, E, Cusachs, PR, and Yap, AS (2021). Cortical actin flow activates an α-catenin clutch to assemble adherens junctions. 2021.07.28.454239.

Nuccitelli, R, Nuccitelli, P, Ramlatchan, S, Sanger, R, and Smith, PJS (2008). Imaging the electric field associated with mouse and human skin wounds. Wound Repair Regen 16, 432–441.

Nusrat, A, Giry, M, Turner, JR, Colgan, SP, Parkos, CA, Carnes, D, Lemichez, E, Boquet, P, and Madara, JL (1995). Rho protein regulates tight junctions and perijunctional actin organization in polarized epithelia. Proc Natl Acad Sci 92, 10629–10633.

Oakes, PW, Wagner, E, Brand, CA, Probst, D, Linke, M, Schwarz, US, Glotzer, M, and Gardel, ML (2017). Optogenetic control of RhoA reveals zyxin-mediated elasticity of stress fibres. Nat Commun 8, 15817.

Oda, H, and Takeichi, M (2011). Structural and functional diversity of cadherin at the adherens junction. J Cell Biol 193, 1137–1146.

Odenwald, MA, Choi, W, Kuo, W-T, Singh, G, Sailer, A, Wang, Y, Shen, L, Fanning, AS, and Turner, JR (2018). The scaffolding protein ZO-1 coordinates actomyosin and epithelial apical specializations in vitro and in vivo. J Biol Chem 293, 17317–17335.

Oldenburg, J, and de Rooij, J (2014). Mechanical control of the endothelial barrier. Cell Tissue Res 355, 545–555.

Oliveira, KMC, Barker, JH, Berezikov, E, Pindur, L, Kynigopoulos, S, Eischen-Loges, M, Han, Z, Bhavsar, MB, Henrich, D, and Leppik, L (2019). Electrical stimulation shifts healing/scarring towards regeneration in a rat limb amputation model. Sci Rep 9, 11433.

Oudin, MJ, and Weaver, VM (2016). Physical and Chemical Gradients in the Tumor Microenvironment Regulate Tumor Cell Invasion, Migration, and Metastasis. Cold Spring Harb Symp Quant Biol 81, 189–205.

Palmer, LG (2017). Epithelial transport in The Journal of General Physiology. J Gen Physiol 149, 897–909.

Pannekoek, W-J, de Rooij, J, and Gloerich, M (2019). Force transduction by cadherin adhesions in morphogenesis. F1000Research 8, F1000 Faculty Rev-1044.

Papakonstanti, EA, Vardaki, EA, and Stournaras, C (2000). Actin Cytoskeleton: A Signaling Sensor in Cell Volume Regulation. Cell Physiol Biochem 10, 257–264.

Park, J-A et al. (2015). Unjamming and cell shape in the asthmatic airway epithelium. Nat Mater 14, 1040–1048.

Paxton, S, Peckham, M, and Knibbs, A (2003). The Leeds Histology Guide.

Pearl, EJ, Li, J, and Green, JBA (2017). Cellular systems for epithelial invagination. Philos Trans R Soc B Biol Sci 372, 20150526.

Pearl, R (1900). STUDIES ON ELECTROTAXIS. I.—ON THE REACTIONS OF CERTAIN INFUSORIA TO THE ELECTRIC CURRENT. Am J Physiol-Leg Content 4, 96–123.

Pesqueira, T, Costa-Almeida, R, and Gomes, ME (2017). Uncovering the effect of low-frequency static magnetic field on tendon-derived cells: from mechanosensing to tenogenesis. Sci Rep 7, 10948.

Piekny, AJ, and Glotzer, M (2008). Anillin Is a Scaffold Protein That Links RhoA, Actin, and Myosin during Cytokinesis. Curr Biol 18, 30–36.

Pinheiro, D, and Bellaïche, Y (2018). Mechanical Force-Driven Adherens Junction Remodeling and Epithelial Dynamics. Dev Cell 47, 3–19.

van de Pol, V, Vos, M, DeRuiter, MC, Goumans, MJ, de Vries, CJM, and Kurakula, K (2020). LIM-only protein FHL2 attenuates inflammation in vascular smooth muscle cells through inhibition of the NFκB pathway. Vascul Pharmacol 125–126, 106634.

Preibisch, S, Saalfeld, S, and Tomancak, P (2009). Globally optimal stitching of tiled 3D microscopic image acquisitions. Bioinformatics 25, 1463–1465.

Priya, R, Gomez, GA, Budnar, S, Acharya, BR, Czirok, A, Yap, AS, and Neufeld, Z (2017). Bistable front dynamics in a contractile medium: Travelling wave fronts and cortical advection define stable zones of RhoA signaling at epithelial adherens junctions. PLOS Comput Biol 13, e1005411.

Pullarkat, P, Fernandez, P, and Ott, A (2007). Rheological properties of the Eukaryotic cell cytoskeleton. Phys Rep 449, 29–53.

Rajendran, SB, Challen, K, Wright, KL, and Hardy, JG (2021). Electrical Stimulation to Enhance Wound Healing. J Funct Biomater 12, 40.

Rauzi, M, Lenne, P-F, and Lecuit, T (2010). Planar polarized actomyosin contractile flows control epithelial junction remodelling. Nature 468, 1110–1114.

Razzell, W, Bustillo, ME, and Zallen, JA (2018). The force-sensitive protein Ajuba regulates cell adhesion during epithelial morphogenesis. J Cell Biol 217, 3715–3730.

Saier, MH (1981). Growth and differentiated properties of a kidney epithelial cell line (MDCK). Am J Physiol-Cell Physiol 240, C106–C109.

Sala, S, and Oakes, PW (2021). Stress fiber strain recognition by the LIM protein testin is cryptic and mediated by RhoA. Mol Biol Cell 32, 1758–1771.

Salbreux, G, Charras, G, and Paluch, E (2012). Actin cortex mechanics and cellular morphogenesis. Trends Cell Biol 22, 536–545.

Schaumann, EN (2020). Geometric and Bioelectric Cues to Cell Mechanics. The University of Chicago.

Schaumann, EN, Staddon, MF, Gardel, ML, and Banerjee, S (2018). Force localization modes in dynamic epithelial colonies. Mol Biol Cell 29, 2835–2847.

Schneider, CA, Rasband, WS, and Eliceiri, KW (2012). NIH Image to ImageJ: 25 years of image analysis. Nat Methods 9, 671–675.

Skoglund, P, Rolo, A, Chen, X, Gumbiner, BM, and Keller, R (2008). Convergence and extension at gastrulation require a myosin IIB-dependent cortical actin network. Development 135, 2435–2444.

Smith, MA, Blankman, E, Gardel, ML, Luettjohann, L, Waterman, CM, and Beckerle, MC (2010). A Zyxin-Mediated Mechanism for Actin Stress Fiber Maintenance and Repair. Dev Cell 19, 365–376.

Söhl, G, and Willecke, K (2004). Gap junctions and the connexin protein family. Cardiovasc Res 62, 228–232.

Solon, J, Kaya-Çopur, A, Colombelli, J, and Brunner, D (2009). Pulsed Forces Timed by a Ratchet-like Mechanism Drive Directed Tissue Movement during Dorsal Closure. Cell 137, 1331–1342.

Song, B, Gu, Y, Pu, J, Reid, B, Zhao, Z, and Zhao, M (2007). Application of direct current electric fields to cells and tissues in vitro and modulation of wound electric field in vivo. Nat Protoc 2, 1479–1489.

Spahn, P, and Reuter, R (2013). A Vertex Model of Drosophila Ventral Furrow Formation. PLOS ONE 8, e75051.

Staddon, MF, Cavanaugh, KE, Munro, EM, Gardel, ML, and Banerjee, S (2019). Mechanosensitive Junction Remodeling Promotes Robust Epithelial Morphogenesis. Biophys J 117, 1739–1750.

Staple, DB, Farhadifar, R, Röper, J-C, Aigouy, B, Eaton, S, and Jülicher, F (2010). Mechanics and remodelling of cell packings in epithelia. Eur Phys J E 33, 117–127.

Stoops, SL, Pearson, AS, Weaver, C, Waterson, AG, Days, E, Farmer, C, Brady, S, Weaver, CD, Beauchamp, RD, and Lindsley, CW (2011). Identification and Optimization of Small Molecules That Restore E-Cadherin Expression and Reduce Invasion in Colorectal Carcinoma Cells. ACS Chem Biol 6, 452–465.

Strange, K (1993). Cellular and Molecular Physiology of Cell Volume Regulation, CRC Press.

Strickland, D, Lin, Y, Wagner, E, Hope, CM, Zayner, J, Antoniou, C, Sosnick, TR, Weiss, EL, and Glotzer, M (2012). TULIPs: tunable, light-controlled interacting protein tags for cell biology. Nat Methods 9, 379–384.

Stringer, C, Wang, T, Michaelos, M, and Pachitariu, M (2021). Cellpose: a generalist algorithm for cellular segmentation. Nat Methods 18, 100–106.

Sun, X et al. (2020). Mechanosensing through Direct Binding of Tensed F-Actin by LIM Domains. Dev Cell 55, 468-482.e7.

Sun, X, and Alushin, GM (2022). Cellular force-sensing through actin filaments. FEBS J n/a.

Sweeny, HL, and Houdusse, A (2010). Structural and Functional Insights into the Myosin Motor Mechanism. Annu Rev Biophys 39, 539–557.

Swiatlowska, P et al. (2022). Pressure and stiffness sensing together regulate vascular smooth muscle cell phenotype switching. Sci Adv 8, eabm3471.

Taghian, T, Narmoneva, DA, and Kogan, AB (2015). Modulation of cell function by electric field: a high-resolution analysis. J R Soc Interface 12, 20150153.

Tai, G, Reid, B, Cao, L, and Zhao, M (2009). Electrotaxis and Wound Healing: Experimental Methods to Study Electric Fields as a Directional Signal for Cell Migration. In: Chemotaxis: Methods and Protocols, ed. T Jin, and D Hereld, Totowa, NJ: Humana Press, 77–97.

Tai, K, Cockburn, K, and Greco, V (2019). Flexibility sustains epithelial tissue homeostasis. Curr Opin Cell Biol 60, 84–91.

Tang, VW (2020). Collagen, stiffness, and adhesion: the evolutionary basis of vertebrate mechanobiology. Mol Biol Cell 31, 1823–1834.

Terry, S, Nie, M, Matter, K, and Balda, MS (2010). Rho Signaling and Tight Junction Functions. Physiology 25, 16–26.

Ting, LH, Jahn, JR, Jung, JI, Shuman, BR, Feghhi, S, Han, SJ, Rodriguez, ML, and Sniadecki, NJ (2012). Flow mechanotransduction regulates traction forces, intercellular forces, and adherens junctions. Am J Physiol-Heart Circ Physiol 302, H2220–H2229.

Tojkander, S, Gateva, G, and Lappalainen, P (2012). Actin stress fibers – assembly, dynamics and biological roles. J Cell Sci 125, 1855–1864.

Tokuda, S, Miyazaki, H, Nakajima, K, Yamada, T, and Marunaka, Y (2009). Hydrostatic pressure regulates tight junctions, actin cytoskeleton and transcellular ion transport. Biochem Biophys Res Commun 390, 1315–1321.

Tokuda, S, and Yu, ASL (2019). Regulation of Epithelial Cell Functions by the Osmolality and Hydrostatic Pressure Gradients: A Possible Role of the Tight Junction as a Sensor. Int J Mol Sci 20, 3513.

Topper, JN, and Gimbrone Jr, MA (1999). Blood flow and vascular gene expression: fluid shear stress as a modulator of endothelial phenotype. Mol Med Today 5, 40–46.

Totsukawa, G, Yamakita, Y, Yamashiro, S, Hartshorne, DJ, Sasaki, Y, and Matsumura, F (2000). Distinct Roles of Rock (Rho-Kinase) and Mlck in Spatial Regulation of Mlc Phosphorylation for Assembly of Stress Fibers and Focal Adhesions in 3t3 Fibroblasts. J Cell Biol 150, 797–806.

Trichas, G et al. (2012). Multi-cellular rosettes in the mouse visceral endoderm facilitate the ordered migration of anterior visceral endoderm cells. PLoS Biol 10, e1001256.

Uemura, A, Nguyen, T-N, Steele, AN, and Yamada, S (2011). The LIM Domain of Zyxin Is Sufficient for Force-Induced Accumulation of Zyxin During Cell Migration. Biophys J 101, 1069–1075.

Vanderleest, TE, Smits, CM, Xie, Y, Jewett, CE, Blankenship, JT, and Loerke, D (2018). Vertex sliding drives intercalation by radial coupling of adhesion and actomyosin networks during Drosophila germband extension. ELife 7, e34586.

Varadarajan, S, Stephenson, RE, Misterovich, ER, Wu, JL, Erofeev, IS, Goryachev, AB, and Miller, AL (2021). Mechanosensitive calcium signaling in response to cell shape changes promotes epithelial tight junction remodeling by activating RhoA. 2021.05.18.444663.

Vicente-Manzanares, M, Ma, X, Adelstein, RS, and Horwitz, AR (2009). Non-muscle myosin II takes centre stage in cell adhesion and migration. Nat Rev Mol Cell Biol 10, 778–790.

Villalonga, P, Villalonga, P, and Ridley, AJ (2006). Rho GTPases and cell cycle control. Growth Factors 24, 159–164.

Wagh, K, Ishikawa, M, Garcia, DA, Stavreva, DA, Upadhyaya, A, and Hager, GL (2021). Mechanical Regulation of Transcription: Recent Advances. Trends Cell Biol 31, 457–472.

Wagner, E, and Glotzer, M (2016). Local RhoA activation induces cytokinetic furrows independent of spindle position and cell cycle stage. J Cell Biol 213, 641–649.

Walko, G, Castañón, MJ, and Wiche, G (2015). Molecular architecture and function of the hemidesmosome. Cell Tissue Res 360, 363–378.

Wall, ME, and Banes, AJ (2005). Early responses to mechanical load in tendon: role for calcium signaling, gap junctions and intercellular communication. J Musculoskelet Neuronal Interact 5, 70–84.

Walsh, SV, Hopkins, AM, Chen, J, Narumiya, S, Parkos, CA, and Nusrat, A (2001). Rho kinase regulates tight junction function and is necessary for tight junction assembly in polarized intestinal epithelia. Gastroenterology 121, 566–579.

Wang, J et al. (2022). Role of SPAK–NKCC1 signaling cascade in the choroid plexus blood–CSF barrier damage after stroke. J Neuroinflammation 19, 91.

Wang, K, Parekh, U, Ting, JK, Yamamoto, NAD, Zhu, J, Costantini, T, Arias, AC, Eliceiri, BP, and Ng, TN (2019). A Platform to Study the Effects of Electrical Stimulation on Immune Cell Activation During Wound Healing. Adv Biosyst 3, 1900106.

Wang, Y, Zhang, C, Yang, W, Shao, S, Xu, X, Sun, Y, Li, P, Liang, L, and Wu, C (2021). LIMD1 phase separation contributes to cellular mechanics and durotaxis by regulating focal adhesion dynamics in response to force. Dev Cell 56, 1313-1325.e7.

Warrick, HM, and Spudich, JA (1987). Myosin structure and function in cell motility. Annu Rev Cell Biol 3, 379–421.

Wei, C, Wang, X, Chen, M, Ouyang, K, Song, L-S, and Cheng, H (2009). Calcium flickers steer cell migration. Nature 457, 901–905.

Wei, C, Wang, X, Zheng, M, and Cheng, H (2012). Calcium gradients underlying cell migration. Curr Opin Cell Biol 24, 254–261.

Wolpert, L, Smith, JC, Keller, R, Davidson, L, Edlund, A, Elul, T, Ezin, M, Shook, D, and Skoglund, P (2000). Mechanisms of convergence and extension by cell intercalation. Philos Trans R Soc Lond B Biol Sci 355, 897–922.

Wood, W, and Martin, P (2002). Structures in focus—filopodia. Int J Biochem Cell Biol 34, 726–730.

W. Style, R, Boltyanskiy, R, K. German, G, Hyland, C, W. MacMinn, C, F. Mertz, A, A. Wilen, L, Xu, Y, and R. Dufresne, E (2014). Traction force microscopy in physics and biology. Soft Matter 10, 4047–4055.

Wu, C et al. (2015). Mechanosensitive PPAP2B Regulates Endothelial Responses to Atherorelevant Hemodynamic Forces. Circ Res 117, e41–e53.

Wu, D et al. (2017). HIF-1α is required for disturbed flow-induced metabolic reprogramming in human and porcine vascular endothelium. ELife 6, e25217.

Yamada, S, and Nelson, WJ (2007). Localized zones of Rho and Rac activities drive initiation and expansion of epithelial cell–cell adhesion. J Cell Biol 178, 517–527.

Yao, L, Pandit, A, Yao, S, and McCaig, CD (2011). Electric Field-Guided Neuron Migration:A Novel Approach in Neurogenesis. Tissue Eng Part B Rev 17, 143–153.

Ye, GJC, Nesmith, AP, and Parker, KK (2014). The Role of Mechanotransduction on Vascular Smooth Muscle Myocytes Cytoskeleton and Contractile Function. Anat Rec 297, 1758–1769.

Zajdel, TJ, Shim, G, and Cohen, DJ (2020). Come together: bioelectric healing-on-a-chip. 2020.12.29.424578.

Zehnder, SM, Suaris, M, Bellaire, MM, and Angelini, TE (2015). Cell Volume Fluctuations in MDCK Monolayers. Biophys J 108, 247–250.

Zhou, J, Li, Y-S, and Chien, S (2014). Shear stress-initiated signaling and its regulation of endothelial function. Arterioscler Thromb Vasc Biol 34, 2191–2198.